The Thesis Committee for Michael Brett Cronin
Certifies that this is the approved version of the following thesis:

Core-scale heterogeneity and dual-permeability pore structure in the Barnett Shale

APPROVED BY
SUPERVISING COMMITTEE:

Supervisor:

Peter Flemings

Kitty Milliken

Marc Hesse

Core-scale heterogeneity and dual-permeability pore structure in the Barnett Shale

by

Michael Brett Cronin; B.S.; B.S.

Thesis

Presented to the Faculty of the Graduate School of

The University of Texas at Austin

in Partial Fulfillment

of the Requirements

for the Degree of

Master of Science in Geological Sciences

The University of Texas at Austin

December 2014

Dedication

I thank my adviser, family, friends, the Geofluids group, and colleagues for their tireless support and encouragement. My time at the University of Texas has been an absolute blessing. In all things, Ad maiorem Dei gloriam.

Acknowledgements

This research was funded by grants from the Shell-University of Texas Unconventional Resources (SUTUR) program and the American Association of Petroleum Geologists (AAPG) Grants in Aid program (Mruk Family Named Grant). In addition, I was funded by the UT GeoFluids Consortium members (Anadarko, BP, BHP Billiton, Chevron, ConocoPhillips, ExxonMobil, Hess, Murphy Oil Corporation, Repsol, Schlumberger, Shell, Statoil, and Total) and a fellowship from Statoil. I thank Patrick Smith and Tingwei (Lucy) Ko for their assistance performing the scanning electron microscopy imaging, as well as Dr. Kitty Milliken, Joel Lunsford, Maxwell Pommer, Dr. Bob Loucks, and Dr. Gregory Frébourg for all of their assistance and suggestions with mudrock petrography. Lastly, I thank my committee members (Dr. Peter Flemings (adviser), Dr. Kitty Milliken, and Dr. Marc Hesse) for their thoughtful feedback, which immeasurably improved this work.

Abstract

Core-scale heterogeneity and dual-permeability pore structure in the Barnett Shale

Michael Brett Cronin, M.S. Geo. Sci.

The University of Texas at Austin, 2014

Supervisor: Peter Flemings

Abstract: I present a stratigraphically layered dual-permeability model composed of thin, alternating, high (~9.2 x 10^{-20} m^2) and low (~3.0 x 10^{-22} m^2) permeability layers to explain pressure dissipation observed during pulse-decay permeability testing on an intact Barnett Shale core. I combine both layer parallel and layer perpendicular measurements to estimate layer permeability and layer porosity. Micro-computed x-ray tomography and scanning electron microscopy confirm the presence of alternating cm-scale layers of silty-claystone and organic-rich claystone. I interpret that the silty-claystone has a permeability of 9.2 x 10^{-20} m^2 (92 NanoDarcies) and a porosity of 1.4% and that the organic-rich claystone has a permeability of 3.0 x 10^{-22} m^2 (0.3 NanoDarcies) and a porosity of 14%. A layered architecture explains the horizontal (k_H = 107 x 10^{-21} m^2) to vertical (k_V = 2.3 x 10^{-21} m^2) permeability anisotropy ratio observed in the Barnett Shale. These core-scale results suggest that spacing between high-permeability carrier beds can influence resource recovery in shales at the reservoir-scale. I also illustrate the characteristic pulse-decay behavior of core samples with multiple mutually-orthogonal

fracture planes, ranging from a single planar fracture to the Warren and Root (1963) "sugar cube" model with three mutually-orthogonal fracture sets. By relating sub core-scale matrix heterogeneity to core-scale gas transport, this work is a step towards upscaling experimental permeability results to describe in-situ gas flow through matrix at the reservoir scale.

Table of Contents

List of Tables

List of Figures

CHAPTER 1: OVERVIEW

GOALS AND STRUCTURE OF THIS THESIS

My goal is to explore how stratigraphic layering and fractures influence gas transport in mudrock core samples. In this thesis, I develop a dual-permeability model to relate pulse-decay permeability experiments to core-scale permeability heterogeneity.

In Chapter 1, I provide an overview of thesis content, the geologic context and motivation for this study, a summary of the pulse-decay method, my contributions to current pulse-decay theory, and recommendations for future study.

In Chapter 2, I use my layered dual-permeability model to define the permeability, porosity, and spacing of claystone layers versus silty-claystone layers within a well-characterized Barnett Shale core sample. First, I present the experimental pulse-decay data. Next, I document a workflow to obtain dual-permeability model parameters from the experimental pulse-decay data and define transport properties in the claystone and silty-claystone. Finally, I compare model results to independent petrographic analysis and discuss key implications.

In Chapter 3, I experimentally validate my fractured dual-permeability model using a well-characterized fractured cement core plugs. I then use my simulator to describe controls on pulse-decay behavior in samples with various fracture geometries (single planar fracture versus a set of mutually orthogonal fractures). I show that observing a characteristic "dual-timescale" response in fractured samples relies on pressure equilibration through the fractures being rapid compared to pressure equilibration with the matrix.

In the Appendices, I provide details on the 1-D numerical simulator I wrote to validate my analytical models. In addition, I provide supplemental petrography data for the Barnett Shale core samples I studied in this thesis.

CONTEXT AND MOTIVATION

In this thesis, I use "mudrock" as the general term (with no connotations of fissility or the relative fraction of silt-sized versus clay-sized material) for fine-grained sedimentary rocks (Ingram 1953). However, I acknowledge that there are multiple textural classification schemes that can be used to define a "mudrock." For example, in Ingram's (1953) textural classification for mudrocks, more than 50 percent of all particles must be silt-sized (between 62.5 microns and 4 microns) or clay-sized (smaller than 4 microns) (Wentworth, 1922). On the other hand, Stow's (1980) textural classification requires that all particles be silt-sized or clay-sized. In this thesis, I use Shephard's (1954) textural classification to define specific mudrock lithologies based on the fraction of silt-sized versus clay-sized material (e.g., siltstone, clayey-siltstone, silty-claystone, claystone).

Relatively recent advancements in horizontal drilling and well completion techniques (hydraulic fracturing) have spurred commercial development of mudrocks as unconventional gas or unconventional oil reservoirs (EIA 2013). These unconventional mudrock reservoirs are commonly referred to as "shales" in the petroleum engineering literature (Javadpour 2009; Wilkins 2011). However, "shale" may be technically inappropriate as a geologic classification because "shale" is used to denote mudrocks with fissility (Macquaker et al. 2003).

Forecasting well performance in fractured mudrock reservoirs requires matrix permeability (Nie et al. 2012). However, characterizing matrix permeability is complicated because mudrocks are broadly heterogeneous across multiple length scales,

from the reservoir scale to the fine scale (10^4 - 10^{-4} m) (Loucks et al. 2007; Rowe et al. 2012; Hickey et al. 2007; Fathi et al. 2009; Passey et al. 2010). This tremendous heterogeneity means that basic questions such as the length-scale constituting a representative-elementary-volume in mudrocks remain poorly understood. Furthermore, production decline analysis in the Barnett Shale requires the bulk permeability of stimulated matrix to be around 1 microDarcy ($10^{-18}\ m^2$) (Patzek, 2013). This result is intriguing because core-derived permeability values are generally smaller ($k = 10^{-22} - 10^{-19}\ m^2$). Reconciling core-scale experimental permeability with inferred in-situ reservoir-scale permeability requires the presence of high-permeability pathways to increase bulk permeability (but at what length scale, and are these pathways due to fractures or some type of layering (carrier bed) phenomenon?).

Core plugs are attractive because they provide a means to conduct porosity and permeability testing on reservoir material and are *relatively* easy to obtain. Whereas core plug samples are relatively small (~1 – 3 cm) compared to the reservoir, they still represent a length scale ~10^5 times that of typical scanning electron microscopy images. Therefore, core samples may be large enough to subsume fine-scale heterogeneity and provide a representative matrix fabric for permeability. However, considerable debate exists as to whether intact core samples *can* represent in-situ fabrics (and therefore in-situ permeability) due to sampling-related disruption. Of primary concern is micro-fractures may be generated while drilling or while the sample is "unloaded" (brought from reservoir stress conditions to the surface)—hence the popularity of crushed rock "GRI" permeability (Luffel et al. 1993). Regardless, the influence of core-scale heterogeneity (~10^{-3} - 10^{-2} m) on permeability must be understood before upscaling core-scale results to the reservoir scale.

Sub-core scale heterogeneity may broadly arise from micro-fractures (naturally occurring or induced during sampling) (Gale et al. 2007; Luffel et al. 1993) or via heterogeneity in the pore-network due to depositional layering, the distribution and type of organic matter, or diagenesis (Heath et al. 2011; Wang et al. 2009; Sondergeld et al. 2010; Lin et al. 1986). In this thesis, I quantitatively illuminate the magnitude and origin of this underlying heterogeneity in shales by comparing dual-permeability models and experimental pulse-decay data. By exploring the transport implications of fractures and layering at the core-scale, I provide an experimental basis for up-scaling these effects to the reservoir scale. Therefore, this work helps improve understanding of gas flow in mudrock matrix.

PULSE-DECAY PERMEABILITY TECHNIQUE:

Origins & Method

Permeability can be measured in core samples using a steady-state method ((API) 1998) with a constant differential driving pore pressure (ΔP). When fluid flow-rate (Q) at the inlet and outlet is equal, permeability (k) is calculated by rearranging Darcy's Law [1.1]:

$$k = -\frac{Q\mu}{A}\frac{L}{\Delta P} \quad [1.1]$$

μ is fluid viscosity and L is the length of the core sample. However, the steady-state method can be problematic in low permeability samples due to difficulty measuring flow-rates and prohibitively-long test duration. Soeder (1988) reported these problems when conducting steady-state permeability measurements on Devonian gas shales and Benson (2006) reported them with crystalline rocks.

Alternatively, core sample permeability can be calculated using a transient method. Brace (1968) invented the pulse-decay technique while investigating the

permeability of crystalline rocks. Instead of measuring fluid flow rates to calculate permeability, he analyzed reservoir pressure transients to calculate core sample permeability. This transient technique is specifically used to investigate the permeability of geological materials with extremely small intrinsic permeability values (k < 1 μD , < 10^{-18} m^2) that are prohibitive of steady state analyses.

A pulse-decay experimental apparatus consists of a confined core sample hydraulically connected to fixed-volume reservoirs upstream and downstream (Figure 1.1). Prior to the experiment, the upstream reservoir, core sample, and downstream reservoir are in pore pressure equilibrium. Next, a valve is used to increase pressure in just the upstream reservoir. Thus, at initial conditions ($t = 0$) there is an original differential reservoir pressure (ΔP_0) imposed across the core sample (Figure 1.2). The experiment begins when the main valve is opened and the upstream pressure pulse starts to decay. Upstream reservoir pressure will decline and downstream pressure will increase until they asymptotically equilibrate at late-time (Figure 1.2). Permeability in the core sample is related to how quickly differential pressure (ΔP) dissipates. In practice, permeability is calculated by determining the best-fit linear slope (m) to a plot of $\ln|\Delta P/\Delta P_0|$ versus time (Figure 1.3).

The pressure diffusion equation [1.2] (shown below in one-dimension) describes fluid flow in homogeneous porous media with isotropic permeability (k) and constant porosity (ϕ). P is pressure, x is the Cartesian spatial coordinate, t is time, and C is fluid compressibility.

$$\frac{\partial^2 P}{\partial x^2} = \frac{\phi \mu C}{k} \frac{\partial P}{\partial t} \qquad [1.2]$$

Conceptually, the pulse-decay technique is a scaled down “well-test” where the pressure diffusion equation [1.2] is solved with initial/boundary conditions adapted for

core-scale flow in a fixed-volume pulse-decay apparatus (Figure 1.1) rather than reservoir-scale flow into a wellbore (Lee et al. 2003) to interpret permeability from pressure-transients. I provide details on these conditions and the solution to equation [1.2] for homogeneous core samples in the appendix (Chapter 4.2A).

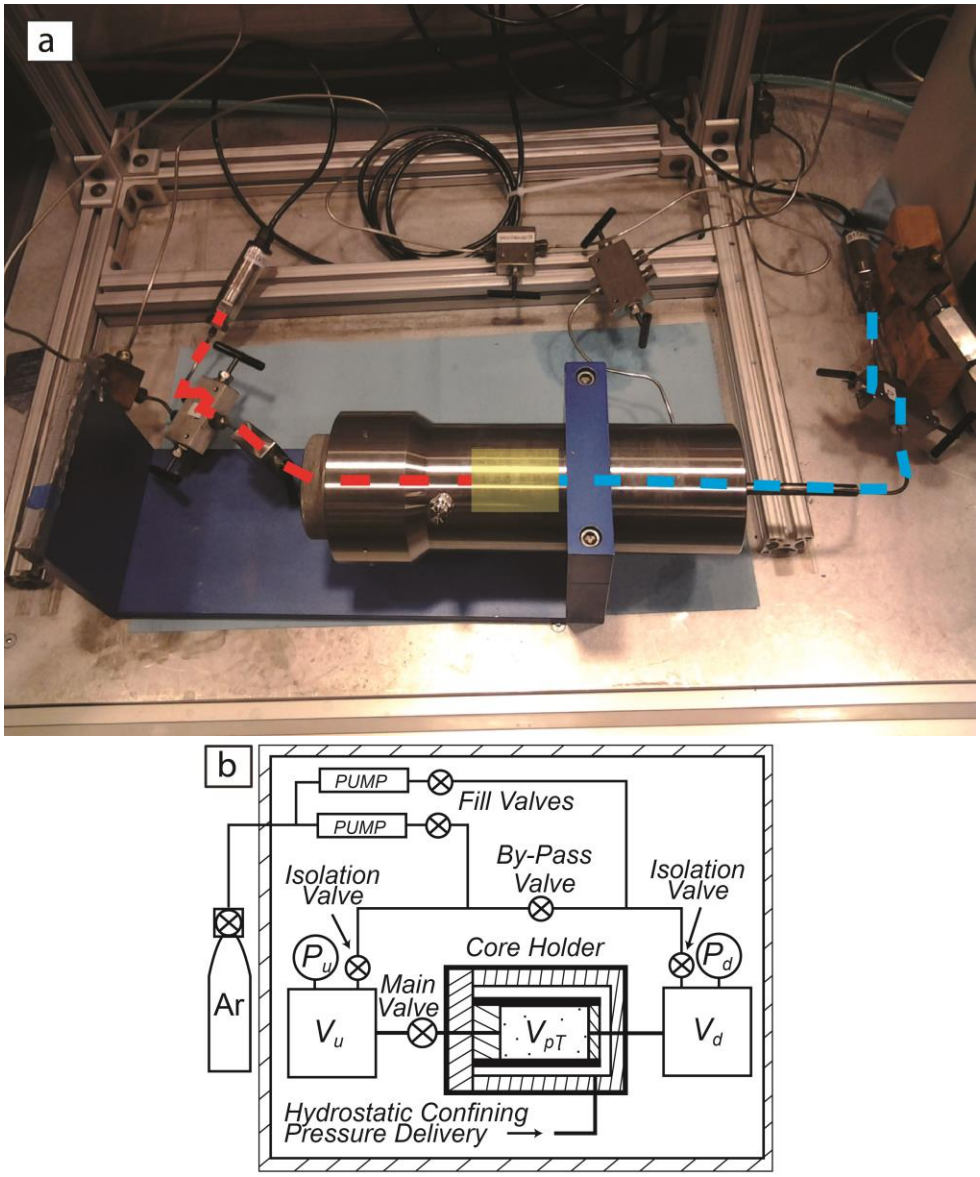

Figure 1.1 a. Experimental pulse-decay permeability apparatus. Dashed lines indicate the extent of the upstream (red) and downstream (blue) reservoirs, while the yellow box depicts the core sample within the core holder. Reservoirs consist of the connected interior volume residing in the tubing, valves/connections, and pressure transducers upstream and downstream of the core-sample. Valves allow upstream reservoir pressure to be changed independently. Bhandari et al. (*in review*) describe this pulse-decay apparatus in detail. **b**. Schematic corresponding to the apparatus shown in (**a**).

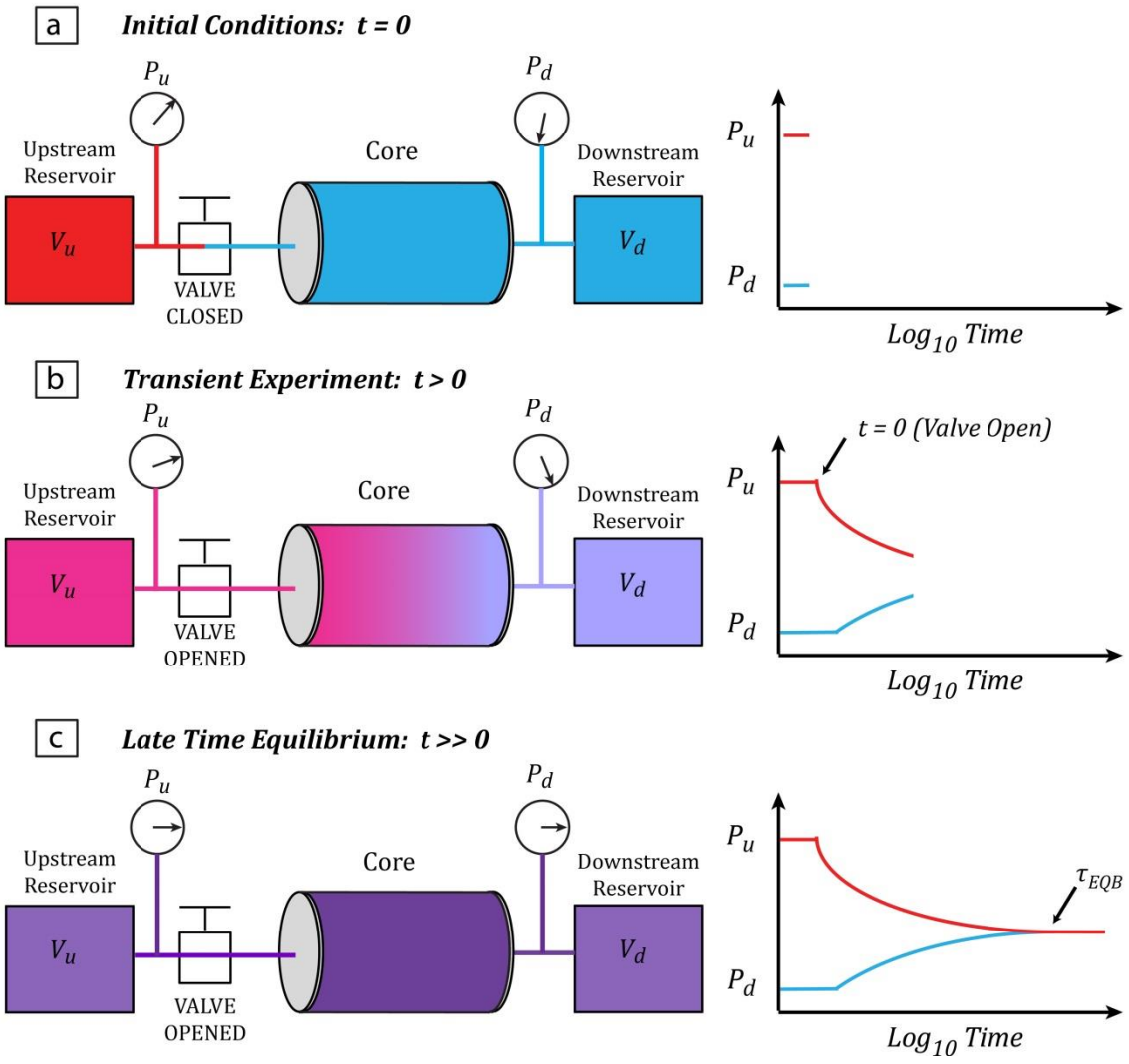

Figure 1.2 Characteristic pulse-decay behavior for homogeneous, single-porosity core samples at three fundamental times. **a.** Initial conditions. **b.** Transient phase. **c.** Late-time equilibrium phase. Cartoons in the left column depict the pore pressure distribution within the core sample and reservoirs. Red indicates maximum original upstream pore pressure (P_{u0}), blue indicates base system pore pressure (P_0), purple indicates final equilibrium pressure (P_{EQB}). The right column indicates the characteristic pressure versus time behavior observed in the upstream and downstream reservoir. Differential pore pressure dissipates during the transient phase until reservoir pressures asymptotically approach the late-time equilibrium pore pressure. The characteristic equilibration timescale (τ_{EQB}) required for 99% dissipation in differential pressure is a function of pulse-decay apparatus and core sample properties.

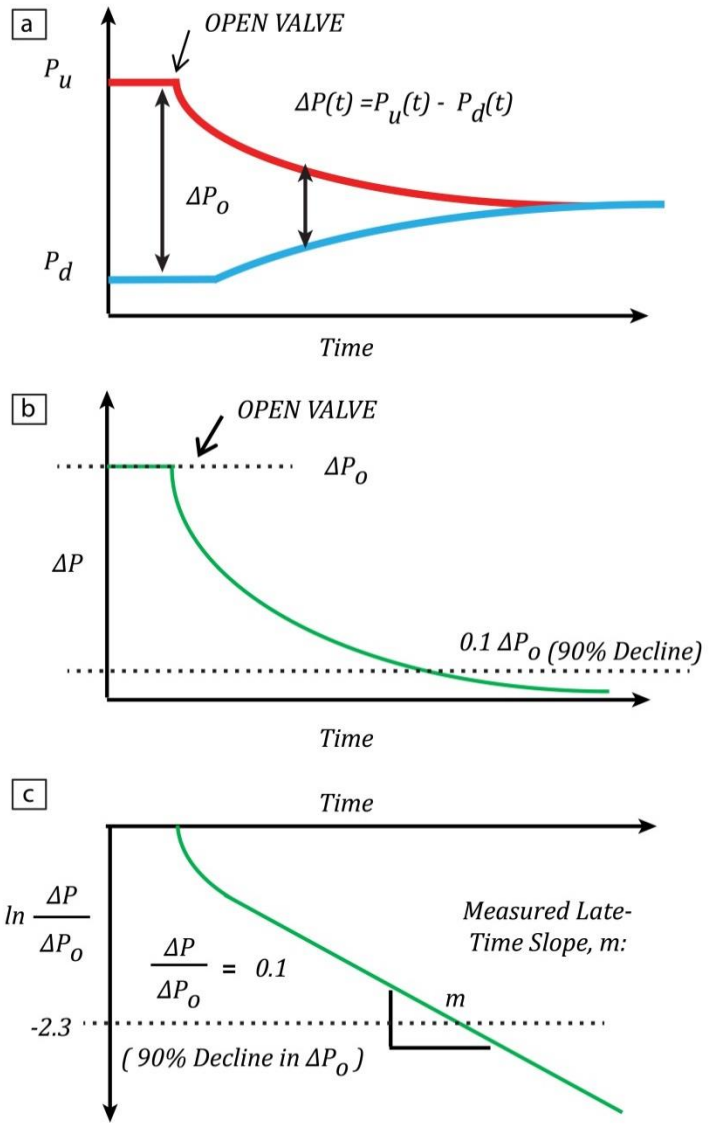

Figure 1.3 Three panel cartoon illustrating schematic pressure measurements of a homogeneous single-pore structure core during a pulse-decay experiment. **a.** Upstream P_u (red) and downstream P_d (blue) reservoir pressure over time. **b.** Differential pore pressure over time, where differential pore pressure = upstream pressure minus downstream pressure. **c.** Natural log of dimensionless differential pressure vs. time. The late time slope (after 90% decay in original differential pressure) is used in the analytical interpretation of permeability.

Effects of Heterogeneity on Pulse-Decay Behavior

Classical pulse-decay theory (Hsieh et al. 1981) predicts that core samples with isotropic permeability and constant porosity have the characteristic pulse-decay behavior illustrated in (Figure 1.2). However, core samples with significant permeability heterogeneity due to through-going fractures or high-permeability contrast stratigraphic layering can display the "dual-timescale" response illustrated in (Figure 1.4). In a "dual-timescale" response, there is an early-time convergence in the upstream and downstream reservoir pressures at the "convergence pressure" P_{conv} due to rapid flow through the high-permeability pathways. Reservoir pore pressure then slowly declines until asymptotically equilibrating at the late-time "final equilibrium pressure" P_{eqb} due to flow into the low-permeability material. Kamath et al. (1992) experimentally demonstrated that core samples with plane parallel fractures can display this "dual-timescale" response. In addition, Kamath et al. (1992) demonstrated that large reservoir volumes (relative to sample pore volume) tend to obscure this "dual-timescale" effect and produce a more "homogeneous" pulse-decay response while small reservoir volumes tend to enhance the "dual-timescale" effect. Ning (1992) developed an analytical model to predict pulse-decay behavior in core samples with plane-parallel fractures to relate pressure transients to matrix versus fracture properties.

Permeability heterogeneity at the reservoir-scale can produce a similar "dual-timescale" effect where early-time production reflects the contribution of high-permeability pathways (fractures), and late-time flow reflects the contribution of lower-permeability matrix (Cinco-Ley et al. 1981). For example, King et al. (1986) document the importance of permeability anisotropy, fracture spacing, and matrix-fracture transfer on transient gas production in fractured coal-bed methane reservoirs. Stratigraphically

layered reservoirs can also display a “dual-timescale” response similar to that of fractured reservoirs (Warren et al. 1963). Desbarats (1987) illustrates how effective permeability in layered reservoirs will change as the volume of low-permeability material (shale layers) relative to high-permeability material (sand layers) increases.

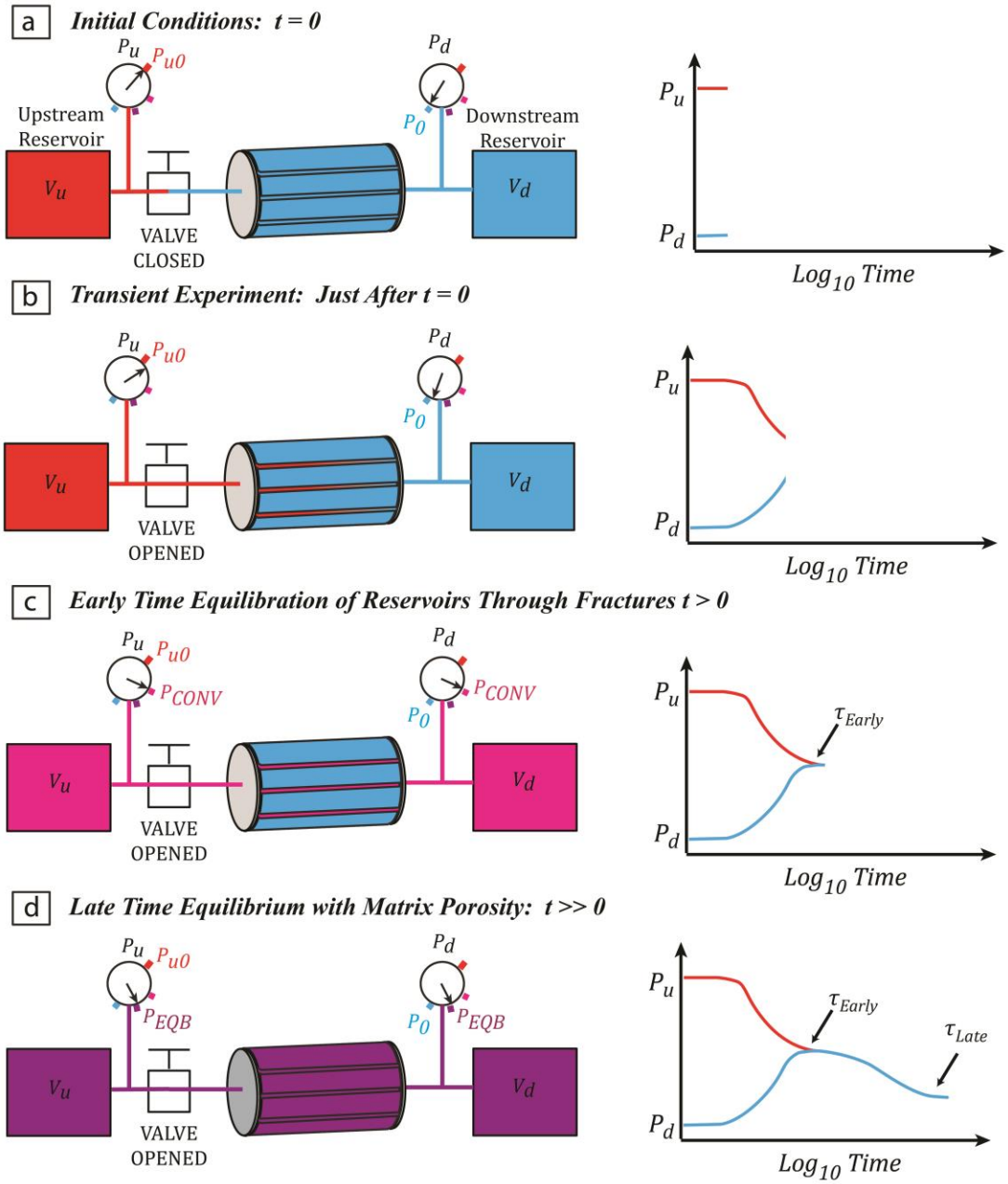
a Initial Conditions: t = 0
P_u
P_{u0}
P_d
P_0
Upstream Reservoir
Downstream Reservoir
V_u
V_d
VALVE CLOSED
P_u
P_d
Log_{10} Time
b Transient Experiment: Just After t = 0
VALVE OPENED
c Early Time Equilibration of Reservoirs Through Fractures t > 0
P_{CONV}
τ_{Early}
d Late Time Equilibrium with Matrix Porosity: t >> 0
P_{EQB}
τ_{Late}

Figure 1.4

Figure 1.4 Characteristic pulse-decay behavior of fractured core samples at four fundamental times; **a.** initial conditions, **b.** early-time pre-reservoir convergence, **c.** reservoir pressure convergence time, **d.** late-time equilibrium. Left column depicts pore pressure distribution within the core sample. Color indicates the pore fluid pressure within the matrix versus fractures/high-permeability flow paths. Red indicates maximum original upstream pore pressure (P_{u0}), blue indicates base system pore pressure (P_0), pink corresponds to reservoir convergence pressure (P_{CONV}), and purple indicates final equilibrium pressure (P_{EQB}). The right column indicates the characteristic dual-timescale pressure versus time behavior observed in the upstream and downstream reservoir, with an early-time pressure convergence followed by a late-time final equilibrium pore-pressure.

MY CONTRIBUTION TO EXISTING PULSE-DECAY THEORY

Previous pulse-decay research has primarily focused on studying interactions between the matrix and fractures (Ning 1992; Kamath et al. 1992), identifying alternative pressure boundary conditions for homogeneous core samples (e.g. constant downstream pressure (Bourbie et al. 1983) and oscillating reservoir pressure (Suri et al. 1997)), and the use of crushed samples (Luffel et al. 1993; Jannot et al. 2007). My main contribution in this thesis is that I present a dual-permeability model developed specifically to describe transport in lithologically layered systems. In addition, I provide a simple workflow to define layer properties using a novel application of a vertical permeability constraint to my model. I present this work on layered systems in Chapter 2.

My second contribution to pulse-decay research relates to the effect of fractures. Ning (1992) analytically described pulse-decay behavior in core samples with plane-parallel fractures. However, the implications for pulse-decay behavior on core-samples with multiple mutually orthogonal planes (such as the Warren and Root (1963) "sugar cube" model) have not been studied. I develop a general analytical model to predict pulse-decay behavior in fractured core samples for a range of conceptual fracture geometries, ranging from a single planar fracture to three orthogonal fracture planes ("sugar cube"). I present this work in Chapter 3.

RESULTS AND SIGNIFICANCE

I developed an analytical dual-permeability model that simulates transient gas transport during pulse-decay permeability experiment (Hsieh et al. 1981) through various synthetic layered and fractured core (dual-permeability) realizations. I demonstrate how to quantitatively illuminate core-scale heterogeneity in shales (and analogs like fractured coal bed methane) by analyzing experimental pulse-decay data with my dual-

permeability model. I provide a practical experimental-theoretical basis to relate this heterogeneity to core permeability. Therefore, this work contributes towards upscaling core results and better understanding gas flow at the reservoir scale.

In Chapter 2, I successfully use my layered dual-permeability model to experimentally characterize the transport properties (permeability, porosity, layer thickness, and spacing) of two lithologies within a layered Barnett Shale core plug. These properties were independently verified by lithologic characterization (X-ray micro-computed tomography and thin section analysis). In Chapter 3, I used a fractured cement core sample to experimentally validate my dual-permeability model for pulse-decay experiments in cores with fractures. I then use this model to illuminate the characteristic pulse-decay behavior of samples with multiple orthogonal fracture planes

My work explores the implications of multiple mutually-orthogonal fracture sets (i.e. the "sugar cube" model suggested by Warren and Root (1963) at the reservoir scale) on mass transport at the core scale, whereas previous core-scale work by Ning (1992) only considered one fracture plane orientation. I expand previous work and investigate heterogeneity due to stratigraphic layering, rather than explicitly due to fractures. Furthermore, this work is novel because it incorporates the use of vertical permeability constraints to uniquely assign layer properties during dual-permeability modeling.

LIMITATIONS

While additional transport mechanisms (e.g., gas slip and Knudsen diffusion) and stress-dependent mechanisms may be active in shales, I made simplifications to my model physics to facilitate first-order insights into core-scale permeability heterogeneity using pulse-decay permeability experiments. My model yields apparent Darcy's law values, so the user must manually correct for slip and stress effects. In addition, it is

important to keep in mind that the sample data presented here are not representative of the Barnett Shale as a whole.

RECOMMENDATIONS AND FUTURE WORK

Selecting layered core plug samples provides an opportunity to measure flow properties of two different lithologies. In addition, it provides a means to validate reservoir engineering simplifications for permeability in thinly bedded systems. In addition, measuring fractured core samples provides a means to deconvolve fracture and matrix properties. While the fractures may or may not be present in-situ, the mass transport implications of core-scale fractures on bulk permeability can be calculated. This is useful when attempting to reconcile core-scale permeability values with production decline-inferred values when trying to constrain the in-situ fracture network. Future work should enhance the sophistication of this modeling approach by considering the effects of stress, as well as non-Darcy mechanisms and interactions with organic matter.

REFERENCES

(API), A.P.I.: Recommended Practices for Core Analysis (2nd Edition). In: Exploration and Production Department, vol. Recommended Practice 40. API Publishing Services, 1220 L Street, N.W., Washington, D.C. 20005, (1998)

Benson, P.M., Meredith, P.G., Schubn|el, A.: Role of void space geometry in permeability evolution in crustal rocks at elevated pressure. Journal of Geophysical Research **111**, B12203 (2006)

Bourbie, T., Walls, J.: Pulse decay permeability: Analytical solution and experimental test : Bourbie, T; Walls, J Soc Petr Engr J, V22, N5, Oct 1982, P719-721. International Journal of Rock Mechanics and Mining Sciences & Geomechanics Abstracts **20**(2), A37-A37 (1983). doi:10.1016/0148-9062(83)90369-8

Brace, W.F., Walsh, J.B., Frangos, W.T.: Permeability of Granite Under High Pressure. Journal of Geophysical Research **73**(6), 2225-2236 (1968)

Fathi, E., Akkutlu, I.Y.: Matrix Heterogeneity Effects on Gas Transport and Adsorption in Coalbed and Shale Gas Reservoirs. Transport in Porous Media **80**(2), 281-304 (2009). doi:10.1007/s11242-009-9359-4

Hickey, J.J., Henk, B.: Lithofacies summary of the Mississippian Barnett Shale, Mitchell 2 T.P. Sims well, Wise County, Texas. AAPG Bulletin **91**(4), 437-443 (2007). doi:10.1306/12040606053

Hsieh, P.A., Tracy, J.V., Neuzil, C.E., Bredehoeft, J.D., Silliman, S.E.: A transient laboratory method for determining the hydraulic properties of `tight' rocks--I. Theory. International Journal of Rock Mechanics and Mining Sciences & Geomechanics Abstracts **18**(3), 245-252 (1981). doi:10.1016/0148-9062(81)90979-7

Jannot, Y., Lasseux, D., Vize, G., Hamon, G.: A Detailed Analysis of Permeability and Klinkenberg coefficient estimation from unsteady-state pulse-decay or draw-down experiments. Paper presented at the International Symposium of the Society of Core Analysts, Calgary, Canada, 10-12 September, 2007

Kamath, J., Boyer, R.E., Nakagawa, F.M.: Characterization of Core-Scale Heterogeneities Using Laboratory Pressure Transients. SPE Formation Evaluation **September** (1992)

Lee, J., Rollins, J.B., Spivey, J.P.: Pressure transient testing. Society of Petroleum Engineers, (2003)

Loucks, R.G., Ruppel, S.C.: Mississippian Barnett Shale: Lithofacies and depositional setting of a deep-water shale-gas succession in the Fort Worth Basin, Texas. AAPG Bulletin **91**(4), 579-601 (2007). doi:10.1306/11020606059

Luffel, D.L., Houston, R., Hopkins, C.W., Inc, S.A.H.a.A., Schettler, P.D.J.: Matrix Permeability Measurement of Gas Productive Shales. Paper presented at the 6th Annual Technical Conference and Exhibition of the Society of Petroleum Engineers, Houston, TX,

Nie, R.-S., Meng, Y.-F., Jia, Y.-L., Zhang, F.-X., Yang, X.-T., Niu, X.-N.: Dual Porosity and Dual Permeability Modeling of Horizontal Well in Naturally Fractured Reservoir. Transport in Porous Media **92**(1), 213-235 (2012). doi:10.1007/s11242-011-9898-3

Ning, X.: The measurement of matrix and fracture properties in naturally fractured low permeability cores using a pressure pulse method. Texas A&M University (1992)

Passey, Q.R., Bohacs, K., Esch, W.L., Klimentidis, R., Sinha, S.: From Oil-Prone Source Rock to Gas-Producing Shale Reservoir â□“ Geologic and Petrophysical

Characterization of Unconventional Shale-Gas Reservoirs. Paper presented at the International Oil and Gas Conference and Exhibition in China, Beijing, China, 01/01/2010

Rowe, H., Hughes, N., Robinson, K.: The quantification and application of handheld energy-dispersive x-ray fluorescence (ED-XRF) in mudrock chemostratigraphy and geochemistry. Chemical Geology **324–325**(0), 122-131 (2012). doi:http://dx.doi.org/10.1016/j.chemgeo.2011.12.023

Soeder, D.J.: Porosity and Permeability of Eastern Devonian Gas Shale. SPE Formation Evaluation(03) (1988). doi:10.2118/15213-pa

Suri, P., Azeemuddin, M., Zaman, M., Kukreti, A.R., Roegiers, J.C.: Stress-dependent permeability measurement using the oscillating pulse technique. Journal of Petroleum Science and Engineering **17**(3-4), 247-264 (1997). doi:10.1016/s0920-4105(96)00073-3

Warren, J.E., Root, P.J.: The Behavior of Naturally Fractured Reservoirs. Society of Petroleum Engineers Journal(September), 245-255 (1963)

CHAPTER 2: CORE-SCALE HETEROGENEITY AND DUAL-PERMEABILITY PORE STRUCTURE IN THE BARNETT SHALE

Abstract

I present a stratigraphically layered dual-permeability model composed of thin, alternating, high (~1.5 x 10^{-19} m^2) and low (~3.0 x 10^{-22} m^2) permeability layers to explain pressure dissipation observed during pulse-decay permeability testing on an intact Barnett Shale core. I combine both layer-parallel and layer-perpendicular measurements to estimate layer permeability and layer porosity. Micro-computed X-ray tomography and scanning electron microscopy confirm the presence of alternating cm-scale layers of silty-claystone and organic-rich claystone. I interpret that the silty-claystone has a permeability of 9.2 x 10^{-20} m^2 (92 NanoDarcies) and a porosity of 1.4% and that the organic-rich claystone has a permeability of 3.0 x 10^{-22} m^2 (0.3 NanoDarcies) and a porosity of 14%. A layered architecture explains the horizontal (k_H = 107 x 10^{-21} m^2) to vertical (k_V = 2.3 x 10^{-21} m^2) permeability anisotropy ratio observed in the Barnett Shale. These core-scale results suggest that spacing between high-permeability carrier beds can influence resource recovery in shales at the reservoir-scale. By relating sub core-scale matrix heterogeneity to core-scale gas transport, this work is a step towards upscaling experimental permeability results to describe in-situ gas flow through matrix at the reservoir scale.

Table 2.1 Nomenclature

Symbol	Description and Dimensions*/Units
English	
a	Ratio of pore volume to upstream reservoir volume (dimensionless)
a_E	Ratio of early-time pore volume to upstream reservoir volume (dimensionless)
b	Ratio of pore volume to downstream reservoir volume (dimensionless)
b_E	Ratio of early-time pore volume to downstream reservoir volume (dimensionless)
C	Compressibility ($M^{-1}L\,T^2$, Pa^{-1})
D	Diameter of core (L, m)
d	Terzaghi (1943) half-space model thickness (L, m)
$f(a,b)$	Eq. A15 in Dicker and Smits (1988) (rad^2)
H	Model thickness (L, m)
h_1	Thickness of high-permeability layers (L, m)
h_2	Thickness of low-permeability layers (L, m)
k_1	Isotropic layer permeability in high-permeability layers (L^2, m^2)
k_2	Isotropic layer permeability in low-permeability layers (L^2, m^2)
k_H	Effective horizontal permeability of homogeneous core (L^2, m^2)
k_V	Effective vertical permeability of homogeneous core (L^2, m^2)
L	Length of core (L, cm)
M	Indicial replacement for sum, $m = 0, \ldots \infty$ (Eq. [2.42]) (-)
m	Indicial index for summation (Eq. [2.42]) (-)
m_E	Early-time model dimensionless pressure dissipation slope (T^{-1}, s^{-1})
m_L	Late-time model dimensionless pressure dissipation slope (T^{-1}, s^{-1})
N_1	Number of high-permeability layers (-)
N_2	Number of low-permeability layers (-)
P_C	Absolute (hydrostatic) confining pressure ($ML^{-1}T^{-2}$, Pa)
P_{conv}	Early-time reservoir convergence pressure ($ML^{-1}T^{-2}$, Pa)
P_d	Pore pressure in downstream reservoir ($ML^{-1}T^{-2}$, Pa)
P_{eqb}	Late-time final equilibrium pressure ($ML^{-1}T^{-2}$, Pa)
P_D	Dimensionless pressure scaled between P_{u0} and P_0 (dimensionless)
P_L	Late-time system pressure ($ML^{-1}T^{-2}$, Pa)
$\bar{P}_L$	Time-averaged value of late-time system pressure ($ML^{-1}T^{-2}$, Pa)
P_u	Pore pressure in upstream reservoir ($ML^{-1}T^{-2}$, Pa)

Table 2.1, cont.

P_{u0}	Initial upstream reservoir pressure after opening main valve ($ML^{-1}T^{-2}$, Pa)
P_2	Pore pressure in the low-permeability layers ($ML^{-1}T^{-2}$, Pa)
$\bar{P}_2$	Average pore pressure in the low-permeability layers ($ML^{-1}T^{-2}$, Pa)
P_1	Pore pressure in high-permeability layers ($ML^{-1}T^{-2}$, Pa)
P_0	Initial pore pressure in sample and downstream reservoir ($ML^{-1}T^{-2}$, Pa)
$p.u.$	Porosity units (-)
S_z	Layer spacing in the z-direction (L, m)
T_V	Terzhagi (1943) dimensionless time-factor for late-time model (-)
t	Time (T, s)
t_D	Dimensionless time (-)
V_B	Bulk volume of the core sample (L^3, m^3)
V_d	Downstream reservoir volume (L^3, m^3)
V_L	Late-time system volume (L^3, m^3)
V_{pB}	Total pore volume of core (L^3, m^3)
V_{p1}	Pore volume in high-permeability layers (L^3, m^3)
V_{p2}	Pore volume in low-permeability layers (L^3, m^3)
V_u	Upstream reservoir volume (L^3, m^3)
W	Model width (L, m)
Z	Real gas deviation factor (dimensionless)
Z_{conv}	Real gas deviation factor at P_{conv} (dimensionless)
Z_{eqb}	Real gas deviation factor at P_{eqb} (dimensionless)
Z_{u0}	Real gas deviation factor at P_{u0} (dimensionless)
Z_0	Real gas deviation factor at P_0 (dimensionless)
x, y, z	Cartesian distances (x = flow direction, z = normal to bedding) (L, cm)
Greek	
γ	High to Low-Permeability Layer Porosity Ratio (dimensionless)
ΔP	Differential pore pressure, $\Delta P = (P_u - P_d)$ ($ML^{-1}T^{-2}$, Pa)
ΔP_D	Dimensionless early-time ΔP, $\Delta P_D = \Delta P/(P_{u0} - P_0)$ (dimensionless)
ΔP_L	Late-time system differential pressure, $\Delta P_L = (P_L - P_{eqb})$ (Pa)
ΔP_2	Low-permeability layer differential pressure, $\Delta P_2 = (P_2 - P_{eqb})$ ($ML^{-1}T^{-2}$, Pa)
ΔP_{LD}	Dimensionless ΔP_L, $\Delta P_{LD} = \Delta P_L/(P_{conv} - P_{eqb})$ (dimensionless)
ΔP_{2D}	Dimensionless ΔP_2, $\Delta P_{2D} = \Delta P_L/(P_0 - P_{eqb})$ (dimensionless)
λ	High to Low-Permeability Layer Transmissibility Ratio (dimensionless)
μ	Dynamic viscosity ($ML^{-1}T^{-1}$, Pa s)
τ_{conv}	Characteristic timescale for early-time convergence (T, s)
τ_{eqb}	Characteristic timescale for late-time equilibrium (T, s)
ϕ_B	Bulk porosity of core sample (fraction)
ϕ_{He}	Bulk helium porosity of core sample (fraction)

Table 2.1, cont.

ϕ_1	Porosity in high-permeability layers (fraction)
ϕ_2	Porosity in low-permeability layers (fraction)
ω	Fraction of total pore volume residing in high permeability layers (fraction)
Common Subscripts	
B	Bulk core property
D	Dimensionless
d	Downstream reservoir property
E	Early-time system property
L	Late-time system property
u	Upstream reservoir property
1	High permeability layer property
2	Low permeability layer property

* M: mass, L: length, T: time, Θ: temperature, (-): integer

INTRODUCTION

Fine-grained formations contain important hydrocarbon resources worldwide, with more than 75% of such global reserves residing outside North America (EIA 2013). Because they have low matrix permeability, shale gas and shale oil development requires extensive hydraulic fracture stimulation to achieve commercial production rates (Waters et al. 2009). The broad conceptual view is that the production rates and the cumulative recovery are controlled by the matrix permeability, the distribution of natural fractures, and the spacing between adjacent hydraulic fracture "stages" (Patzek et al. 2013). Because hydraulic fracture stimulation is a major expense, optimizing shale gas development requires precise knowledge of matrix permeability (Grieser et al. 2008).

Well-test data and/or production data at the reservoir-scale are commonly used to estimate matrix permeability (Rwechungura et al. 2011). However, interpreting matrix permeability from well production data may require production histories upwards of 10 to 20 years (Patzek et al. 2013). Thus, in many circumstances, well tests in low-permeability

media are prohibitively expensive (Lee et al. 2003). Furthermore, even if such a well test could be made, it is necessary to know the fracture spacing in order to interpret the matrix permeability (Patzek et al. 2013; Warren et al. 1963). Unfortunately, in-situ fracture networks are complex (Geiser et al. 2012; Gale et al. 2007) and shale matrix is naturally heterogeneous across multiple length scales ($< 10^{-4} – 10^{4}$ m) (Loucks et al. 2007; Rowe et al. 2012; Hickey et al. 2007; Fathi et al. 2009; Passey et al. 2010).

An alternative approach is to measure permeability at the core-scale. The transient pulse-decay technique (Brace et al. 1968) is commonly used to measure permeability in shale (Luffel et al. 1993; Jones 1997; Jannot et al. 2007). Steady-state permeability measurements ((API) 1998) are less common because low-permeability samples take a long time to reach steady-state conditions and fluid transport rates may be so low that it becomes difficult to accurately measure the volume flux (Soeder 1988; Benson et al. 2006). In the pulse-decay approach, permeability is calculated by measuring the dissipation of a pressure-pulse applied at one end of a core sample.

Pulse-decay measurements can also illuminate permeability heterogeneity. For example, Kamath (1992) and Ning (1992) showed that pulse-decay testing can record the presence of layer-parallel fractures in a core-sample and provide insight into matrix versus fracture permeability (flow) and porosity (storage). This is because the pulse-decay behavior of cores with heterogeneous permeability differs in a predictable manner from the theoretical response predicted for cores with homogeneous permeability (Kamath et al. 1992; Holder 1988; Ning 1992). This aspect of pulse-decay theory is relevant to shales because they routinely display fractures (Gale et al. 2007), fine-layering (Sondergeld et al. 2010) and significant horizontal to vertical permeability anisotropy (Vermylen 2011; Bhandari et al. *in review*). Indeed, Ning (1992) and Civan

and Rasmussen (2012) have already used core-scale pulse-decay experiments to study fracture-matrix fluid transfer. Vega et al. (2014) used high X-ray contrast gas to document the existence of significant flow-path heterogeneities in cores of shale and coal.

I perform pulse-decay testing to illuminate core-scale permeability heterogeneity due to fine mm-scale lithologic heterogeneity and provide insight into the horizontal to vertical permeability anisotropy observed in shales. It is important to understand how mm-scale heterogeneity influences gas transport and storage because pore networks in fine-grained rocks (Wang et al. 2009) are complex, and the presence of small pores ($d < 1x10^{-8}m$) leads to interesting micro-scale flow processes (Javadpour 2009; Mehmani et al. 2013; Cui et al. 2009; Civan et al. 2011).

I describe pulse-decay permeability tests on a Barnett Shale core sample. Two characteristic gas transport timescales are observed: an early timescale characterized by rapid gas flow through more permeable layers, and a late timescale characterized by slow pore-pressure equilibration. Cm-scale lithologic layers of alternating silty-claystone and claystone (textural classification of Shepard (1954)) are present based on analysis of thin-sections, scanning electron microscopy, and micro-computed X-ray tomography. I present an analytical dual-permeability model composed of alternating high and low permeability layers to explain the observed pressure dissipation. dual-timescale behavior and characterize permeability in the silty-claystone and claystone as well as permeability anisotropy. I interpret that the Barnett Shale core that we examined is composed of cm-scale layers composed of lower permeability mudstone ($\sim 10^{-22}m^2$, 0.1 NanoDarcies) interbedded with higher permeability silty-claystone ($\sim 10^{-19}m^2$, 100 NanoDarcies). The pore volume of each of these lithologies is approximately equal.

SAMPLE CHARACTERIZATION

The horizontal (6H1) and vertical (2V) Barnett Shale core plugs are from 2319.5 – 2325.3 m-KB in the Mitchell Energy T.P. Sims #2 Well, Fort Worth Basin, Texas, U.S.A. core. This core is described by several authors (Loucks et al. 2007; Hickey et al. 2007) and core plug preparation is detailed in Bhandari et al. (*in review*). I followed the thin section preparation and microscopy methods presented in Milliken et al. (2012). Grain (mineral and organic matter) abundances were determined semi-quantitatively by comparing selected electron (SEM) and optical photomicrographs, using digital image analysis program JMicrovision© (Roduit 2008). X-ray powder diffraction (XRPD) bulk mineralogy, total organic carbon (TOC), bulk carbonate (w.t. %), vitrinite-reflectance thermal maturity (R_o), and total helium porosity (ϕ_{He}) were also used to characterize the sample.

The major mineral components in core 6H1 (**Table 2.2**) are quartz (43.1%), dolomite (22.7%), and iliite + illite-smectite (17.1%). Core 6H1 is 25.62% carbonate by weight and bulk (helium) porosity ϕ_{He} (measured for intact plug at ambient stress conditions) is 4.1 +/- 1 p.u. and (**Table 2.3**). X-ray micro-computed tomography (micro-CT) cross-sections of core 6H1 reveal through-going cm-scale alternating layers of light and dark material; low attenuation (lower density) dark layers are approximately (4 – 8) mm thick, and high attenuation (higher density) light layers are approximately (6 – 12) mm thick (Figure **2.1a**). The high density layers are siliceous silty-claystone (25 - 30% silt-sized versus 65 - 70% sub-silt sized particles) and the low density layers are claystone (~ 10 - 15% silt-sized versus 85 - 90% sub-silt sized particles) (**Figure 2.1b**). The bulk TOC value for core 6H1 is 3.77% and vitrinite-reflectance thermal maturity VR_0 is 1.89% (**Table 2.3**). The dark color in micro-CT and high-resolution SEM images confirm that

organic matter is present in both the claystone (**Figure 2.2a**) and silty-claystone (**Figure 2.2b**) lithologies. However, the organic bulk volume fraction V_{fK} we interpret from digital analysis of SEM images is higher within the claystone (V_{fK} = 16 +/- 4%) than the silty-claystone (V_{fK} = 7 +/- 4%). Thus, I interpret that there is approximately twice as much organic matter present in the claystone facies.

Table 2.2 X-ray powdered diffraction (XRPD) mineralogy (performed by The James Hutton Institute, Scotland).

	Bulk Mineral Composition (%)													
Sample	Quartz	Plagioclase	K-Feldspar	Calcite	Dolomite	Pyrite	Anhydrite	Celestine	Apatite	Siderite	Anatase	Muscovite	Illite + Illite-Smectite	Total (%)
6	43.1	2.9	-	5.4	22.7	2	-	-	-	0.9	0.2	5.7	17.1	100

Table 2.3 Supplementary characterization (total organic carbon (TOC) and vitrinite reflectance (VR_o) measured by Geomark Research Ltd). Total carbonate is the sum of the calcite and dolomite (**Table 2.2**). Helium porosity measured at ambient stress in plug 6H1 using our bench-top porosimeter (**Figure 4.4**).

Sample	TOC (wt. %)	Carbonate (wt. %)	Maturity (VR_o)	φ_{He} (p.u.)
6	3.77	25.62	1.89	4.2 +/- 1

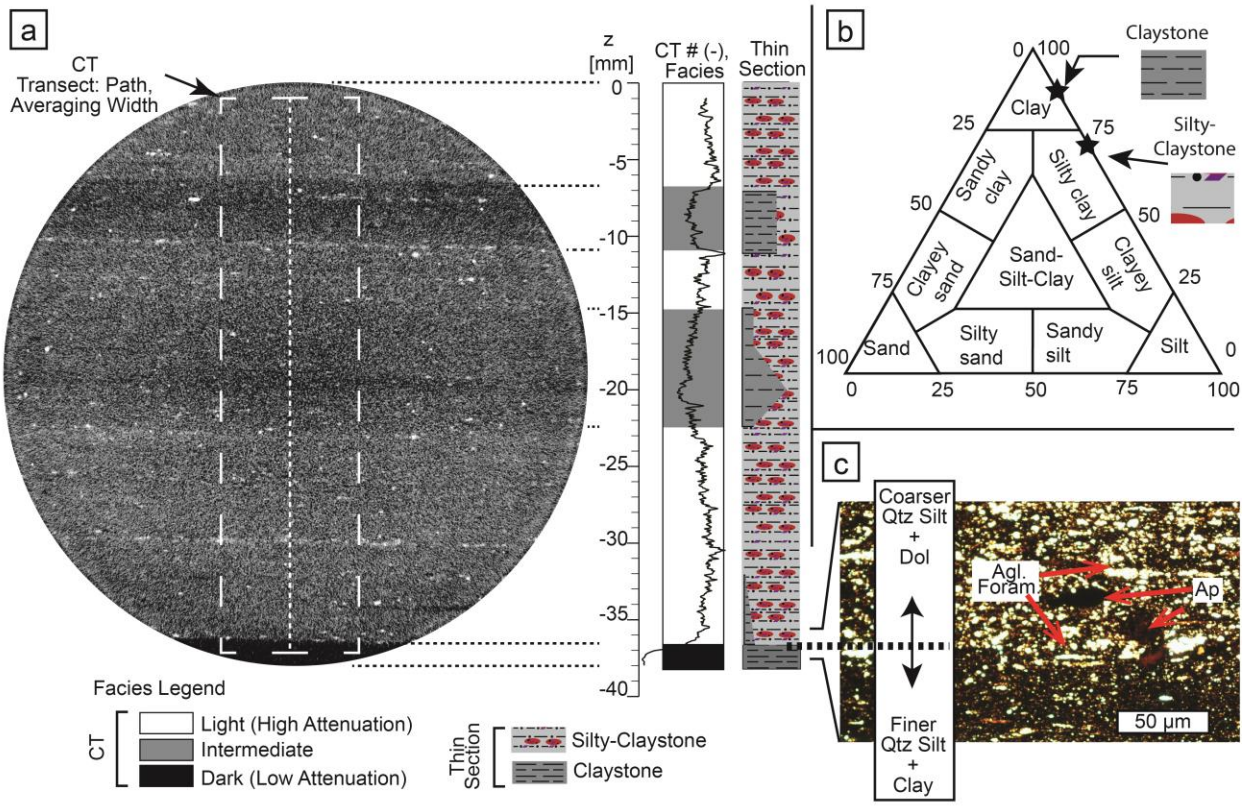

Figure 2.1 Matrix characterization of core 6H1. **a**. Micro-CT images (scanning energy = 200 keV, voxel size = 41.56 µm) of core 6H1 post pulse-decay testing in cross-section. Thin section and CT lithology logs are referenced to core cross-section. Dashed white box denotes portion of imaged used to generate the CT # curve. Imaging performed at the High-Resolution X-ray CT Facility, Department of Geological Sciences, The University of Texas at Austin. **b.** Textural classification of core 6H1 lithologies using Shepard's (1954) texture scheme. Sand-, silt-, and clay-sized fractions (%) were defined from digital image analysis using the Wentworth (1922) grain-size scale. **c.** Interface between the silty-claystone (top) and claystone (bottom) in PP light in a polished thin section.

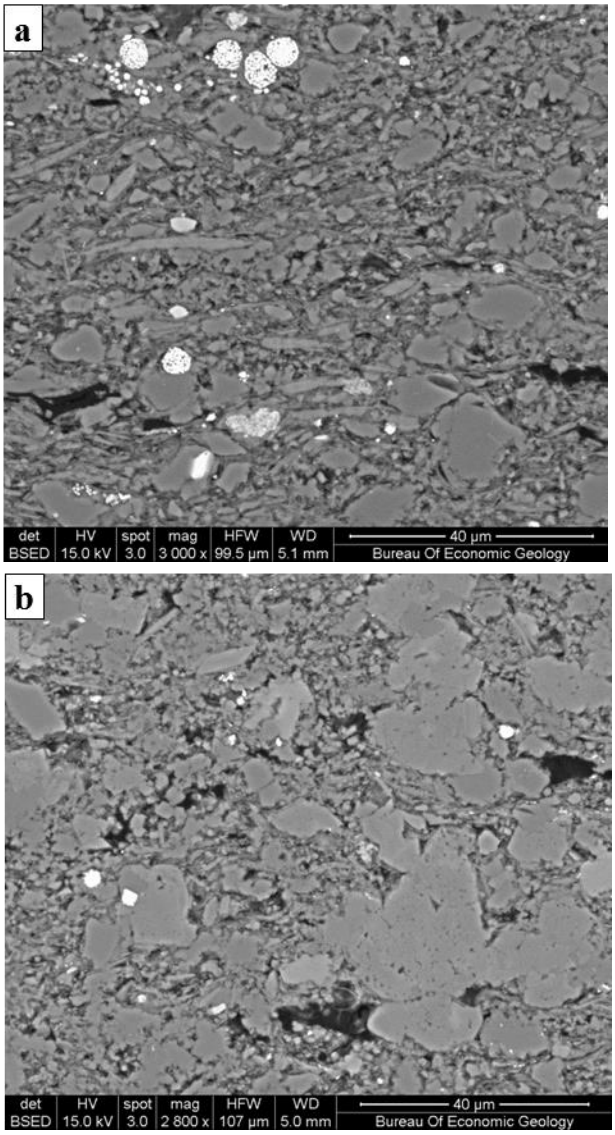

Figure 2.2 Backscatter electron (BSE) images comparing texture in the **a**. claystone and **b**. silty-claystone lithologies. The silt-size grain fraction is ~15% in the claystone compared to ~30% in the silty-claystone. The claystone is primarily sub-silt size quartz grains and platy clay minerals. Kerogen and pores are inter-mixed within the platy clays. The silty-claystone is a mixture of quartz-silt and dolomite-calcite rhombs. Bright minerals in both photomicrographs are pyrite framboids.

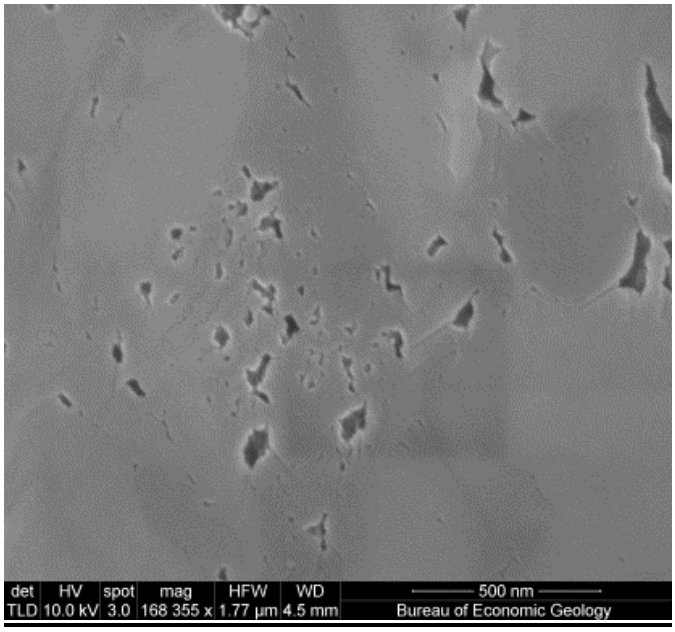

Figure 2.3 Secondary electron (SE) image of Ar-ion milled surface showing organic matter pores in the claystone. Observed pore diameters range from 50 nm to less than 5 nm.

PULSE-DECAY RESULTS

I performed pulse-decay permeability measurements (Hsieh et al. 1981) using the apparatus and methods described in Bhandari et al. (*in review*) on samples 6H1 (oriented parallel to bedding) and 2V (oriented perpendicular to bedding). In the pulse-decay method (Hsieh et al. 1981), a pressure pulse is imposed on the upstream side of a core sample and allowed to dissipate through the core sample. Sample permeability is proportional to the timescale needed for upstream (P_u) and downstream (P_d) pore pressures to equilibrate with each other at the "convergence pressure" (P_{conv}). We refer to this convergence timescale as t_{conv}.

Sample 2V takes 1000 minutes to reach convergence whereas 6H1 takes only 30 minutes (Figure 2.4). In sample 6H1, pressures initially converge and then asymptotically decline to a second pressure. If the material were homogeneous and isotropic, pulse-

decay theory (Hsieh et al. 1981) predicts a single pressure response (as seen in 2V). The dual-response observed in 6H1 suggests heterogeneity is influencing gas transport. We divide the 6H1 experimental data into an early- and late-time portion (Ning 1992) (Figure 2.5). Early-Time constitutes the time prior to initial reservoir pressure convergence (P_{conv}), while Late-Time constitutes the time until the final equilibrium pressure (P_{eqb}) is reached.

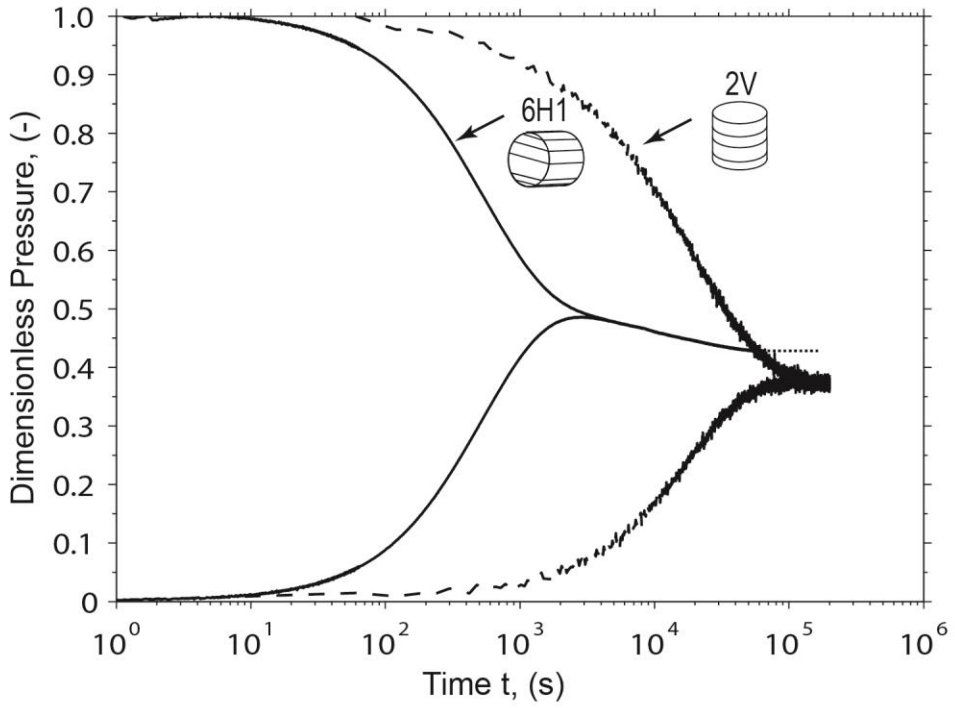

Figure 2.4 Leak-corrected pulse-decay data for the horizontal 6H1 and vertical 2V cores. Core 6H1 displays dual-timescale response composed of an early convergence in reservoir pressure timescale and a late-time final pore pressure equilibrium scale. The measured leak-rate (loss of gas into the surroundings) is $\sim 1.0\ kPa/hr$. Bhandari et al. (*in review*) describe how this measured leak-rate was used to apply a linear pressure correction to the reservoir-pressure time-series data. The experimental gas is Argon. For 6H1, the reservoir volume upstream (V_u) is $2.120 \pm 0.052\ cm^3$ and the volume downstream (V_d) is$1.763 \pm 0.067\ cm^3$. For 2V, V_u is $1.96 \pm 0.08\ cm^3$ and V_d is$2.26 \pm 0.09\ cm^3$.

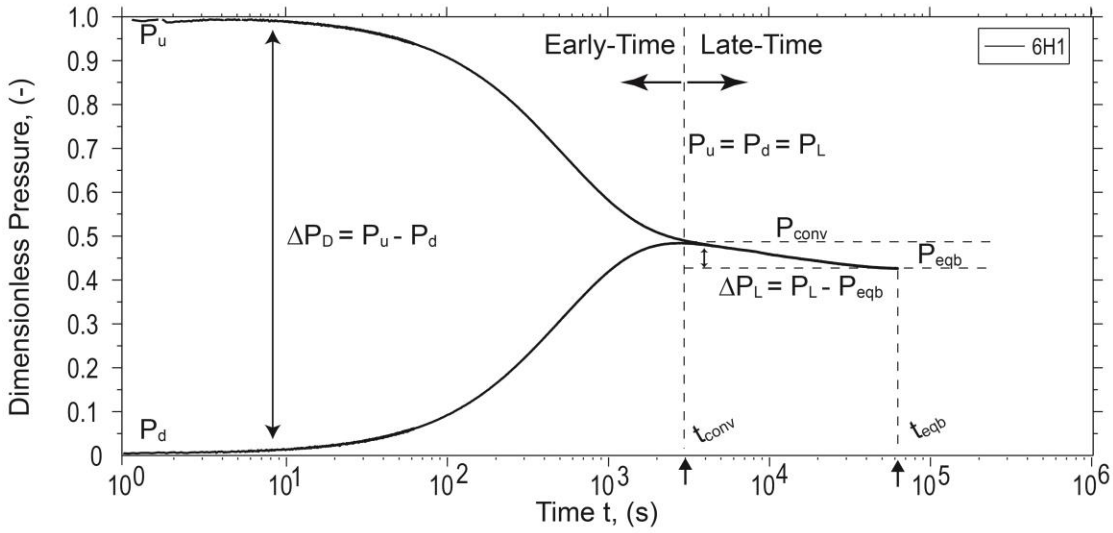

Figure 2.5 Nomenclature for interpreting multi-scale pulse decay test. Early-time consists of the initial convergence of reservoir pressure at P_{conv} and t_{conv}. Late-time consists of the secondary decline in reservoir pressure from P_{conv} to P_{eqb} between t_{conv} and t_{eqb}.

DUAL-PERMEABILITY MODEL

Model Description

I consider a rock consisting of alternating high and low permeability layers with thickness h_i, porosity ϕ_i, isotropic permeability k_i, and pore volume V_{pi} (Figure 2.6). Subscripts "$i = 1$" and "$i = 2$" refer to the high and low permeability layer properties respectively, and subscript "$i = B$" refers to bulk core values. Each low-permeability layer is bounded above and below by a high-permeability layer, so there is one more high-permeability layer than low-permeability layer ($N_1 = N_2 + 1$). The rock is assumed incompressible and gas flow is assumed to be purely advective (Darcy's law). L is the core length. H is the model thickness perpendicular to layering, and W is the model width. I assume $H = W \approx 0.866D$). ω is the fraction of total pore volume residing

within the high-permeability layers (Equation [2.1]), and γ is the intrinsic layer porosity ratio (Equation [2.2]) (see for example, ω in Warren and Root (1963)):

$$\omega = \frac{V_{p1}}{V_{p1} + V_{p2}} \quad [2.1]$$

$$\gamma = \frac{\phi_1}{\phi_2} \quad [2.2]$$

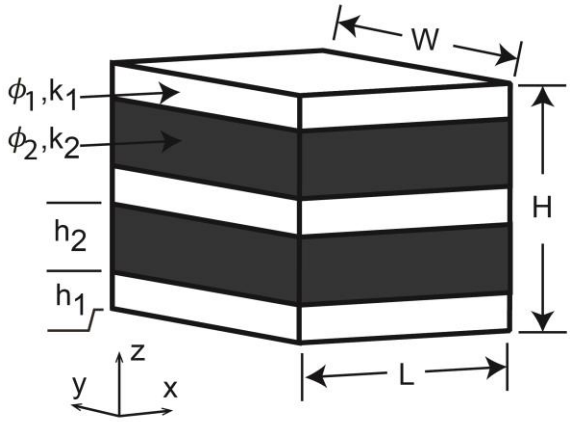

Figure 2.6 Geometry of layered dual-permeability model. Alternating high and low permeability layers with thickness, h, isotropic permeability, k, and layer porosity ϕ are present. L is the model length and equals the core sample length. Subscript "1" refers to the high-permeability layers, and subscript "2" refers to the low-permeability layers. The model has equal cross-sectional area to the core sample (with diameter D), such that $H = W \approx 0.866D$.

Pore Volumes

Boyles Law is used to calculate the total pore volume in the sample:

$$V_{pB} = \frac{\left(\frac{P_{eqb}}{Z_{eqb}} - \frac{P_{u0}}{Z_{u0}}\right)V_u + \left(\frac{P_{eqb}}{Z_{eqb}} - \frac{P_0}{Z_0}\right)V_d}{\frac{P_0}{Z_0} - \frac{P_{eqb}}{Z_{eqb}}} \quad [2.3]$$

P_0 is the initial pressure in both the sample and downstream reservoir, P_{u0} is the initial upstream pressure, and P_{eqb} is the pressure after total equilibration of the upstream and downstream pressures (Figure 2.5). Z_{eqb}, Z_{u0}, and Z_0 are real gas compressibility factors (Reid et al. 1987), and V_u and V_d are the upstream and downstream reservoir volumes. V_{pB} is found to be 1.368 cm^3, which corresponds to a bulk porosity (ϕ_B) of 6.9% (**Table 2.4**).To estimate the pore volume within the high-permeability layers, V_{p1}, we assume no flow in the low-permeability layers during early-time (Figure 2.5, Figure 2.7a):

$$V_{p1} = \frac{\left(\frac{P_{conv}}{Z_{conv}} - \frac{P_{u0}}{Z_{u0}}\right)V_u + \left(\frac{P_{conv}}{Z_{conv}} - \frac{P_0}{Z_0}\right)V_d}{\frac{P_0}{Z_0} - \frac{P_{conv}}{Z_{conv}}} \quad [2.4]$$

Where P_{conv} and Z_{conv} are the pressure and z-factor at the end of early-time, and V_{p1} is found to be 0.657 cm^3. Pore volume in the low-permeability layers is the difference of equations [2.3] and [2.4]:

$$V_{p2} = V_{pB} - V_{p1} \quad [2.5]$$

V_{p2} is found to equal 0.711 cm^3. Approximately one half of total pore volume resides within the high-permeability layers ($\omega = 0.48$) (Eq. [2.1]).

Table 2.4 Pulse-decay porosimetry results for 6H1 (Argon).

V_{pB} $[cm^3]$	$V_{p1}[cm^3]$	$V_{p2}[cm^3]$	ϕ_B [p.u.]	ω [fraction]
1.368	0.657	0.657	6.9 ± 0.57	0.48

The cumulative thickness of the high-permeability layers (H_1) is proportional to both layer porosity (ϕ_1), total layer thickness (H), and the volume of pores in the high-permeability layers (V_{p1}):

$$H_1 = \frac{V_{p1}}{\phi_1 HL} \quad [2.6]$$

The cumulative thickness of the low-permeability layers (H_2) is calculated in the same manner as equation [2.6]:

$$H_2 = \frac{V_{p2}}{\phi_2 HL} \quad [2.7]$$

The number of low-permeability layers (N_2) is equal to cumulative thickness H_2 divided by individual layer thickness h_2:

$$N_2 = \frac{H_2}{h_2} \quad [2.8]$$

Equations [2.1], [2.5], [2.6], and [2.7] are combined to relate high-permeability layer porosity ϕ_1 to low-permeability layer porosity ϕ_2:

$$\phi_1 = \frac{\omega\phi_B}{1-(1-\omega)\frac{\phi_B}{\phi_2}} \quad [2.9]$$

In equation [2.9] both ϕ_1 and ϕ_2 are unknown.

Early-Time Model

The linear best-fit slope (m_E) of $ln\left|\frac{P_u(t)-P_d(t)}{P_{u0}-P_0}\right|$ versus time (Figure 2.8) is used to calculate an effective horizontal permeability k_H of the core (6H1) equal to $9.2\ x10^{-20} m^2$ (92 nD) (Bhandari et al. *in review*) using the standard approach described by Dicker and Smits (1988):

$$k_H = \frac{\omega\phi_B\,\overline{\mu C}_E\,L^2}{f(a_E,b_E)} m_E \quad [2.10]$$

To calculate k_H, properties are evaluated at the convergence pressure (Figure 2.5), where $\overline{\mu C}_E$ is the average viscosity-compressibility product evaluated at P_{conv} and $f(a_E, b_E)$ is a function of the high-permeability layer pore volume ($V_{p1} = 0.657\ cm^3$) and reservoir

volumes ($V_u = 2.120\ cm^3,\ V_d = 1.763\ cm^3$). Refer to Appendix 2A for additional details.

I assume that Early-Time flow occurs only through the high permeability layers until P_u and P_d converge at P_{conv} (Figure 2.7a) and that there is no flow into the low permeability layers. To calculate k_1, the permeability of the high-permeability layer, we must correct for the fraction of the cross-sectional area that is composed of high-permeability material in the sample:

$$k_1 = \frac{\omega k_H}{[\gamma(1-\omega)+\omega]} \quad [2.11]$$

However, I do not independently know the volume fraction of the silty-claystone versus claystone layers because I do not know the porosity within these layers (constrained by γ).

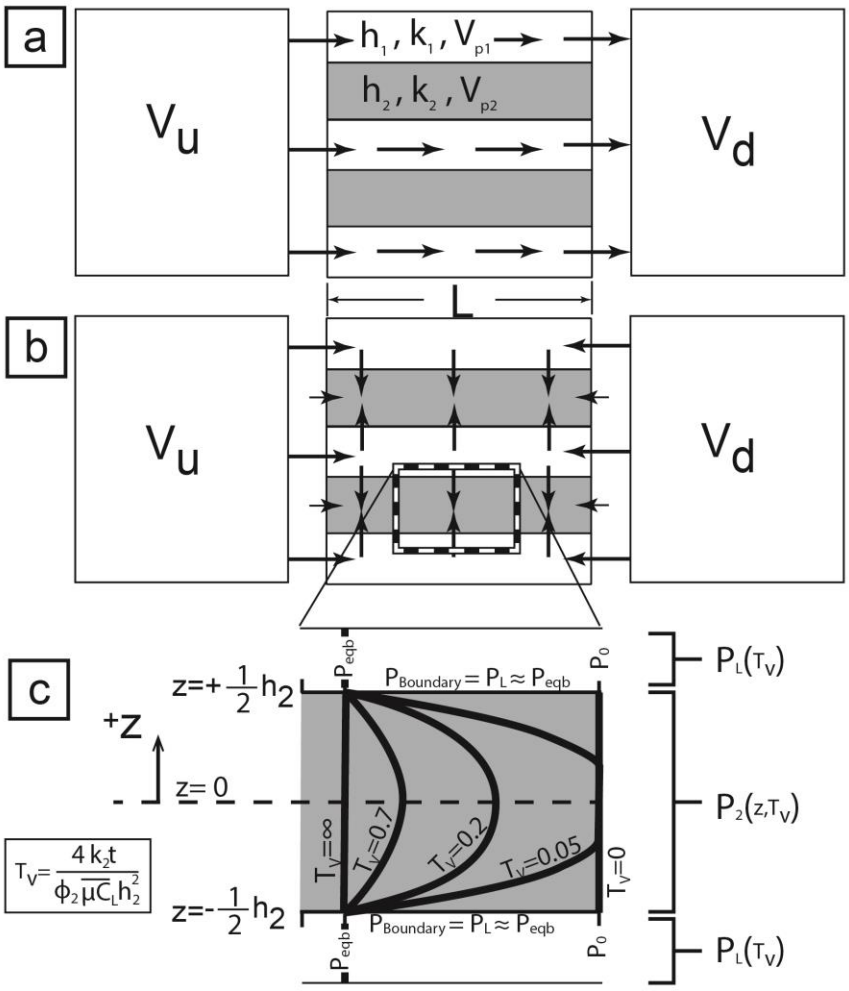

Figure 2.7 Dual-permeability model. **a**. At Early-Time, gas flows from the upstream to downstream reservoir through high perm layers (with assumption of no flow into low-permeability layers). **b**. At Late-Time, gas flows into the low-permeability layers and high-permeability layers are in pressure equilibrium. **c**. In simplified 1-D model, each low-permeability layer is a half-space where gas flows only in the z-direction (perpendicular to layering). The layer edges ($z = \pm\frac{h_2}{2}$) are in pressure communication with the late-time volume ($V_u + V_d + V_{p1}$). I approximate pressure at the layer edges as a constant pressure boundary condition equal to P_{eqb}. Pressure within the low-permeability layer ($P_2(z, T_V)$) is shown at different values of dimensionless time-factor T_V (Terzaghi 1943) ranging from initial conditions ($T_V = 0$) until an infinite time has passed ($T_V = \infty$). Average low-permeability layer pressure ($\bar{P}_2$) increases from P_0 to P_{eqb}, while P_L declines from P_{conv} to P_{eqb}.

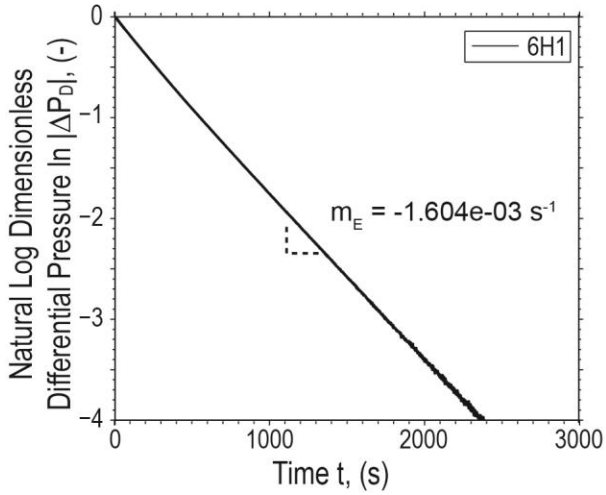

Figure 2.8 Early-Time dissipation slope (m_E) from the natural log of dimensionless differential pressure ($\Delta P_D(t) = \frac{P_u(t)-P_d(t)}{P_{u0}-P_0}$) versus time. m_E is measured from straight-line portion after 90% decay in the original differential pressure across the core sample ($\Delta P_D = 0.1$).

Late-Time Model

At Late-Time, gas flows from the high-permeability layers (V_{p1}) and reservoirs (V_u, V_d) into the low-permeability layers (V_{p2}) (Figure 2.7b). I adapt Ning's (1992) method and combine the reservoirs and high-permeability pore volume into a single late-time system volume ($V_L = V_u + V_d + V_{p1}$) with pressure P_L. I assume 1-D, isothermal single-phase gas flow within the low-permeability layers in the *z*-direction (perpendicular to layering). After a sufficient time, V_L and V_{p2} reach pressure equilibrium at P_{eqb} (Figure 2.7c). We modify the Terzaghi (1943) equation as presented by Craig (2004) for 1-D dimensionless pressure dissipation:

$$\ln\left|\frac{P_L(t)-P_{eqb}}{P_{conv}-P_{eqb}}\right| \approx \frac{-9.872k_2t}{\phi_2\overline{\mu C}_L h_2^2} - 0.2098, \quad for \ \frac{P_L(t)-P_{eqb}}{P_{conv}-P_{eqb}} < 0.6 \qquad [2.12]$$

Equation [2.12] is valid for $\frac{P_L(t)-P_{eqb}}{P_{conv}-P_{eqb}} < 0.6$. $\overline{\mu C}_L$ is the average viscosity-compressibility product evaluated at P_{eqb}. k_2 is calculated by determining the best-fit linear slope (m_L) to $ln\left|\frac{P_L(t)-P_{eqb}}{P_{conv}-P_{eqb}}\right|$ versus time (Figure 2.9):

$$k_2 = -\frac{\phi_2(\overline{\mu C})_L h_2^2}{9.872} m_L \quad [2.13]$$

To calculate the permeability of the low-permeability layer (k_2), the porosity (ϕ_2) and thickness (h_2) must be known. The effective vertical permeability of the core (2V) is also calculated using the standard approach described by Dicker and Smits (1988) (Eq. [2.10], **Figure 2.4**): and is found to be $2.3x10^{-21}m^2$ (Bhandari et al *in review*). If this sample is composed of interbedded layers of high and low-permeability material, then this permeability equals the weighted harmonic average of layer permeabilities (k_1 and k_2):

$$k_V = \frac{k_1 k_2}{k_2 + (k_1 - k_2)\left[\frac{\gamma(1-\omega)}{\gamma(1-\omega)+\omega}\right]} \quad [2.14]$$

Equations [2.13] and [2.14] are combined to estimate the thickness of the low-permeability layer:

$$h_2 = \sqrt{-\frac{9.872}{m_L \phi_2 (\overline{\mu C})_L} \frac{k_1\left[\frac{\gamma(1-\omega)}{\gamma(1-\omega)+\omega}\right]}{\left(\frac{k_1}{k_V} - \left[\frac{\omega}{\gamma(1-\omega)+\omega}\right]\right)}} \quad [2.15]$$

Layer thickness depends on the porosity and permeability in the low permeability material.

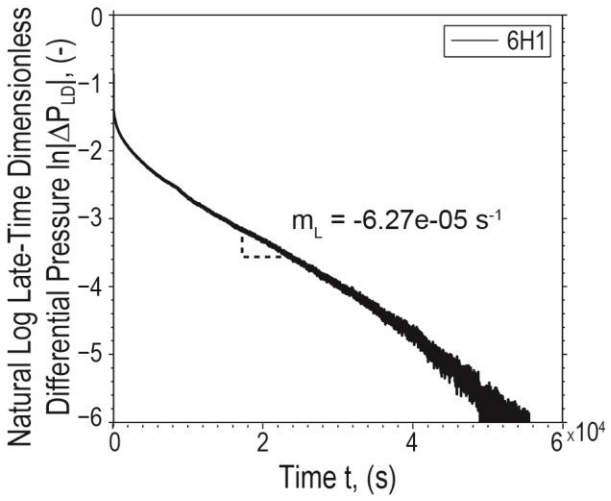

Figure 2.9 Late-Time dissipation slope (m_L) from the natural log of dimensionless late-time differential pressure ($\Delta P_{LD} = \frac{P_L - P_{eqb}}{P_{conv} - P_{eqb}}$) versus time. m_L is measured from straight-line portion after 90% decay in the late-time differential pressure ($\Delta P_{LD} = 0.1$).

MODEL RESULTS & DISCUSSION

9 equations describe the relationship between layer thickness ([2.6], [2.7], [2.8], [2.15]), porosity ([2.2], [2.8]), and permeability ([2.11], [2.13], [2.14]) with 11 unknown parameters: $H_1, H_2, h_2, N_2, \phi_1, \phi_2, \omega, \gamma, k_1, k_2, k_V$. I first consider the case where the layer porosities are the same and equal to the bulk porosity ($\phi_1 = \phi_2 = \phi_B = 6.9\%, \gamma = 1$). For this case, k_1 can be calculated directly (Eq. [2.11]) and is equal to $1.9x10^{-19}m^2$. To calculate k_2, we must know the layer thickness (Eq. [2.13]). If we assume a layer thickness of 5 mm as is observed in the CT images, then we calculate k_2 to be $2.8x10^{-23}m^2$. An alternative approach to calculate k_2 is to use the vertical permeability measurement ($k_V = 2.3x10^{-21}m^2$) and Eq. [2.15]. In this case, we find that the resultant layer permeability (k_2) is $1.2x10^{-21}m^2$ and layer thickness (h_2) is 3.3 cm for the low-

permeability layers. However, this individual layer thickness implies that 98% of the total rock is composed of the low-permeability material, which we argue to be physically unreasonable.

Model Sensitivity:

In fact, we do not know the porosity of the individual layers and the vertical permeability measured is from a level that is not identical to the location of the layer where we measured the horizontal permeability. We explore the effects of different layer porosities (γ) in Figure 2.10. Permeability and layer thickness increase in the low-permeability material for larger values of γ (Figure 2.10). We illustrate that vertical permeability must be $\lesssim 5\,x10^{-22}m^2$ because smaller k_V values produce more sensible layer thickness values (Figure 2.11). This is because CT images show that there is at least one complete low-permeability layer ~ 0.5 cm thick (Figure 2.1). This corresponds to k_2 values between $\sim 5x10^{-23}m^2$ and $\sim 2x10^{-22}m^2$ and γ between ~0.2 and 0.7 (Figure 2.11).

This range of model parameters yields a reasonable match to the experimental pulse-decay reservoir pressure time-series data (Figure 2.12). These γ values of indicate that the high-permeability layers have lower porosity than the low-permeability layers, which means that permeability and porosity are de-coupled (not proportional). This is not necessarily unreasonable because mudrock reservoirs (including the Barnett Shale) can have weak porosity-permeability correlations for a variety of reasons such as lithological heterogeneity and differences in laboratory methods/ sample preparation (Passey et al. 2010; Wang et al. 2009; Loucks et al. 2009). Furthermore, these γ values may suggest that the high-permeability layers behave as carrier beds that assist in the drainage of the low-permeability layers.

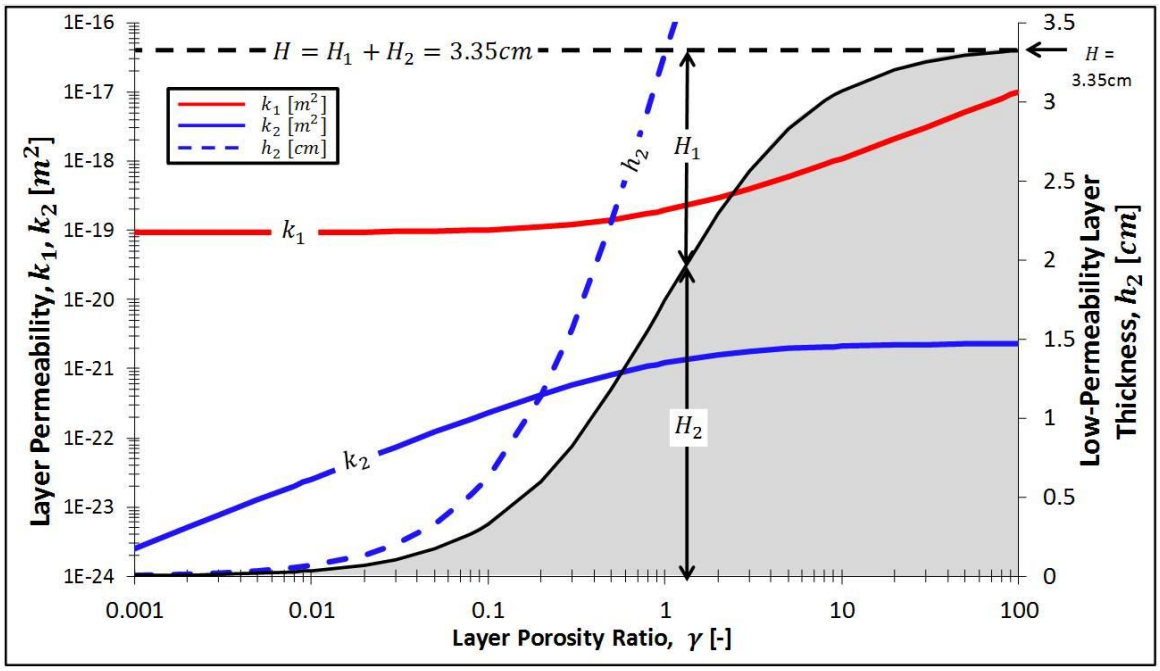

Figure 2.10 Layer permeabilities (k_1, k_2) and low-permeability layer thickness (h_2) as a function of layer porosity ratio ($\gamma = \phi_1/\phi_2$). Gray-filled area indicates the cumulative thickness of low-permeability layers (H_2) versus the high-permeability layers (H_1). The combined thickness of all layers (H) is 3.35cm. Note that the number of low-permeability layers is a fraction less than one ($N_2 \approx 0.8$) for $\gamma > 0.3$ because the individual layer thickness is larger than the cumulative layer thickness in the low-permeability material ($h_2 > H_2$). h_2 exceeds the total model thickness H when γ is greater than 1. Layer thickness values observed in X-ray CT scanning (**Figure 2.1**a) ranged between 0.5 and 1.5 cm. Plot generated using $\omega = 0.48$ for the fraction of total pore volume residing in the high-permeability layers, $\phi_B = 6.9\%$ for bulk porosity, and $k_V = 2.3x10^{-21}m^2$ for the vertical permeability.

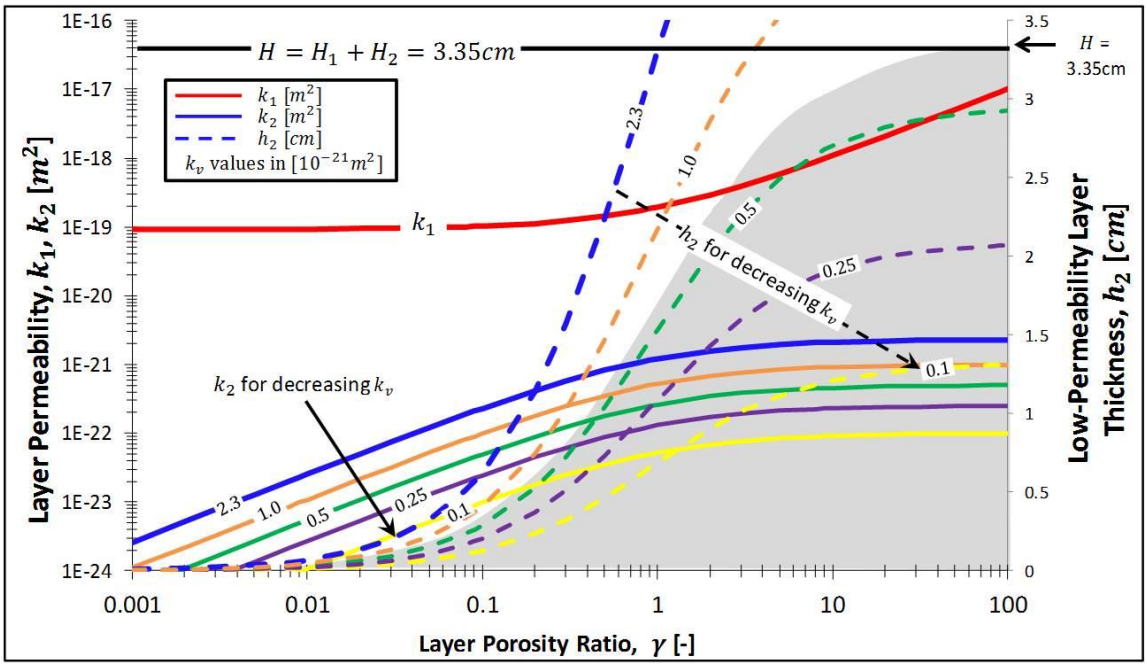

Figure 2.11 Influence of vertical permeability on the layer permeability (k_1, k_2) and low-permeability layer thickness (h_2) versus layer porosity ratio ($\gamma = \phi_1/\phi_2$) presented in Figure 2.10. Posted values indicate the value of k_V in $10^{-21}m^2$ used to calculate k_2 (solid lines) and h_2 (dashed lines). The model predicts as least one complete low-permeability layer ($N_2 \geq 1$) when $k_V < 0.5x10^{-21}m^2$.

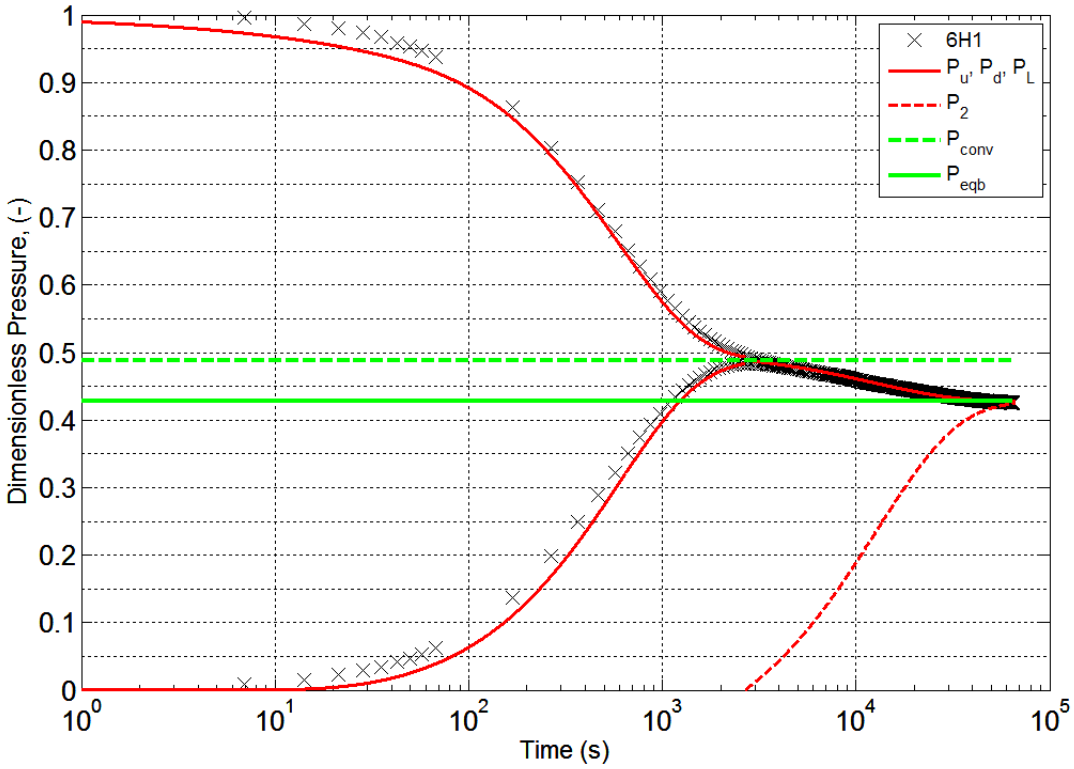

Figure 2.12 6H1 experimental pulse-decay data (X's) versus analytical model. Solid red lines depict reservoir pressure. Dashed green line denotes the convergence pressure (P_{conv}). Solid green line denotes the final equilibrium pressure (P_{eqb}). Early-time ($t < t_{conv}$) reservoir pressure was generated using the early-time model ($k_H = 92\ x10^{-21}m^2$), while late-time pressure was generated with the late-time model and $k_V = [2.3]x10^{-21}m^2$. Dashed red line depicts average pressure within the low-permeability layers predicted by late-time model. Model parameters: $\phi_B = 6.9\%$, $\omega = 0.48$, $m_L = -6.27\ x10^{-5}s^{-1}$, $V_u = 2.120\ cc$, $V_d = 1.763\ cc$, $D = 3.784cm$, $L = 1.764cm$. $R^2 = 0.88$ for the late-time analytical model versus experimental data.

Model vs. Matrix Characterization

The core sample is composed of silty-claystone layers and claystone layers (**Figure 2.1**). Dual-permeability modeling indicates that one lithology has substantially higher permeability, but relatively less porosity. My goal is to illustrate which lithology, the silty-claystone or the claystone, corresponds to the "high-permeability" layers.

Vitrinite reflectance data ($VR_o = 1.89\%$, **Table 2.3**) indicates that 6H1 organic matter is in the gas-generation thermal maturity window (Pollastro et al. 2007). At this maturity level, organic matter typically features small "nanopores" ($r < 1x10^{-8}m$) (Loucks et al. 2009), which we observed in high-resolution SEM images on an ion-milled surface (Figure 2.2). This is important, because Barnett Shale porosity principally resides within organic matter pores (Jarvie et al. 2007; Hickey et al. 2007; Wang et al. 2009; Loucks et al. 2007).

In the claystone, organic matter is highly distributed and compacted within the finer-grained material (**Figure 4.9**, **Figure 4.10**, **Figure 4.11**) with well-developed organic matter hosted pores. In the silty-claystone, organic matter appears as stringy "organo-mineralic aggregates" (**Figure 4.20**, **Figure 4.21**) (Macquaker 1994), angular woody particles, and in forms with "spongey" organic matter pores. I interpreted approximately twice as much organic matter in the claystone than the silty-claystone. Therefore, I argue that the claystone has higher layer porosity due to the greater abundance of organic matter (recall that $\omega = 0.48$ indicates that ~50% of the total pore volume resides in the low-permeability material). If the claystone has greater porosity, the previous dual-permeability result ($\gamma < 1$, **Figure 2.10**) means that the claystone also has lower permeability. Micro-CT scanning did not reveal visible micro-fractures (Figure 2.1) in the core sample or silty-claystone layers. This potentially means that a fracture-

related feature is below the micro-CT resolution. I observed a small number of micro-fractures in thin-section, but we interpret that these fractures are due to disturbance during thin-section preparation because they lacked mineral cement (Gale et al. 2007) and occurred near the trimmed edge of the thin-section or were filled with impregnation epoxy (see **Figure 4.20** in the supplemental petrography appendix (Ch. 4.4A)). However, based on previous pulse-decay experiments we conducted in naturally fractured core samples, we argue that the pulse-decay "convergence" time-scale observed for 6H1 is too slow to allow large through-going micro-fractures. In addition, the "dual-timescale" response in 6H1 persists at higher stresses (Bhandari et al. *in review*). Therefore, we need an alternative (non-fractured) explanation for high-permeability pathways in the silty-claystone to match dual-permeability model results.

I hypothesize that the silty-claystone provided an initially large, open, inter-connected pore-system of inter-granular porosity that was later filled with bitumen. Schneider et al. (2011) show that silt-fraction correlates to increased porosity preservation and higher permeability in clay-silt mixtures. Permeability would be higher within the silty-claystone because the spongey texture of the bitumen pores are well-connected (Loucks et al. 2014), and the lower volume fraction of elognate clay minerals in the silty-claystone means that gas molecules have a less tortuous path than they would have in the claystone (Figure 2.14). Permeability models that depict mudrocks as a "bundle of tubes" (Javadpour 2009) generally predict that $k \propto r^2$. At any given pore size, apparent flow-through permeability will decrease as tortuosity (path length) increases. Therefore, the conceptual expectation is that a well-connected sponge-like network of organic matter pores would have higher permeability than a more isolated one (e.g., migrated bitumen versus depositional kerogen).

Loucks and Reed (2014) report that migrated organic matter (bitumen) can have a spongey, highly-connected pore system, that they suggest provides a more permeable network than depositional kerogen. I observed evidence for post-depositional organic matter migration into inter-granular pore-space of the silty-claystone in the form of diagenetic dolomite rhombs impinging on spongey organic material (Figure 2.13). The bulk mineralogy of 6H1 is siliceous (~66% quartz and clay minerals, **Table 2.2**) and the silty-claystone is significantly coarser (silt-sized grains are larger and more abundant) than the claystone (**Figure 2.2**). Davies et al. (1991) report that pore size scales with detrital silt grain size in Devonian shales, while Bustin et al (2008) report more micro-scale pores in silica rich mudrocks. Scanning electron microscopy (SEM) provides high-resolution images of texture and pore-systems, but has an extremely limited field-of-view $\lesssim$ (250 x 250) μm^2. This limitation is not absolute because multiple SEM images can be combined to create a large 2D image (Milliken 2013) or 3-D image from successively milled surfaces (Sondergeld et al. 2010). However, it quickly becomes impractical to attempt to define the entire volume of a core sample at this resolution. This is precisely why flow-through permeability experiments are so valuable because they provide a means to remotely sense the entire core pore volume. Therefore it is naturally complementary to integrate pulse-decay, micro-computed x-ray tomography, and scanning electron microscopy analyses.

I integrated dual-permeability modeling and matrix characterization to replicate the "dual-timescale" pulse-decay behavior observed in a layered Barnett Shale core sample to define the permeability of the silty-claystone and claystone layers. However, I emphasize that I cannot definitely state that the silty-claystone is the higher permeability lithology.

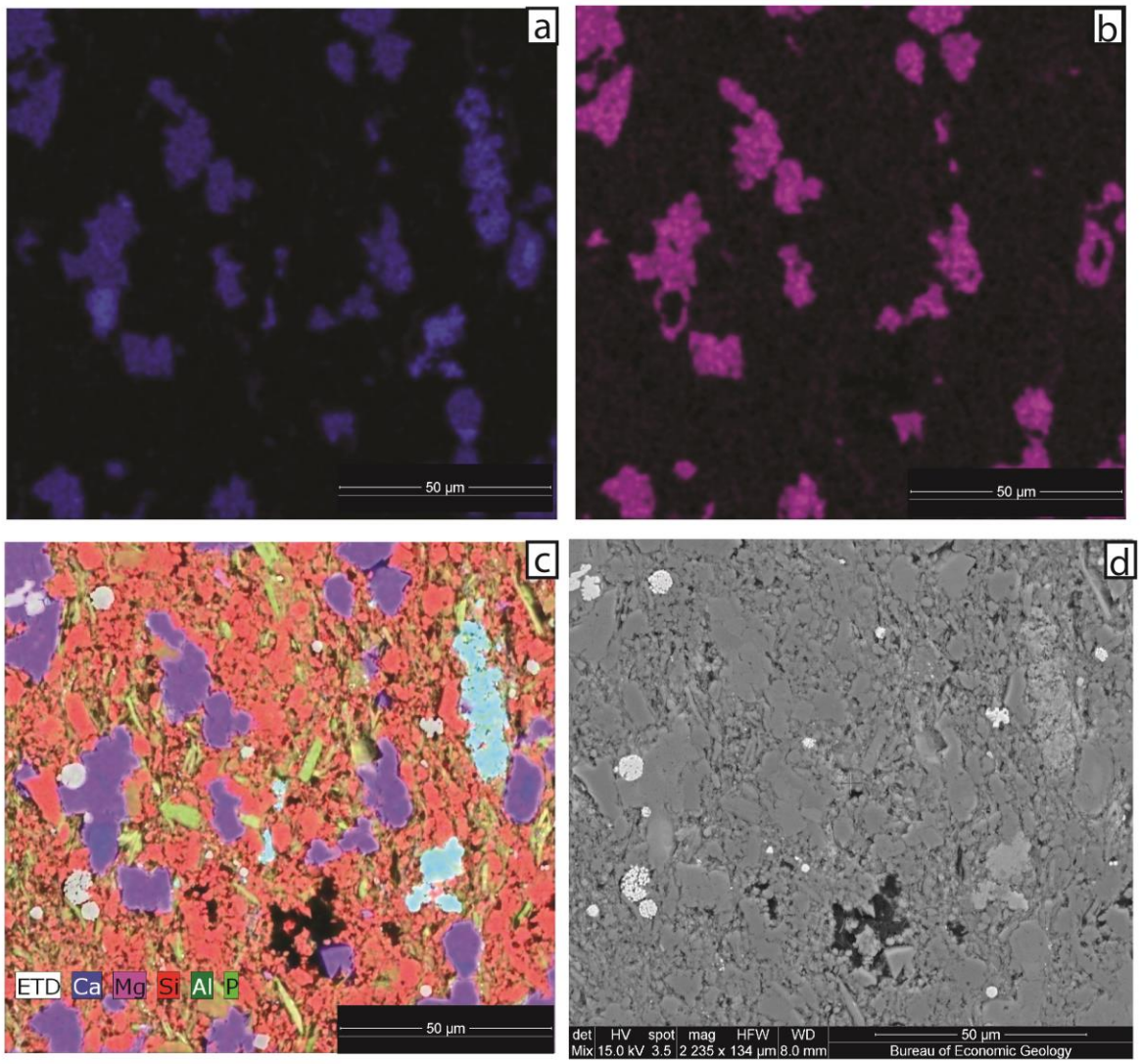

Figure 2.13 X-ray maps and scanning electron micrographs in the siltsone facies showing diagenetic dolomite overgrowths. The large black area in **c** and **d** is impregnation epoxy. **a.** Calcium map. **b.** Magnesium map. **c.** Magnesium content increases towards the edge of the calcite/dolomite grains. This suggests dolomite over-growth. **d.** SEM image shows pointed dolomite rhombs impinging on organic material.

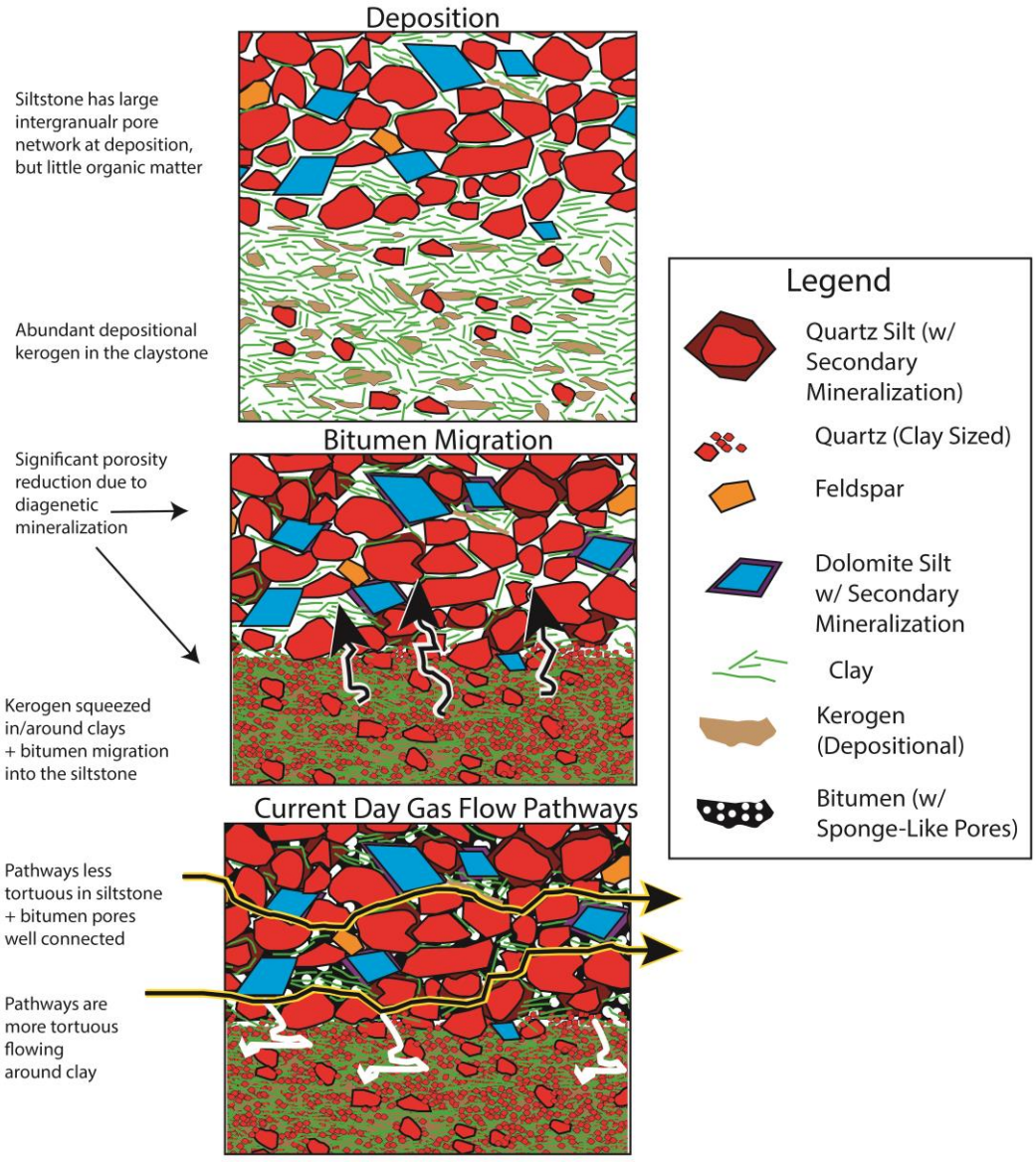

Figure 2.14 Conceptual model for pore-space evolution in the silty-claystone. Bitumen migrates into the silty-claystone, leaving a well-connected, sponge-like network resulting in higher flow-through permeability than the claystone. The claystone permeability is lower because the clay minerals significantly increase tortuousity.

Implications

I demonstrated that mm-scale layering can induce more complicated gas transport behavior. This layering effect may have implications on core-sampling strategies for reservoir characterization. In particular, there may be a selection bias against "heterogeneous" cores in favor of more "homogeneous" ones. After all, reservoir engineers routinely request permeability values of "pure" lithologies to populate reservoir models. Reservoir engineers may simplify fluid flow through heterolithic/heterogeneous intervals using a variety of standard weighting techniques (Ertekin et al. 2001). However, these simplifications may not capture potentially important flow behavior arising from fine-scale heterogeneity. For example, in thinly bedded or laminated reservoirs, layer spacing and porosity/permeability can influence permeability anisotropy and control drainage lengths. Therefore, I think that flow-through permeability experiments in naturally heterogeneous intervals could provide rich insight into the role of heterogeneity on transport and help calibrate upscaling/simplification efforts.

SUMMARY

I presented a simple approach to explain the first order observation of dual-timescale flow behavior in horizontal Barnett Shale cores using a layered dual-permeability model. This dual-permeability model workflow provides a simple means of decomposing the gas transport/storage contribution of two lithologies within a heterogeneous core. The model is composed of high and low permeability material. Simultaneous application of experimentally-derived horizontal and vertical permeability constraints overcomes the non-uniqueness inherent to dual-permeability modeling. The new insight is that the Barnett Shale has dual-timescale permeability behavior due to mm-scale lithologic layering. By relating experimental permeability to sub core-scale

heterogeneity, this work contributes towards better understanding in-situ gas flow at the reservoir scale.

CONCLUSIONS

1) The dual-timescale pulse-decay behavior we observe in our Barnett core sample is caused by lithologic layering.

2) The dual-permeability model suggests that porosity and permeability are decoupled, wherein the high-permeability layers have relatively low porosity and low-permeability layers have relatively high porosity.

3) The silty-claystone layers potentially have higher permeability, but lower porosity than the claystone.

4) The vertical permeability constraint is a novel feature of our dual-permeability model and helps overcome the non-uniqueness inherent to dual-permeability modeling.

5) Pulse-decay permeability tests should be integrated with micro-computed tomography and thin section/scanning electron microscopy to enhance the quality of dual-permeability modeling.

APPENDIX 2A: EARLY-TIME APPROXIMATE SOLUTION

Dicker and Smits (1988) give the analytical solution for upstream, downstream, and differential reservoir pressures versus time for a pulse-decay apparatus with fixed volume reservoirs upstream and downstream, and where fluid flows uniformly across the entire cross-sectional area of the core. We modify these solutions because our early-time model (Figure 2.7a) has gas flowing through the high-permeability layers only. Permeability in the high-permeability layers (k_1) is:

$$k_1 = k_H \frac{\omega}{[(1-\omega)\gamma+\omega]} \quad [2.16]$$

Equation [2.16] equates steady-state flow through the homogeneous core with effective permeability k_H to flow through the high-permeability layers. The modified governing equation, initial conditions, and boundary conditions are:

Governing Equation:

$$\frac{\partial \mathrm{P}_1}{\partial \mathrm{t}} = \frac{k_1}{\phi_1 \mu C} \frac{\partial^2 \mathrm{P}_1}{\partial x^2}, \quad 0 < x < L, t > 0 \quad [2.17]$$

Initial Conditions:

$$\mathrm{P_u}(0) = P_{u0} \quad [2.18]$$

$$\mathrm{P_d}(0) = P_0 \quad [2.19]$$

$$\mathrm{P}_1(x, 0) = P_0, \quad 0 < x < L \quad [2.20]$$

$$\mathrm{P}_2(x, 0) = P_0, \quad 0 < x < L \quad [2.21]$$

Boundary Conditions:

$$\mathrm{P_u}(t) = P_1(x = 0, t), \quad t > 0 \quad [2.22]$$

$$\mathrm{P_d}(t) = P_1(x = L, t), \quad t \geq 0 \quad [2.23]$$

$$\frac{\partial \mathrm{P_u}}{\partial \mathrm{t}} = \frac{k_1}{\phi_1 \overline{\mu C}_E L} \frac{V_{p1}}{V_u} \frac{\partial P_1}{\partial x}, \quad x = 0, t > 0 \quad [2.24]$$

$$\frac{\partial \mathrm{P_d}}{\partial \mathrm{t}} = -\frac{k_1}{\phi_1 \overline{\mu C}_E L} \frac{V_{p1}}{V_d} \frac{\partial P_1}{\partial x}, \quad x = L, t > 0 \quad [2.25]$$

$$\mathrm{P_u(t)} = \mathrm{P_1(x,t)} = \mathrm{P_d(t)} = \mathrm{P_{eqb}}, \quad 0 < x < L, t = \infty \quad [2.26]$$

$$\mathrm{P}_2(\mathrm{x},\mathrm{t}) = P_0, \quad 0 < x < L, t \geq 0 \tag{2.27}$$

The modified solution to the these equations as a function of dimensionless time (t_D) is given by Eq. [2.28], where $\overline{\mu C}_E$ is the average viscosity compressibility product evaluated at P_{conv}:

$$t_D = \frac{k_1[(1-\omega)\gamma+\omega]}{\omega\phi_B\overline{\mu C}_E L^2}t \tag{2.28}$$

Upstream pressure:

$$\frac{P_u(t_D)-P_0}{P_{u0}-P_0} = \frac{b_E}{a_E+b_E+a_Eb_E} + 2\sum_{m=1}^{\infty}\frac{\exp(-t_D\theta_m^2)(a_Eb_E^2+a_E\theta_m^2)}{[(\theta_m^4+\theta_m^2(a_E+a_E^2+b_E+b_E^2)+a_Eb_E(a_E+b_E+a_Eb_E)]cos\theta_m} \tag{2.29}$$

Downstream pressure:

$$\frac{P_d(t_D)-P_0}{P_{u0}-P_0} = \frac{b_E}{a_E+b_E+a_Eb_E} + 2\sum_{m=1}^{\infty}\frac{\exp(-t_D\theta_m^2)(a_Eb_E^2-b_E\theta_m^2)}{[(\theta_m^4+\theta_m^2(a_E+a_E^2+b_E+b_E^2)+a_Eb_E(a_E+b_E+a_Eb_E)]cos\theta_m} \tag{2.30}$$

Differential pressure:

$$\frac{P_u(t_D)-P_d(t_D)}{P_{u0}-P_0} = 2\sum_{m=1}^{\infty}\frac{\exp(-t_D\theta_m^2)a_e(b_E^2+\theta_m^2)-(-1)^m b_E[(a_E^2+\theta_m^2)(b_E^2+\theta_m^2)]^{0.5}}{[(\theta_m^4+\theta_m^2(a_E+a_E^2+b_E+b_E^2)+a_Eb_E(a_E+b_E+a_Eb_E)]} \tag{2.31}$$

a_E and b_E are dimensionless early-time pore volume to reservoir volume ratios:

$$a_E = V_{p1}/V_u \tag{2.32}$$

$$b_E = V_{p1}/V_d \tag{2.33}$$

and θ_m are the roots to the following equation:

$$tan\theta = \frac{(a_E+b_E)\theta}{(\theta^2-a_Eb_E)} \tag{2.34}$$

APPENDIX 2B: LATE-TIME APPROXIMATE SOLUTION

The 1-D pressure diffusion equation describes gas flow within the low-permeability layers (Eq. [2.35]). The initial pressure within the low-permeability layers is P_0 (Eq. [2.36]). At the layer edges ($z = \pm\frac{h_2}{2}$), I assume that the boundary pressure is approximately constant and equal to the final equilibrium pressure P_{eqb} (Eq. [2.37]). By symmetry, there is a no-flow boundary at $z = 0$ (Eq. [2.38]). After a long-time, P_2 asymptotically approaches P_{eqb} (Eq. [2.39]).

Governing Equation:

$$\frac{\partial P_2}{\partial t} = \frac{k_2}{\phi_2 \mu C}\frac{\partial^2 P_2}{\partial z^2}, \quad -\frac{h_2}{2} \le z \le \frac{h_2}{2}, t > t_{conv} \qquad [2.35]$$

Initial Conditions:

$$P_2(z, t_{conv}) = P_0, \quad -\frac{h_2}{2} \le z \le \frac{h_2}{2} \qquad [2.36]$$

Boundary Conditions:

$$P_2(z, t) = P_{eqb}, \qquad z = \pm\frac{h_2}{2}, \ t > t_{conv} \qquad [2.37]$$

$$\frac{\partial P_2}{\partial z} = 0, \quad z = 0, t > t_{conv} \qquad [2.38]$$

$$P_2(z, t) = P_{eqb}, \qquad t = \infty \qquad [2.39]$$

I modify Terzaghi's (1943) solution for the dimensionless layer pressure within the low-permeability layers:

$$\frac{P_2(z, T_v) - P_{eqb}}{P_0 - P_{eqb}} = \sum_{m=0}^{m=\infty} \frac{2}{M} \sin\left(\frac{2Mz}{h_2}\right) \exp(-M^2 T_v) \qquad [2.40]$$

Where T_v is the dimensionless time-factor (Eq. [2.41]) and M is an indicial replacement (Eq. [2.42]).

$$T_v = \frac{4k_2 t}{\phi_2 \overline{\mu C}_l h_2^2} \qquad [2.41]$$

$$M = 2m + 1 \qquad [2.42]$$

Pressure in the late-time system (P_L) is a function of average pressure in the low-permeability layers ($\bar{P}_2$):

$$P_L(t) = P_{eqb}\left(\frac{V_L+V_{p2}}{V_L}\right) - \bar{P}_2(t)\left(\frac{V_{p2}}{V_L}\right) \quad [2.43]$$

Where average layer pressure ($\bar{P}_2$) is:

$$\frac{\bar{P}_2(t)-P_{eqb}}{P_0-P_{eqb}} = \sum_{m=0}^{m=\infty} \frac{\exp(-M^2 T_v)}{M^2} \quad [2.44]$$

Equations [2.35],[2.43], and [2.44] are combined the give the $\ln\left|\frac{P_L(t)-P_{eqb}}{P_{conv}-P_{eqb}}\right|$ versus time:

$$\ln\left|\frac{P_L(t)-P_{eqb}}{P_{conv}-P_{eqb}}\right| \approx \frac{-9.872 k_2 t}{\phi_2 \overline{\mu C}_L h_2^2} - 0.2098 \quad [2.45]$$

We modified the Terzaghi (1943) equation as presented in *Craig's Soil Mechanics, 7th Edition* (Craig 2004) to derive Equation [2.45], which is valid for $\frac{P_L(t)-P_{eqb}}{P_{conv}-P_{eqb}} < 0.6$.

ACKNOWLEDGEMENTS

This project was funded by a Shell-University of Texas Unconventional Research (SUTUR) grant. I thank Kitty Milliken, Bob Loucks, Tingwei Ko, Joel Lunsford, and Maxwell Pommer, and Patrick Smith for their assistance and suggestions with petrography (optical, scanning electron, and energy-dispersive x-ray mapping). I thank Athma Bhandari and Peter Polito for their assistance with the pulse-decay permeability experiments. Finally, I thank the anonymous reviewers for their thoughtful feedback and suggestions.

REFERENCES

(API), A.P.I.: Recommended Practices for Core Analysis (2nd Edition). In: Exploration and Production Department, vol. Recommended Practice 40. API Publishing Services, 1220 L Street, N.W., Washington, D.C. 20005, (1998)

Benson, P.M., Meredith, P.G., Schubn|el, A.: Role of void space geometry in permeability evolution in crustal rocks at elevated pressure. Journal of Geophysical Research **111**, B12203 (2006)

Brace, W.F., Walsh, J.B., Frangos, W.T.: Permeability of Granite Under High Pressure. Journal of Geophysical Research **73**(6), 2225-2236 (1968)

Bustin, R.M., Bustin, A.M.M., Cui, A., Ross, D., Pathi, V.M.: Impact of Shale Properties on Pore Structure and Storage Characteristics, 2008/1/1/

Civan, F., Rai, C., Sondergeld, C.: Shale-Gas Permeability and Diffusivity Inferred by Improved Formulation of Relevant Retention and Transport Mechanisms. Transport in Porous Media **86**(3), 925-944 (2011). doi:10.1007/s11242-010-9665-x

Civan, F., Rasmussen, M.L.: Parameters of Matrix/Fracture Immiscible-Fluids Transfer Obtained by Modeling of Core Tests. SPE Journal **17**(2), pp. 540-554 (2012). doi:10.2118/104028-pa

Cui, X., Bustin, A.M.M., Bustin, R.M.: Measurements of gas permeability and diffusivity of tight reservoir rocks: different approaches and their applications. Geofluids **9**(3), 208-223 (2009). doi:10.1111/j.1468-8123.2009.00244.x

Dicker, A.I., Smits, R.M.: A Practical Approach for Determining Permeability From Laboratory Pressure-Pulse Decay Measurements. Paper presented at the International Meeting on Petroleum Engineering, Tianjin, China, 01/01/1988

EIA: Technically Recoverable Shale Oil and Shale Gas Resources: An Assessment of 137 Shale Formations in 41 Countries Outside the United States. In: Administration, U.S.E.I. (ed.). U.S. Department of Energy (DOE), (2013)

Ertekin, T., Abou-Kassem, J.H., King, G.R.: Basic Applied Reservoir Simulation. SPE Textbook Series vol. Vol. 7. Society of Petroleum Engineers, (2001)

Fathi, E., Akkutlu, I.Y.: Matrix Heterogeneity Effects on Gas Transport and Adsorption in Coalbed and Shale Gas Reservoirs. Transport in Porous Media **80**(2), 281-304 (2009). doi:10.1007/s11242-009-9359-4

Freeman, C.M., Moridis, G.J., Blasingame, T.A.: A Numerical Study of Microscale Flow Behavior in Tight Gas and Shale Gas Reservoir Systems. Transport in Porous Media **90**(1), 253-268 (2011). doi:10.1007/s11242-011-9761-6

Gale, J.F., Reed, R.M., Holder, J.: Natural fractures in the Barnett Shale and their importance for hydraulic fracture treatments. AAPG Bulletin **91**(4), 603-622 (2007)

Geiser, P., Lacazette, A., Vermiyle, J.: Beyond 'dots in a box'; an empirical view of reservoir permeability with tomographic fracture imaging. First Break **30**(7), 63-69 (2012)

Grieser, W.V., Shelley, R.F., Johnson, B.J., Fielder, E.O., Heinze, J.R., Werline, J.R.: Data Analysis of Barnett Shale Completions. SPE Journal (2008). doi:10.2118/100674-pa

Hickey, J.J., Henk, B.: Lithofacies summary of the Mississippian Barnett Shale, Mitchell 2 T.P. Sims well, Wise County, Texas. AAPG Bulletin **91**(4), 437-443 (2007). doi:10.1306/12040606053

Holder, J., et al.: Laboratory Measurement of Permeability in Rock. In: al., C.e. (ed.) Key Questions in Rock Mechanics. Balkema, Rotterdam (1988)

Hsieh, P.A., Tracy, J.V., Neuzil, C.E., Bredehoeft, J.D., Silliman, S.E.: A transient laboratory method for determining the hydraulic properties of `tight' rocks--I. Theory. International Journal of Rock Mechanics and Mining Sciences & Geomechanics Abstracts **18**(3), 245-252 (1981). doi:10.1016/0148-9062(81)90979-7

Jannot, Y., Lasseux, D., Vize, G., Hamon, G.: A DETAILED ANALYSIS OF PERMEABILITY AND KLINKENBERG COEFFICIENT ESTIMATION FROM UNSTEADY-STATE PULSE-DECAY OR DRAW-DOWN EXPERIMENTS. Paper presented at the International Symposium of the Society of Core Analysts, Calgary, Canada, 10-12 September, 2007

Jarvie, D.M., Hill, R.J., Ruble, T.E., Pollastro, R.M.: Unconventional shale-gas systems: The Mississippian Barnett Shale of north-central Texas as one model for thermogenic shale-gas assessment. AAPG Bulletin **91**(4), 475-499 (2007). doi:10.1306/12190606068

Javadpour, F.: Nanopores and Apparent Permeability of Gas Flow in Mudrocks (Shales and Siltstone). Journal of Canadian Petroleum Technology(08) (2009). doi:10.2118/09-08-16-da

Jones, S.C.: A Technique for Faster Pulse-Decay Permeability Measurements in Tight Rocks SPE Formation Evaluation **12**(1), 19-26 (1997). doi:10.2118/28450-PA

Kamath, J., Boyer, R.E., Nakagawa, F.M.: Characterization of Core-Scale Heterogeneities Using Laboratory Pressure Transients. SPE Formation Evaluation **September** (1992)

Lee, J., Rollins, J.B., Spivey, J.P.: Pressure transient testing. Society of Petroleum Engineers, (2003)

Loucks, R.G., Ruppel, S.C.: Mississippian Barnett Shale: Lithofacies and depositional setting of a deep-water shale-gas succession in the Fort Worth Basin, Texas. AAPG Bulletin **91**(4), 579-601 (2007). doi:10.1306/11020606059

Luffel, D.L., Houston, R., Hopkins, C.W., Inc, S.A.H.a.A., Schettler, P.D.J.: Matrix Permeability Measurement of Gas Productive Shales. Paper presented at the 6th Annual Technical Conference and Exhibition of the Society of Petroleum Engineers, Houston, TX,

Mehmani, A., Prodanović, M., Javadpour, F.: Multiscale, Multiphysics Network Modeling of Shale Matrix Gas Flows. Transport in Porous Media **99**(2), 377-390 (2013). doi:10.1007/s11242-013-0191-5

Milliken, K., Choh, S.-J., Papazis, P., Schieber, J.: "Cherty" stringers in the Barnett Shale are agglutinated foraminifera. Sedimentary Geology **198**(3–4), 221-232 (2007). doi:http://dx.doi.org/10.1016/j.sedgeo.2006.12.012

Ning, X.: The measurement of matrix and fracture properties in naturally fractured low permeability cores using a pressure pulse method. Texas A&M University (1992)

Passey, Q.R., Bohacs, K., Esch, W.L., Klimentidis, R., Sinha, S.: From Oil-Prone Source Rock to Gas-Producing Shale Reservoir â□" Geologic and Petrophysical Characterization of Unconventional Shale-Gas Reservoirs. Paper presented at the International Oil and Gas Conference and Exhibition in China, Beijing, China, 01/01/2010

Patzek, T.W., Male, F., Marder, M.: Gas production in the Barnett Shale obeys a simple scaling theory. Proceedings of the National Academy of Sciences (2013). doi:10.1073/pnas.1313380110

Roduit, N.: MicroVision: Image analysis toolbox for measuring and quantifying components of high-definition images. In. (2008)

Rowe, H., Hughes, N., Robinson, K.: The quantification and application of handheld energy-dispersive x-ray fluorescence (ED-XRF) in mudrock chemostratigraphy and geochemistry. Chemical Geology **324–325**(0), 122-131 (2012). doi:http://dx.doi.org/10.1016/j.chemgeo.2011.12.023

Rwechungura, R.W., Dadashpour, M., Kleppe, J.: Advanced History Matching Techniques Reviewed, 2011/1/1/

Soeder, D.J.: Porosity and Permeability of Eastern Devonian Gas Shale. SPE Formation Evaluation(03) (1988). doi:10.2118/15213-pa

Sondergeld, C.H., Ambrose, R.J., Rai, C.S., Moncrieff, J.: Micro-Structural Studies of Gas Shales, 2010/1/1/

Terry, R.D., Chilingar, G.V.: Summary of "Concerning some additional aids in studying sedimentary formations," by M. S. Shvetsov. Journal of Sedimentary Research **25**(3), 229-234 (1955)

Terzaghi, K.: Theoretical Soil Mechanics. John Wiley & Sons, New York (1943)

Vega, B., Dutta, A., Kovscek, A.: CT Imaging of Low-Permeability, Dual-Porosity Systems Using High X-ray Contrast Gas. Transport in Porous Media **101**(1), 81-97 (2014). doi:10.1007/s11242-013-0232-0

Vermylen, J.: Geomechanical Studies of the Barnett Shale, Texas, USA. Stanford (2011)

Wang, F.P., Reed, R.M.: Pore Networks and Fluid Flow in Gas Shales. Paper presented at the SPE Annual Technical Conference and Exhibition, New Orleans, Louisiana, 01/01/2009

Warren, J.E., Root, P.J.: The Behavior of Naturally Fractured Reservoirs. Society of Petroleum Engineers Journal(September), 245-255 (1963)

Waters, G.A., Dean, B.K., Downie, R.C., Kerrihard, K.J., Austbo, L., McPherson, B.: Simultaneous Hydraulic Fracturing of Adjacent Horizontal Wells in the Woodford Shale, 2009/1/1/

CHAPTER 3: PULSE-DECAY BEHAVIOR OF FRACTURED CORES

Abstract

In this chapter, I describe pulse-decay experiments I conducted on a fractured cement core sample that I used to experimentally validate my dual-permeability fractured core model. I used class H Portland cement with no additives and constrained cement matrix properties by conducting steady-state and pulse-decay permeability tests on un-fractured cement cores. I generated a planar fracture using the Brazilian Disk method. I then present a workflow to interpret matrix and fracture properties from the pulse-decay data. Next, I illustrate the characteristic pulse-decay behavior of samples with the classical "sugar cube" geometry (Warren et al. 1963).

Table 3.1 Nomenclature

Symbol	Description and Dimensions*/Units
English Symbols	
A	Cross-sectional area of core (L^2, m^2)
A_c	Characteristic drainage surface area (L^2, m^2)
A_{meq}	Equivalent matrix-fracture contact surface area (L^2, m^2)
a	Ratio of pore volume to upstream reservoir volume (dimensionless)
a_E	Ratio of early pore volume to upstream reservoir volume (dimensionless)
b	Ratio of pore volume to downstream reservoir volume (dimensionless)
b_E	Ratio of early pore volume to downstream reservoir volume (dimensionless)
C	Gas compressibility ($M^{-1}L\,T^2$, Pa^{-1})
C_f	Gas compressibility in fractures ($M^{-1}L\,T^2$, Pa^{-1})
C_m	Gas compressibility in matrix ($M^{-1}L\,T^2$, Pa^{-1})
D	Diameter of core (L, m)
H	Thickness of model (with equal cross-sectional area to core of diameter D) (L, m)
h_{mx}	Thickness of matrix block in x-direction (L, m)
h_{my}	Thickness of matrix block in y-direction (L, m)
h_{mz}	Thickness of matrix block in z-direction (L, m)
$f(a,b)$	Eq. A15 in Dicker and Smits (1988) (rad^2)
k_{fH}	Effective horizontal permeability of fractured core (L^2, m^2)
k_H	Effective horizontal permeability of homogeneous core (L^2, m^2)
k_f	Permeability (isotropic) of fractures (L^2, m^2)
k_m	Permeability (isotropic) of matrix (L^2, m^2)
k_{mx}	Permeability of matrix in x-direction (L^2, m^2)
k_{my}	Permeability of matrix in y-direction (L^2, m^2)
k_{mz}	Permeability of matrix in z-direction (L^2, m^2)
k_V	Effective vertical permeability (L^2, m^2)
m_E	Early-time model dimensionless pressure dissipation slope (T^{-1}, s^{-1})
m_L	Late-time model dimensionless pressure dissipation slope (T^{-1}, s^{-1})
L	Length of core (L, m)
L_{meq}	Equivalent length of matrix (L, m)
N_F	Number of fractures in a given plane (dimensionless)
N_{FX}	Number of fractures in x-direction (dimensionless)
N_{FY}	Number of fractures in y-direction (dimensionless)
N_{FZ}	Number of fractures in z-direction (dimensionless)
$N_\perp$	Number of mutually orthogonal preferential flow-path planes (dimensionless)
P_C	Absolute (hydrostatic) confining pressure ($ML^{-1}T^{-2}$, Pa)
P_{conv}	Early-time reservoir convergence pressure ($ML^{-1}T^{-2}$, Pa)
P_D	Dimensionless pressure scaled between P_{u0} and P_0 (dimensionless)

Table 3.1, cont.

P_d	Pore pressure in downstream reservoir ($ML^{-1}T^{-2}$, Pa)
P_{eqb}	Late-time final equilibrium pressure ($ML^{-1}T^{-2}$, Pa)
P_L	Late-time system pressure ($ML^{-1}T^{-2}$, Pa)
P_p	Average pore pressure ($ML^{-1}T^{-2}$, Pa)
P_u	Pore pressure in upstream reservoir ($ML^{-1}T^{-2}$, Pa)
P_{u0}	Initial upstream reservoir pressure (after opening main valve) ($ML^{-1}T^{-2}$, Pa)
P_0	Initial system pore pressure ($ML^{-1}T^{-2}$, Pa)
$S.A._{meq}$	Equivalent surface area of matrix-fracture contact (L^2, m^2)
S_{fX}	Fracture spacing in x-direction (L, m)
S_{fY}	Fracture spacing in y-direction (L, m)
S_{fZ}	Fracture spacing in z-direction (L, m)
$\bar{s}$	Laplace transform variable
t	Time (T, s)
t_D	Dimensionless time (dimensionless)
t_{fD}	Dimensionless fracture time (dimensionless)
t_L	Late-time model time, $t_L = t - \tau_E$ (s)
V_B	Bulk volume of the core sample (L^3, m^3)
V_d	Downstream reservoir volume (L^3, m^3)
V_L	Late-time system volume (L^3, m^3)
V_{pE}	Pore volume at "early-time" reservoir convergence pressure (L^3, m^3)
V_{pB}	Total pore volume of core (L^3, m^3)
V_{pm}	Pore volume in matrix (L^3, m^3)
V_{pf}	Pore volume in fractures (L^3, m^3)
V_u	Upstream reservoir volume (L^3, m^3)
W	Width of model (with equal cross-sectional area to core of diameter D) (L, m)
w_f	Fracture aperture (L, m)
w_{fx}	Fracture aperture in x-direction (L, m)
w_{fy}	Fracture aperture in y-direction (L, m)
w_{fz}	Fracture aperture in z-direction (L, m)
x	Cartesian distance in horizontal flow direction (L, m)
y	Cartesian distance in horizontal plane, perpendicular to flow direction (L, m)
Z	Real gas deviation factor (dimensionless)
z	Cartesian distance in vertical direction (perpendicular to bedding) (L, m)
Greek Symbols	
α	Shape factor (L^{-2}, m^{-2})
ΔP	Differential pore pressure, $\Delta P = (P_u - P_d)$ ($ML^{-1}T^{-2}$, Pa)
ΔP_D	Dimensionless ΔP, $\Delta P_D = \Delta P/(P_{u0} - P_0)$ (dimensionless)
ΔP_L	Late-time model differential pressure, $\Delta P_L = (P_L - P_{eqb})$ ($ML^{-1}T^{-2}$, Pa)
ΔP_{LD}	Dimensionless ΔP_L, $\Delta P_{LD} = \Delta P_L/(P_{conv} - P_0)$ (dimensionless)

Table 3.1, cont.

λ_f	Transmissibility ratio of fractures versus matrix (dimensionless)
μ	Dynamic gas viscosity (Pa s)
$\overline{\mu C}$	Average viscosity-compressibility product (T, s)
$\overline{\mu C}_E$	Average viscosity-compressibility product in early-time model (T, s)
$\overline{\mu C}_L$	Average viscosity-compressibility product in late-time model (T, s)
μ_f	Dynamic gas viscosity in fractures ($ML^{-1}T^{-1}$, Pa s)
μ_m	Dynamic gas viscosity in matrix ($ML^{-1}T^{-1}$, Pa s)
$\bar{\mu}_{m,f}$	Average dynamic viscosity between matrix and fractures ($ML^{-1}T^{-1}$, Pa s)
t_{conv}	Timescale for initial reservoir pressure convergence (T, s)
t_{eqb}	Timescale for system to reach final equilibrium pressure (T, s)
τ_f	Characteristic timescale ratio of fractures versus matrix: $\tau = t_{eqb}/t_{conv}$ (-)
ϕ	Porosity (fraction)
ϕ_E	Apparent bulk porosity of entire core at early-time (fraction)
ϕ_B	Bulk porosity of entire core (fraction)
ϕ_f	Intrinsic porosity of fractures (fraction)
ϕ_m	Intrinsic porosity of matrix (fraction)
Φ_1	Fraction of "primary" matrix pore volume to bulk volume of core (fraction)
Φ_2	Fraction of "secondary" fracture pore volume to bulk volume of core (fraction)
ω_f	Fraction of total pore volume residing in the fractured domain (fraction)
Common Subscripts	
B	Bulk core property
D	Dimensionless
E	Early-time system property
L	Late-time system property
$conv$	Pertaining to early-time reservoir pressure convergence
d	Pertaining to downstream reservoir
eqb	Pertaining to late-time equilibrium pressure
f	Pertaining to fractures
m	Pertaining to matrix
p	Pertaining to pore volume (within core)
u	Pertaining to upstream reservoir
0	Original value
1	Primary domain
2	Secondary domain
Common Operators	
Σ	Summation
$\bar{}$	Average

* *M*: mass, *L*: length, *T*: time, *Θ*: temperature, (-): integer

SAMPLE CHARACTERIZATION

Preparation of Cement Core Samples

Cement core samples were prepared following the protocol of API RP-10B (2005). The cement slurry was prepared using Class H Portland cement with no additives and tap water. The cement was cured inside 1.0 inch diameter by 6.0 inch long flexible plastic tubing at 60 degrees C for three days prior to testing. The intact core-sample CI-01 was cut from the cured cement tube and oven-dried to remove water imbibed during cutting. After characterizing porosity and permeability of intact matrix, I used the Brazilian Disk method (Hondros 1959) (Figure 3.1a) to generate a through-going tensile fracture plane in CI-01. The broken halves of the sample were slightly offset and lightly sanded flush. Black electrical tape was tightly wrapped around the core sample to provide integrity and improve the seal between the core sample and the Viton sleeve inside the pulse-decay apparatus. I refer to this fractured sample as CF-01 (Figure 3.1b). I idealize CF-01 as intact cement matrix embedded with a single planar fracture with constant aperture and permeability (Figure 3.1c).

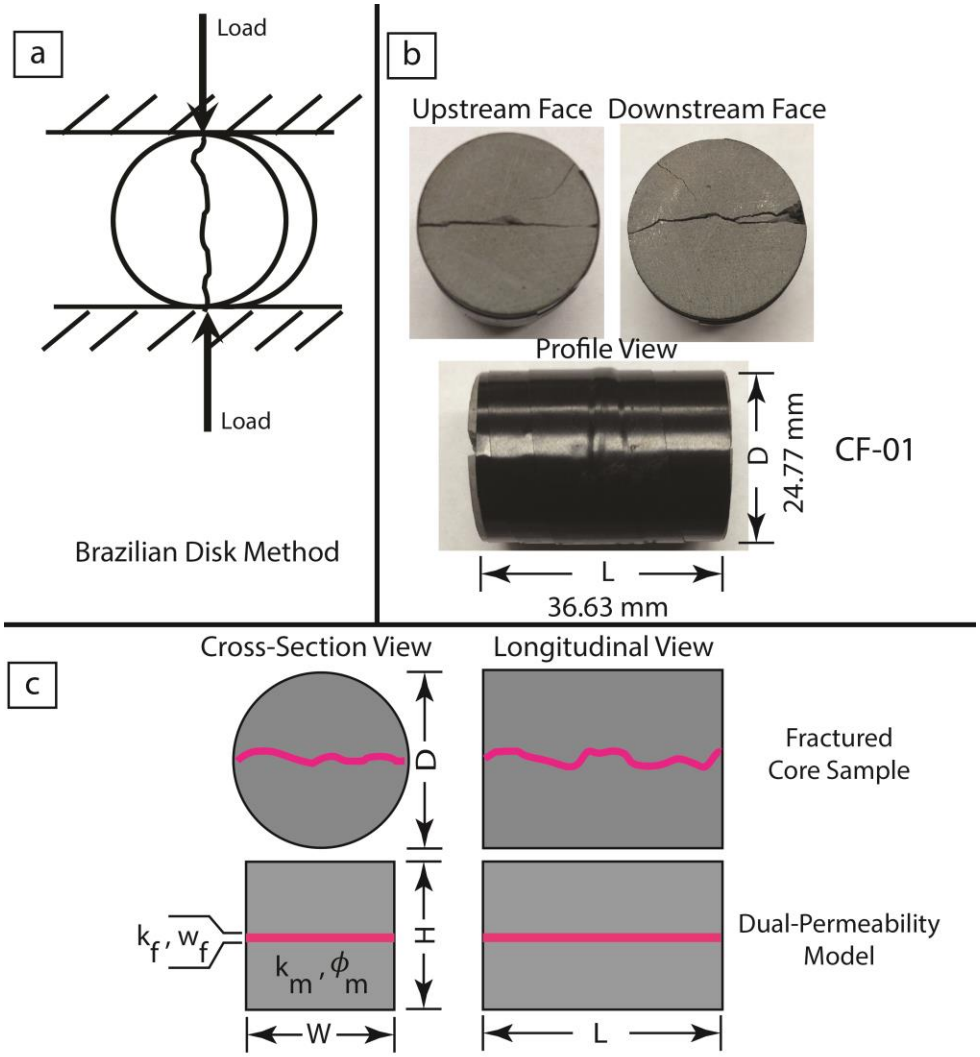

Figure 3.1 a. Schematic of Brazilian Disk method (Hondros 1959)). Cement sample is loaded diametrally until a tensile (Mode I) crack forms. Sample wrapped in heat-treat shrink wrap (to provide integrity) during fracture process. Figure adapted from (Cronin 2011). **b.** Fractured cement core sample CF-01 in cross-section and profile views. There is one dominant through-going fracture plane with a visibly smaller minor secondary plane at ~30 degrees. **c.** Dual-permeability model has a single planar fracture and equal cross-sectional area ($W = H = \sqrt{\pi/4}\,D \approx 0.866D$) to fractured core sample. w_f is fracture aperture, k_f is fracture permeability, k_m is matrix permeability, and ϕ_m is matrix permeability. Fracture porosity assumed to equal 1.

EXPERIMENTAL METHOD

Cement matrix porosity ($\emptyset_m = 14.3\ \% \pm 0.5\ p.u.$) was measured in CI-01 using a bench top helium porosimeter[1] and falls within the typical range for Class H Portland cement (10% to 50%) (Taylor 1997). Cement core plugs were enclosed in a 75-durometer Viton sleeve, which was mounted inside a hydrostatic pressure cell (Figure 3.2). The pore was fluid was Argon (molecular diameter = 0.38 nm) (Reid et al. 1987) and the confining fluid was vacuum pump oil. Valves allowed the apparatus to conduct steady-state ((API) 1998) and pulse-decay (Dicker et al. 1988) permeability measurements. Steady-state permeability (k) to gas is (Dandekar 2013) is:

$$k = -\frac{8Q_{out}P_{out}\mu L}{(P_{in}+P_{out})(P_{out}-P_{in})\pi D^2} \quad [3.1]$$

Where D is core diameter, L is core length, μ is average viscosity, and Q_{out} is the volumetric flow rate measured on the downstream side. P_{in} and P_{out} are the pressure at the upstream (inlet) and downstream (outlet) side. The $2\,Q_{out}P_{out}/(P_{in}+P_{out})$ term in [3.1] equals the average flow rate through the core sample since gas expands between P_{in} and P_{out}. The steady-state permeability of the intact core sample (CI-01) is ($3.4\ x10^{-17}m^2, 34\ \mu D$) (Figure 3.13).

[1] I present the repeatability of this porosity result in Table 3.4 of the Appendix.

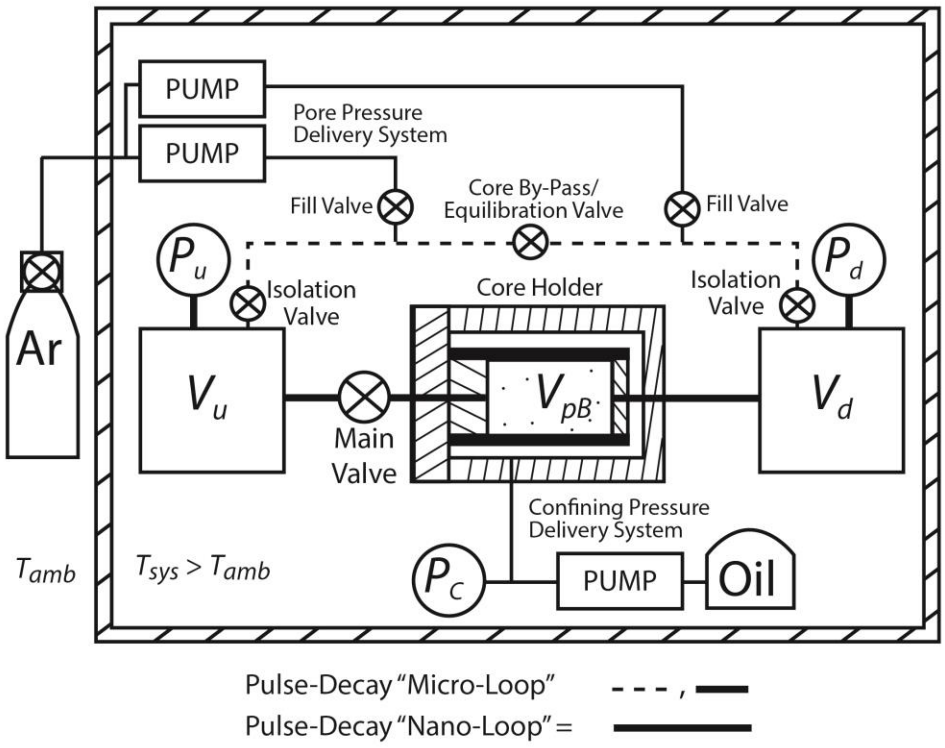

Figure 3.2 Permeability apparatus with independent upstream and downstream pore pressure pumps and confining pressure pumps. System temperature is held constant (T=30 +/- .01 C). Steady-state permeability experiments are conducted by closing the "core by-pass/equilibration valve." Pulse-decay permeability experiments are conducted by closing valves to create fixed-volume upstream and downstream reservoirs. The experiment starts when the main valve is opened. The smallest reservoir volume configuration ("nano-loop") is when the upstream and downstream isolation valves are closed. The largest reservoir volume configuration ("micro-loop") is when both isolation valves are open but both fill-valves and by-pass valves are closed.

Pulse-Decay Permeability

Pulse-decay permeability experiments were conducted at 9.01 MPa confining stress and 6.40 MPa average pore pressure following the methods of (Dicker et al. 1988). The upstream pulse pressure was less than 10% of the mean pore pressure. Effective horizontal permeability in the core (k_H) is proportional to the linear best-fit slope (m_E) to the $\ln\left|\frac{P_u - P_d}{P_u(0) - P_d(0)}\right|$ versus time (Dicker et al. 1988):

$$k_H = -\frac{\phi\overline{\mu C}_E L^2}{f(a,b)} m_E \quad [3.2]$$

m_E is measured after 90% decay ($\Delta P_D = 0.1$) in the original differential pressure which corresponds to $\ln|\Delta P_D|$ equal to -2.3. $\overline{\mu C}_E$ is the average viscosity-compressibility product. $f(a,b)$ is a function of sample pore volume and reservoir volume [3.3].

$$f(a,b) = (a + b + ab) - \frac{1}{3}(a + b + 0.4132ab)^2 + 0.0744(a + b + 0.0578ab)^3 \quad [3.3]$$

Where a is the ratio of core pore volume (V_{pB}) to upstream reservoir volume (V_u) [3.4] and b is the ratio of pore volume to downstream reservoir volume (V_d) [3.5]:

$$a = \frac{V_{pB}}{V_u} \quad [3.4]$$

$$b = \frac{V_{pB}}{V_d} \quad [3.5]$$

The dimensionless volume-averaged reservoir pressure (P_{LD}) is:

$$P_{LD} = \frac{\frac{P_u(t)V_u + P_d(t)V_d}{V_u + V_d} - P_0}{P_1 - P_0} \quad [3.6]$$

PULSE-DECAY RESULTS

In the intact sample (CI-01), the upstream and downstream reservoir pressures smoothly converged after approximately 60 seconds at the final equilibrium pressure (Figure 3.3). However, reservoir pressures converged after about 4 seconds for the fractured core sample (CF-01) (Figure 3.3). The effective horizontal permeability (Equation [3.2]) in CF-01 ($k_H = 3.1x10^{-16}m^2, 310\ \mu D$) is approximately 11 times

greater than the intact matrix results[2] for CI-01 ($k_H = 2.7x10^{-17}m^2, 27\ \mu D$). In addition, the volume-averaged dimensionless reservoir pressure (Equation [3.6]) shows a pronounced inflection point at about 0.7 seconds in the fractured sample, while the intact sample shows a smooth linear trajectory the entire time. The convergence pressure (P_{conv}) for CF-01 corresponds to the "corner-point" of maximum inflection in P_{LD} versus time. The "corner-point" is where early-time and late-time regressions to P_{LD} intersect on a semilog plot (Figure 3.4). The equilibrium pressure (P_{eqb}) corresponds to the final equilibrium pressure in the system (Figure 3.4). The different slopes for P_{LD} versus time confirm that flow behavior in CF-01 is different.

[2] Additional pulse-decay results conducted at different confining stresses and reservoir volumes for CI-01 are detailed in the Appendix (**Figure 3.14**).

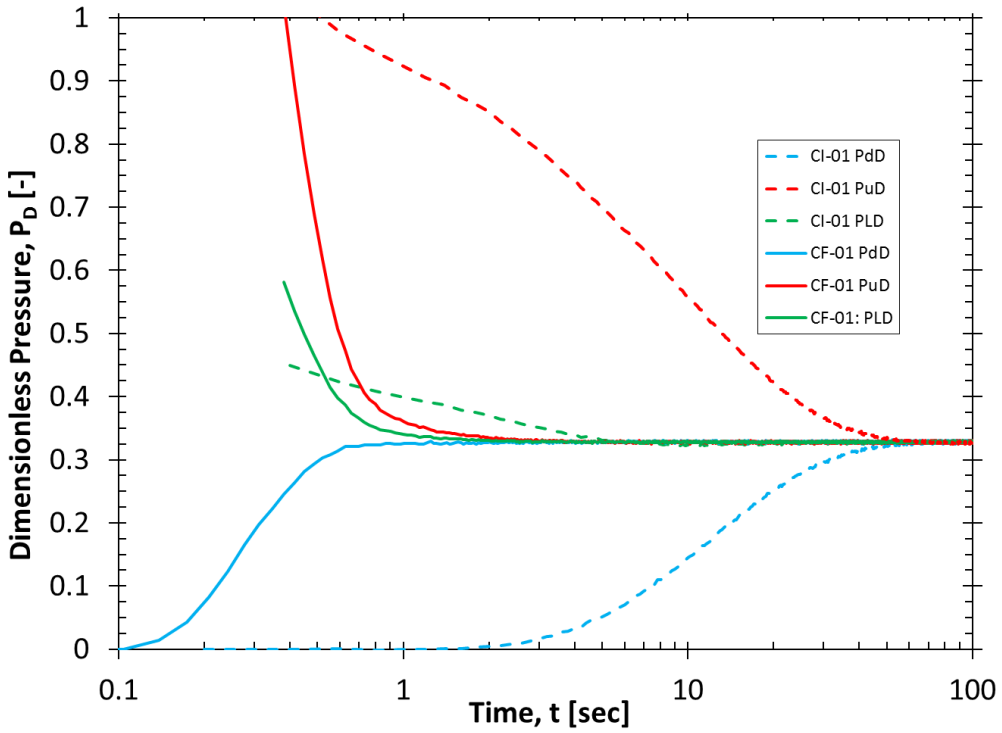

Figure 3.3 Pulse-decay dimensionless reservoir pressure versus time for intact core sample CI-01 (dashed) and fractured core sample CF-01 (solid) at $\bar{P}_C = 9.01\ MPa$ and $\bar{P}_p = 6.40$ MPa. P_{uD} is dimensionless upstream pressure, P_{dD} is dimensionless downstream pressure, and P_{LD} is the dimensionless volume-averaged reservoir pressure. $V_u = 3.150\ cc, V_d = 4.132\ cc$ (a $= 0.84, b = 0.64$). Pore fluid is Argon at 30 ^{o}C.

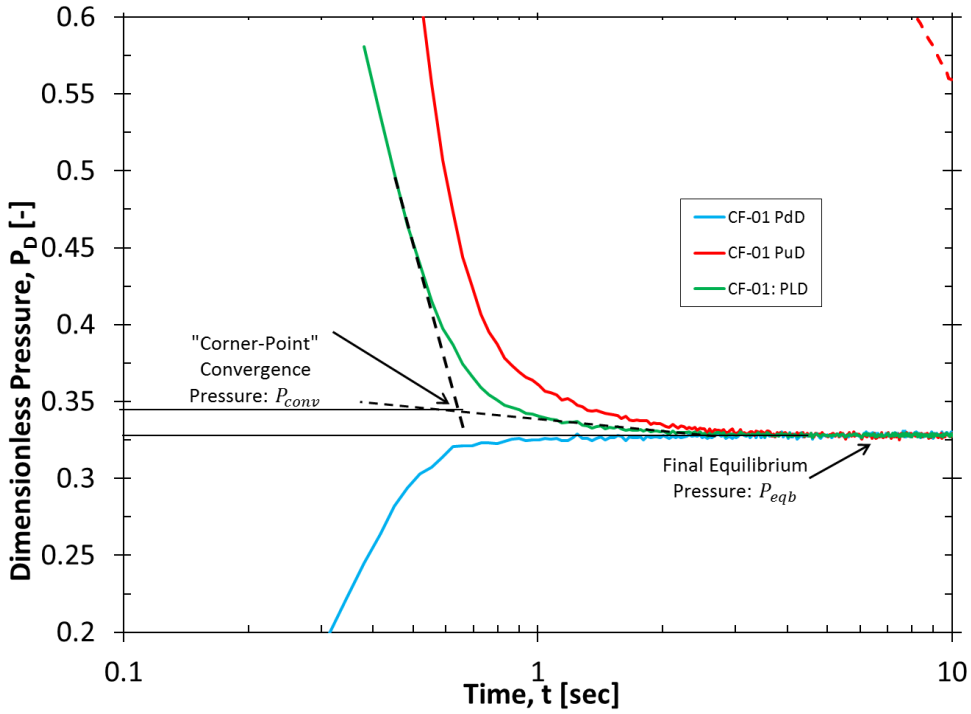

Figure 3.4 Expanded view of Figure 3.3 illustrating how the "corner-point" convergence pressure and equilibrium pressures are graphically identified.

DUAL-PERMEABILITY MODEL

Conceptual Model Description

My conceptual fractured dual-permeability model has two distinct porous domains: the pore volume in the matrix (V_{pm}) and the pore volume within the fractures (V_{pf}) (Figure 3.5). I refer to the matrix domain (Ω_1) as the "primary" porosity and the fractured domain (Ω_2) as the "secondary" porosity (Warren et al. 1963). Matrix has isotropic permeability (k_m) and constant intrinsic porosity (ϕ_m). This general fractured porous medium model has four subcases illustrated in Figure 3.6. The first case is un-fractured "pure matrix" (Figure 3.6a). The second case is the "ice cream sandwich" model with a single set of planar fractures ($N_\perp = 1$) aligned parallel to the horizontal flow direction (x-axis) (Figure 3.6b). The third case is the "plus-sign" model with two mutually orthogonal fracture sets (Figure 3.6c). The fourth case is the "sugar cube" model with three mutually orthogonal fracture sets (Figure 3.6d).

The primary (matrix) porosity bulk volume fraction (Φ_1) is:

$$\Phi_1 = \frac{V_{pm}}{V_B} \quad [3.7]$$

The secondary (fracture) bulk volume fraction (Φ_2) is:

$$\Phi_2 = \frac{V_{pf}}{V_B} \quad [3.8]$$

The relationship between Φ_1 and Φ_2 is:

$$\Phi_1 = \phi_m(1 - \Phi_2) \quad [3.9]$$

Equation [3.9] is derived from conservation of total pore volume. This is because $(1 - \Phi_2)$ equals the total volume fraction not belonging to the fractured domain. The ratio of secondary porosity to total porosity (ω_f) is:

$$\omega_f = \frac{\Phi_2}{\Phi_1 + \Phi_2} \quad [3.10]$$

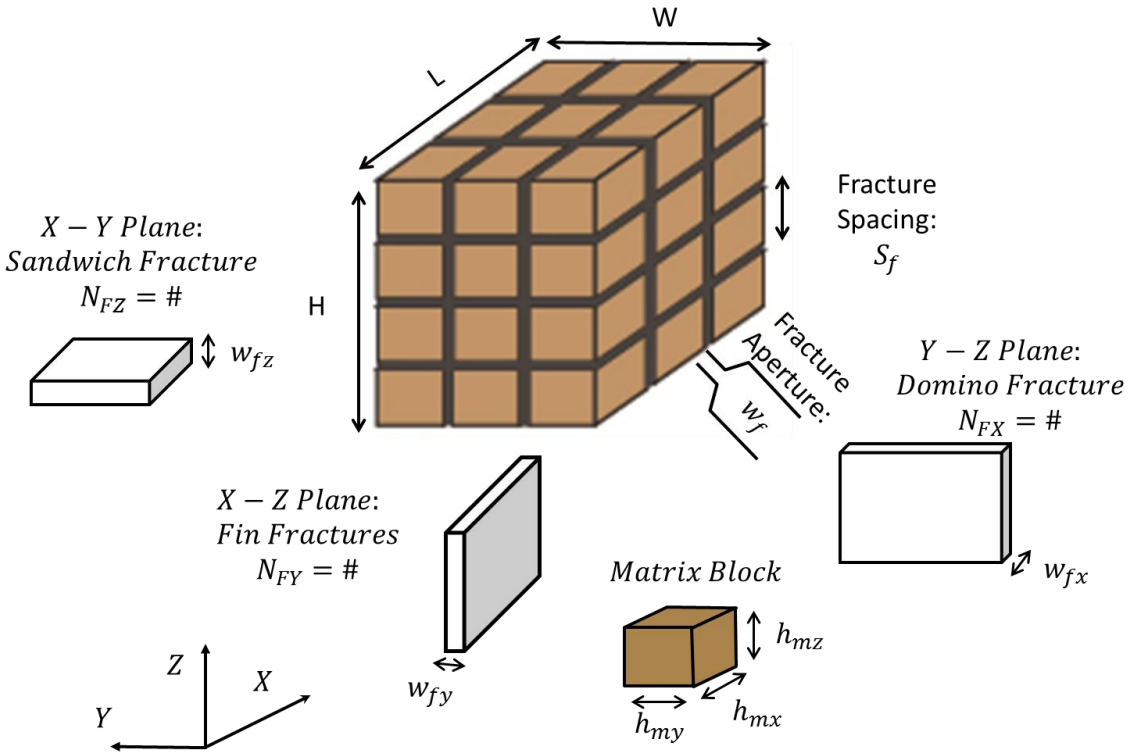

Figure 3.5 Schematic of fractured porous medium with width W, height H, and length L. Matrix blocks and fractures are aligned with the Cartesian coordinate system. The number of fractures is N_F, fracture width is w_f, and the spacing between two parallel fractures is S_f, where subscripts "x", "y", and "z" refer to the cartesian direction perpendicular to the fracture plane. In any direction, there are $(N_F + 1)$ matrix blocks.

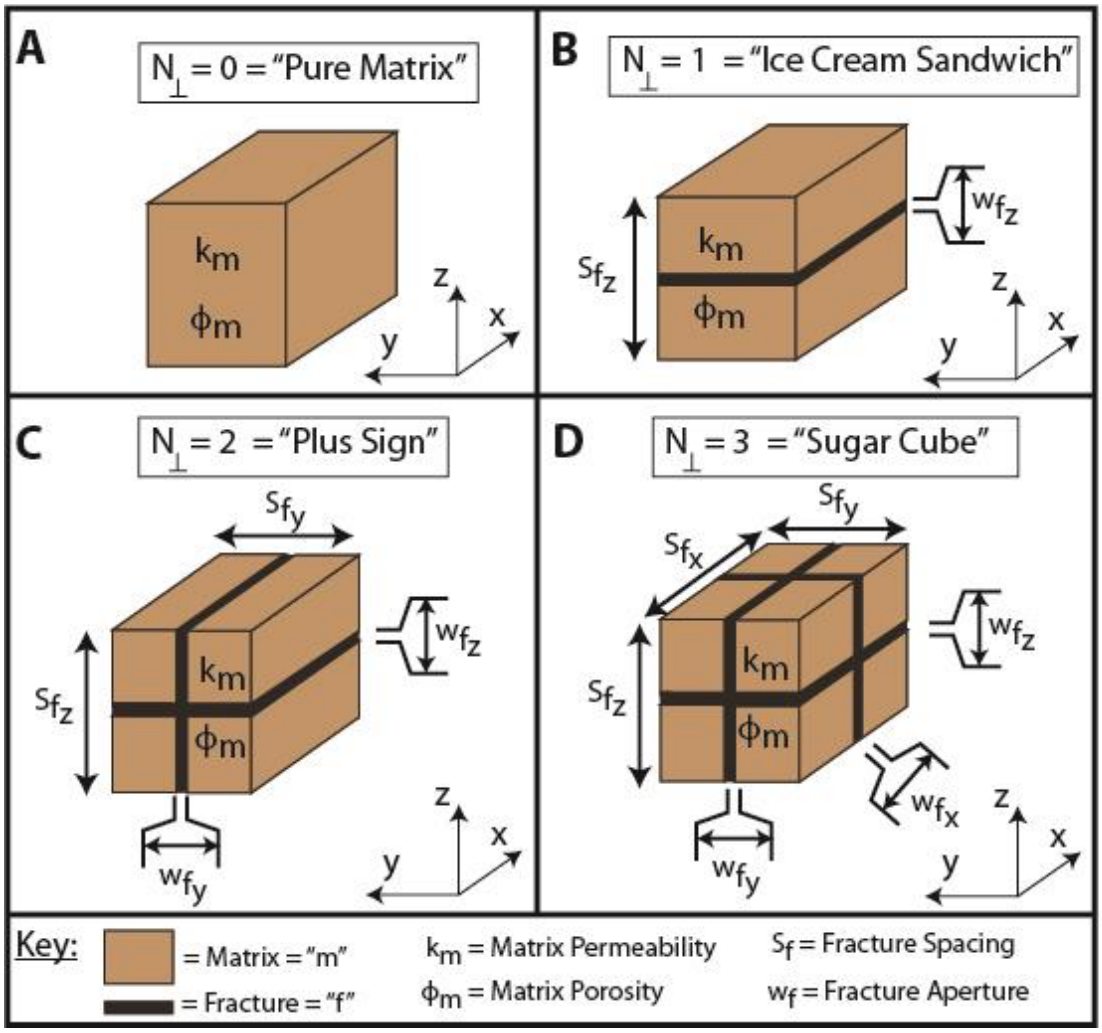

Figure 3.6 Unit volumes for four conceptual fracture geometries corresponding to the generic fractured medium depicted in **Figure 3.5**. $N_{\perp}$ is the number of mutually orthogonal fracture planes. Heavy black lines correspond to planar fractures. **A)** "Pure matrix" case ($N_{\perp} = 0$). **B**) "Ice cream sandwich" case with single planar fracture ($N_{\perp} = 1$) is adapted from Ning (1992). **C**) "Plus sign" case with two mutually orthogonal fracture planes ($N_{\perp} = 2$). **D**) "Sugar cube" case with three mutually orthogonal fracture planes ($N_{\perp} = 3$) is adapted from Warren and Root (1963).

For the general case of $N_\perp$ = 0, 1, 2, or 3 sets of fractures, Equations [3.8], [3.10], and [3.9] become:

$$\Phi_1 \approx \phi_m \left(1 - N_\perp \frac{\phi_f w_f}{S_f}\right) \quad [3.11]$$

$$\Phi_2 \approx N_\perp \frac{\phi_f w_f}{S_f} \quad [3.12]$$

$$\omega_f \approx \frac{N_\perp \phi_f w_f}{\phi_m S_f + N_\perp \phi_f w_f (1-\phi_m)} \quad [3.13]$$

Equations [3.11], [3.12], and [3.13] are valid approximations when S_f and w_f are isotropic and w_f^2/S_f^2 is small. Refer to Table 3.2 for exact values of these quantities.

Table 3.2 Summary of key variables in fractured core model for 1, 2, and 3 sets of orthogonal fracture planes ($N_\perp$). α is defined in terms of a finite difference approximation to Equation [3.27], where average matrix pressure is defined at the center of a matrix block (Kazemi et al. 1976) and matrix permeability is isotropic.

Variable	$N_\perp = 1$	$N_\perp = 2$	$N_\perp = 3$
Φ_2	$\phi_f \frac{w_{fz}}{S_{fz}}$	$\phi_f \frac{w_{fz}}{S_{fz}}\left(1 - \frac{w_{fy}}{S_{fy}} + \frac{w_{fy}S_{fz}}{w_{fz}S_{fy}}\right)$	$\phi_f \left[\frac{w_{fz}}{S_{fz}}\left(1 - \frac{w_{fy}}{S_{fy}} - \frac{w_{fx}}{S_{fx}} + \frac{w_{fx}w_{fy}}{S_{fx}S_{fy}}\right) + \frac{w_{fx}}{S_{fx}}\left(S_{fy} - w_{fy}\right) + \frac{w_{fy}}{S_{fy}}\right]$
A_f	$S_{fy}w_{fz}$	$S_{fy}w_{fz} + w_{fy}(S_{fz} - w_{fz})$	$S_{fy}w_{fz} + w_{fy}(S_{fz} - w_{fz})$
A_{meq}	$2S_{fy}S_{fx}$	$2S_{fx}[(S_{fy} - w_{fy}) + (S_{fz} - w_{fy})]$	$2\begin{bmatrix} S_{fx}(S_{fy} + S_{fz} - w_{fy} - w_{fz}) + S_{fy}(S_{fz} - w_{fx} - w_{fz}) + \\ S_{fz}(-w_{fx} - w_{fy}) + w_{fz}(w_{fx} + w_{fy}) \end{bmatrix}$
α	$4\left(\frac{N_{FX}}{(N_{FX}+1)(S_{fx} - w_{fx})}\right)^2$	$4\left[\left(\frac{N_{FX}}{(N_{FX}+1)(S_{fx} - w_{fx})}\right)^2 + \left(\frac{N_{FY}}{(N_{FY}+1)(S_{fy} - w_{fy})}\right)^2\right]$	$4\left[\left(\frac{N_{FX}}{(N_{FX}+1)(S_{fx} - w_{fx})}\right)^2 + \left(\frac{N_{FY}}{(N_{FY}+1)(S_{fy} - w_{fy})}\right)^2 + \left(\frac{N_{FZ}}{(N_{FZ}+1)(S_{fz} - w_{fz})}\right)^2\right]$
λ_f	$\frac{24k_mS_{fx}}{w_{fz}^3}$	$\frac{24k_mS_{fx}[(S_{fy} - w_{fy}) + (S_{fz} - w_{fz})]}{[S_{fy}w_{fz}^3 + (S_{fz} - w_{fz})w_{fy}^3]}$	$\frac{24k_mS_{fx}}{[S_{fy}w_{fz}^3 + (S_{fz} - w_{fz})w_{fy}^3]}\begin{bmatrix} S_{fx}(S_{fy} + S_{fz} - w_{fy} - w_{fz}) + \\ S_{fy}(S_{fz} - w_{fx} - w_{fz}) - \\ S_{fz}(w_{fx} + w_{fy}) + w_{fz}(w_{fx} + w_{fy}) \end{bmatrix}$

Dual-Permeability Model Description for CF-01

CF-01 has one dominant, through-going fracture (Figure 3.1b), and represents the dual-permeability model case with a single planar fracture ($N_{\perp} = 1, N_{FZ} = 1$) (Figure 3.1c). However, CF-01 also had a minor secondary fracture plane at ~30 degrees to the main plane (Figure 3.1b). Therefore I also present the results for the "plus sign" case ($N_{\perp} = 2, N_{FZ} = N_{FY} = 1$). S_{fz} equals model thickness H, S_{fy} equals model width W, and k_m and ϕ_m correspond to the measured values from CI-01. Therefore, the focus for this dual-permeability model is to vary the fracture aperture and number of orthogonal fracture planes to replicate the observed pulse-decay response (Figure 3.3).

Porosimetry

I determine the pore volume in the matrix and fractures as follows. First, I use Boyles Law to calculate the total pore volume (V_{pm} plus V_{pf}) in the sample:

$$V_{pB} = \frac{\left(\frac{P_{eqb}}{Z_{eqb}} - \frac{P_1}{Z_1}\right)V_u + \left(\frac{P_{eqb}}{Z_{eqb}} - \frac{P_0}{Z_0}\right)V_d}{\frac{P_0}{Z_0} - \frac{P_{eqb}}{Z_{eqb}}} \quad [3.14]$$

Pore volume in the fractures corresponds to the difference in pore volume of the fractured sample and the intact sample:

$$V_{pf} = V_{pB} - \phi_m V_B \quad [3.15]$$

Since apparatus reservoir volumes and matrix porosity are known, Equations [3.14] and [3.15] can be directly solved using Boyle's Law porosimety. This allows direct calculation of Φ_1 ([3.7]), Φ_2 ([3.8]), and ω_f ([3.10]). However, V_{pf} may be too small to accurately resolve. In such a case, Φ_1 will approximately equal the matrix porosity measured in CI-01 and Φ_2 must be calculated by assuming values for w_f and S_f (Table 3.2).

Early-Time Model

The permeability of a single fracture (k_f) is:

$$k_f = \frac{w_f^2}{12} \quad [3.16]$$

k_f is derived by equating flow through parallel plates to Darcy's law (Bird et al. 2007). The effective horizontal permeability of CF-01 is the area-weighted average of fracture permeability and matrix permeability.:

$$k_{fH} = k_f \frac{A_f}{A_H} + k_m \frac{1-A_f}{A_H} \quad [3.17]$$

Equation [3.17] is the permeability required in an un-fractured homogeneous rock to equal steady-state flow through the fractured sample. A_f is the cross-sectional area of the fractures (Table 3.2). A_H is the bulk cross-sectional area and equals WH. Pulse-decay permeability values for heterogeneous samples approximate steady-state values as reservoir volumes increase (Kamath et al. 1992). I approximate k_{fH} by determining the best-fit linear slope ($m_E = -0.495\, s^{-1}$) to the plot of $\ln\left|\frac{P_u(t)-P_d(t)}{P_u(0)-P_d(0)}\right|$ versus time ($k_{fH} = k_H = 3.1x10^{-16}m^2$) (Figure 3.3) with Equation [3.2]. Equations [3.16] and [3.17] are combined to solve for fracture aperture for the single-fracture case:

$$w_f^3 - 12k_m w_f = 12(k_{fH} - k_m)H \quad [3.18]$$

Since equation [3.18] is a cubic polynomial, there may be up to three real roots (2006). However, the correct value of w_f must satisfy the following conditions:

Condition 1: The root is positive and real

Condition 2: If 2 or more roots are positive and real, aperture is w_f is smallest root greater than zero.

In a similar way, fracture aperture for the two orthogonal fracture planes case is:

$$12(H^2 k_{fH} - k_m) = -w_f^4 + 2Hw_f^3 + 12k_m w_f^2 - 24k_m H w_f \quad [3.19]$$

Since Equation [3.19] is quartic, valid roots (values of w_f) must satisfy the two conditions I defined earlier for equation [3.18]. Refer to Appendix A for details on the early-time approximate solution.

Late-Time Model

At late-time, reservoir pressures have equilibrated through the fracture. Late-time pressure is the volume-averaged reservoir pressure (restated from [3.6] in dimensional form):

$$\bar{P}_L(t) = \frac{P_u(t)V_u + P_d(t)V_d}{V_u + V_d} \quad [3.20]$$

The late-time volume is the sum of the reservoir volumes and the fracture pore volume:

$$V_L = V_u + V_d + V_{pf} \quad [3.21]$$

The $\ln\left|\frac{\bar{P}_L(t)-P_{eqb}}{P_{conv}-P_{eqb}}\right|$ is:

$$\ln\left|\frac{\bar{P}_L(t)-P_{eqb}}{P_{conv}-P_{eqb}}\right| = -\frac{k_m\alpha}{\Phi_1(\overline{\mu C})_L}\left(\frac{V_L+V_{pm}}{V_L}\right)t \quad [3.22]$$

Equation [3.22] assumes that pressure equilibration with the cement matrix is an exponential process where the matrix domain (Ω_1) is at pseudo-steady-state. $(\overline{\mu C})_L$ is the average viscosity-compressibility product evaluated at P_{eqb}. P_{conv} and P_{eqb} were graphically calculated in Figure 3.4. Matrix permeability is calculated by determining the best-fit linear slope (m_L) to a plot of $\ln\left|\frac{\bar{P}_L(t)-P_{eqb}}{P_{conv}-P_{eqb}}\right|$ versus time:

$$k_m = -\frac{\Phi_1(\overline{\mu C})_L}{\alpha}\left(\frac{V_L}{V_L+V_{pm}}\right)m_L \quad [3.23]$$

Shape factor (α) equals the equivalent surface area of matrix in contact with the fractures (A_{meq}) divided by a characteristic matrix block half-length (L_{meq}) per unit of bulk volume:

$$\alpha = \frac{A_{meq}}{L_{meq}V_B} \quad [3.24]$$

The value of α depends on the fracture spacing and the number of fracture planes (Table 3.2) and a detailed derivation of α is provided in Chapter 4.A4. Additional information on shape factors can be found in Warren and Root (1963), Kazemi et al. (1976) or Lim and Aziz (1995). Refer to Appendix B for details on the late-time approximate solution.

Numerical Model

The coupled gas flow equations for the fractured core system (**Figure 3.6**) expressed in 1-Dimension are:

In the fractured (Ω_2) domain:

$$k_f \frac{A_f}{A_H} \frac{\partial^2 P_f}{\partial x^2} - q_{m-f} = \Phi_2 \overline{\mu C}_f \frac{\partial P_f}{\partial t} \quad [3.25]$$

In the matrix (Ω_1) domain:

$$k_m \frac{(1-A_f)}{A_H} \frac{\partial^2 \bar{P}_m}{\partial x^2} + q_{m-f} = \Phi_1 \overline{\mu C}_m \frac{\partial \bar{P}_m}{\partial t} \quad [3.26]$$

Where:

$$q_{m-f} = \frac{\alpha\, k_m}{\overline{\mu_g C_g}_{m-f}} \left(P_f - \bar{P}_m\right) \quad [3.27]$$

Equations [3.25], [3.26], and [3.27] are based on the original by Warren and Root (1963), where P_f is fracture pore pressure, $\bar{P}_m$ is average matrix pore pressure, q_{m-f} is the inter-porosity flux between the matrix and fractures, and $\overline{\mu_g C_g}$ is the average viscosity-compressibility product. I assume that pore pressure varies only as a function of x in the fracture (Ω_2) domain and (when matrix blocks are continuous) in the matrix (Ω_1) domain. I assume that permeability is isotropic, fracture aperture and porosity are constant, and that gas flow is single-phase, isothermal, and described by Darcy's Law. I used the numerical methods described by Ertekin et al. (2001) to solve Equations [3.25], [3.26],

and [3.27] for the pulse-decay boundary/initial conditions using an implicit finite-difference scheme. Refer to **Appendix 4.A4** for details on the numerical simulator.

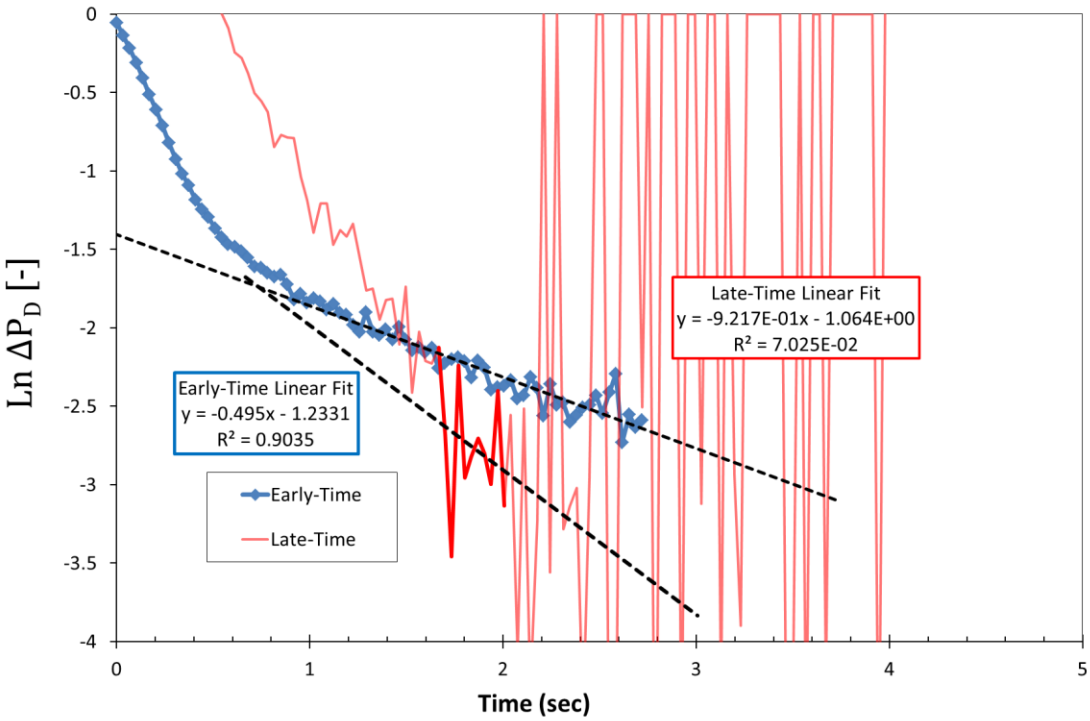

Figure 3.7 Determining the early-time (m_E) versus late-time (m_L) linear regression dissipation slopes to the CF-01 pulse-decay pressure versus time data shown in **Figure 3.3**. The early-time slope is fitting $\ln\left|\frac{P_u(t)-P_d(t)}{P_1-P_0}\right|$ versus time data (blue). The late-time slope is fitting $\ln\left|\frac{P_L(t)-P_{eqb}}{P_{conv}-P_{eqb}}\right|$ versus time data (red). The dark red portion of the late-time data was used for the regression.

MODEL RESULTS AND DISCUSSION

Matrix permeability and porosity is known, but the fracture aperture is not known. The core sample has a dominant horizontal fracture plane, but there is a small secondary fracture (**Figure 3.1**). For a single fracture plane ($N_{\perp} = 1$), the interpreted fracture aperture is between $(49 - 56)\ \mu m$ from numerical simulation (**Figure 3.8**) and 20 μm from the early-time analytical model (Equation [3.18]). For two orthogonal fracture planes ($N_{\perp} = 2$), the interpreted fracture aperture from numerical simulation is between $(20 - 30)\ \mu m$ (**Figure 3.9**). However, the analytical model (Equation [3.20]) does not give real results for the $N_{\perp} = 2$ case because the left-hand side of Equation [3.20] is always negative. I check the late-time analytical model by comparing the matrix permeability measured in CI-01 ($k_m = 2.7x10^{-17}m^2$) to the permeability I back-interpret using Equation [3.23]. I measured the late-time pressure decline slope ($m_L = -9.2x10^{-1}\ s^{-1}$, **Figure 3.7**), and calculate that $k_m = 4.6x10^{-17}m^2, 46\ \mu D$ for the $N_{\perp} = 1$ case, and that $k_m = 2.3\ x10^{-17}m^2, 23\ \mu D$ for the $N_{\perp} = 2$ case. These late-time model values are reasonable and fall within a factor of 2 compared to the experimental result.

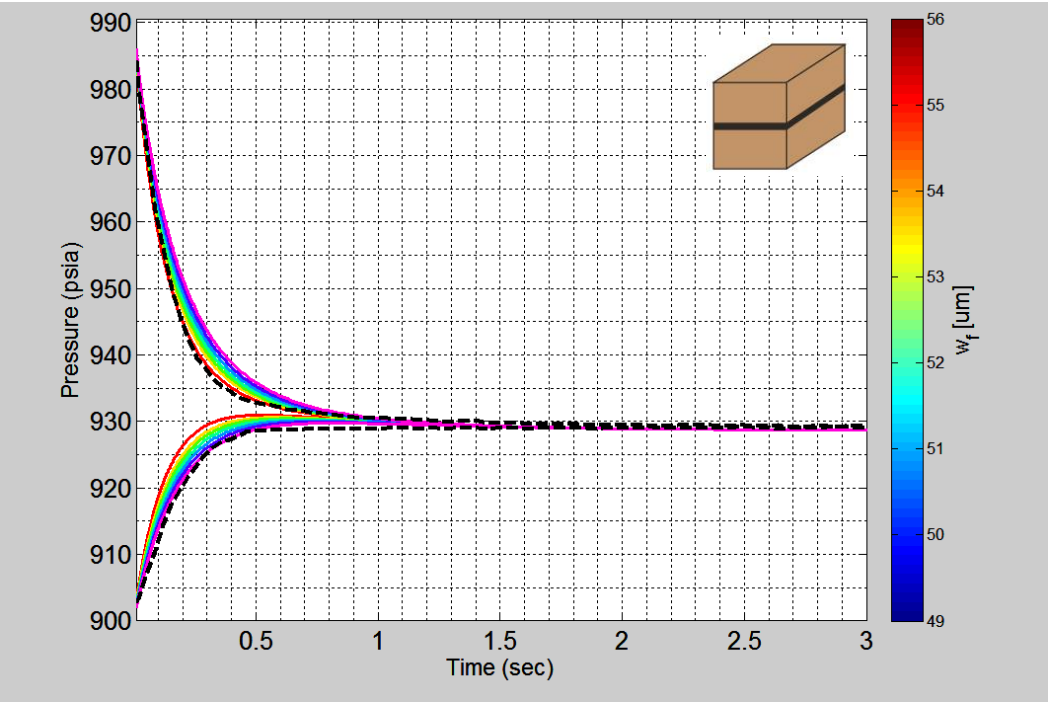

Figure 3.8 Experimental versus simulated pulse-decay data for CF-01 for the single-orthogonal fracture planes case. Fracture aperture is between 49 to 56 microns.

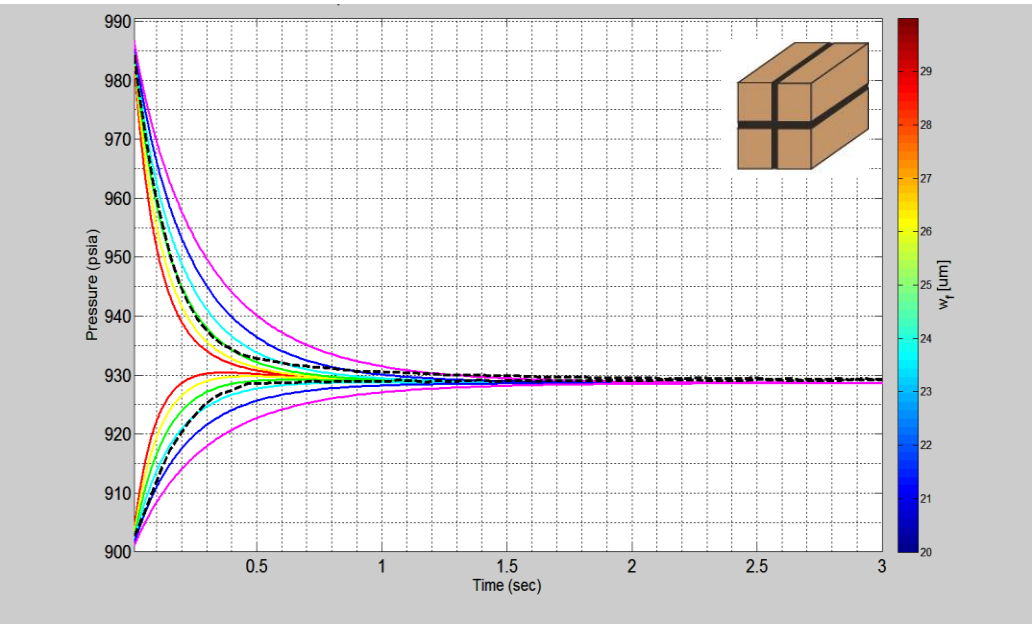

Figure 3.9 Experimental versus simulated pulse-decay data for CF-01 for the two-orthogonal fracture planes case. Fracture aperture is between 20 to 30 microns.

General Behavior of Fractured Porous Media for Different Fracture Geometries

The numerical simulation produced a high-quality fit to the experimental pulse-decay reservoir pressure time-series data for CF-01. However, CF-01 did not display a classical "dual-timescale" response (**Figure 1.4**) where reservoir pressures initially converge and then declined to a secondary equilibrium pressure. I show that this "dual-timescale" response is only observed when pressure equilibration through the fractures is rapid compared to pressure equilibration with the matrix. For the case of a single horizontal fracture with fixed aperture, larger values of matrix permeability and lower matrix porosity values lead to decreased dual-timescale behavior (**Figure 3.10**). This is also true for the "sugar cube" case (**Figure 3.12**). In addition, dual-timescale behavior decreases as fracture aperture decreases (**Figure 3.11**).

The ratio of fracture to matrix transmissibility (λ_f):

$$\lambda_f = \frac{k_m A_{meq}}{k_f A_f} \qquad [3.28]$$

Equation [3.28] compares the relative value of inter-porosity flow (between Ω_1 and Ω_2) versus flow through the fractured domain. λ_f depends on the fracture spacing and the number of fracture planes, which I define in **Table 3.2**. The early-time fracture convergence timescale "t_{conv_f}" is the time needed for 90% dissipation in the original differential pressure ($\Delta P_D = 0.1$):

$$t_{conv_f} = -\ln|0.1| \frac{\Phi_2 \overline{\mu C}_E L^2}{k_{fH}\, f(a_E, b_E)} \qquad [3.29]$$

The late-time matrix equilibrium timescale "t_{eqb_m}" is the time needed for 90% dissipation in the late-time differential pulse pressure ($\Delta P_{LD} = 0.1$):

$$t_{eqb_m} = -\ln|0.1| \frac{\Phi_1 (\overline{\mu C})_L}{k_m \alpha} \left(\frac{V_L}{V_L + V_{pm}} \right) \qquad [3.30]$$

Combining Equations [3.29] and [3.30] gives the characteristic matrix to fracture time-scale ratio:

$$\tau_f = \frac{k_{fH}}{k_m \alpha L^2}\left(\frac{\Phi_1 V_L\, f(a_E, b_E)}{\Phi_2 [V_L + V_{pm}]}\right)\frac{\overline{\mu C}_L}{\overline{\mu C}_E} \qquad [3.31]$$

Equation [3.31] compares the matrix equilibration timescale and the early-time fracture convergence timescale. Values of τ_f less than 1 indicate rapid pressure equilibration with the matrix while τ_f less than 1 indicates slow equilibration with the matrix compared to the initial convergence in reservoir pressure through the fractures. As the permeability contrast decreases and the fracture spacing gets closer, it becomes more difficult to maintain a differential pressure inside the core sample between the fractures (P_f) and the matrix (P_m). The increased mass flow-rate into the matrix results in a more uniform pressure profile in the core sample through time. The implication is that the pulse-decay behavior observed in a fractured sample will increasingly resemble that of a homogeneous sample as τ_f decreases.

CONCLUSIONS

The numerical dual-permeability model successfully replicated the pulse-decay response in a well-characterized fractured cement core sample, while the late-time analytical model was able to correctly-back interpret the measured matrix permeability. I show that additional fracture planes can produce a dual-timescale response. However, the presence of additional fracture planes decreases the characteristic length scale in the matrix resulting in more rapid pressure equilibration. I incorporate the competing effects of increased fracture permeability but more rapid matrix equilibration in the characteristic timescale ratio.

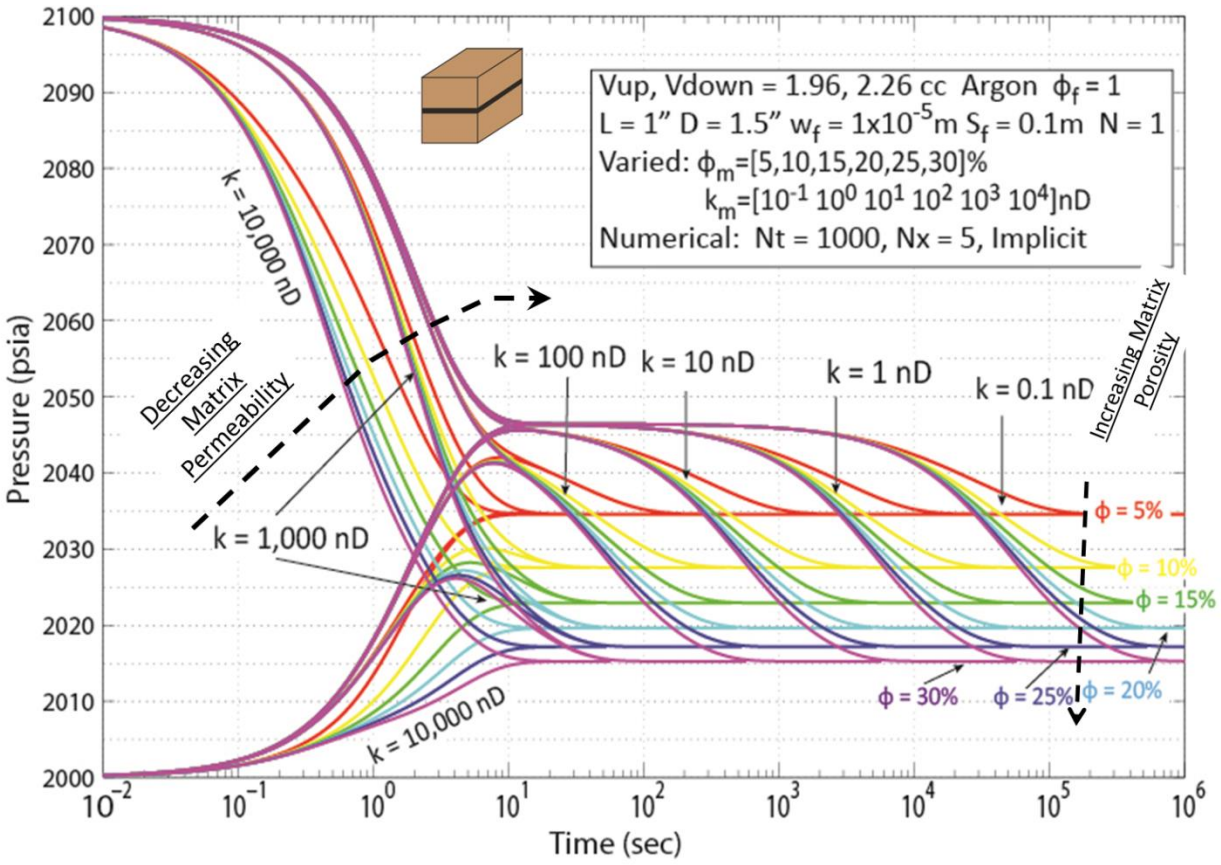

Figure 3.10 Theoretical pulse-decay pressure versus time behavior for example combinations of matrix permeability and porosity for a pulse-decay experiment in the UT Geomechanics laboratory on a core with 1 fracture plane. Pressure versus time data generated using Cronin numerical simulator.

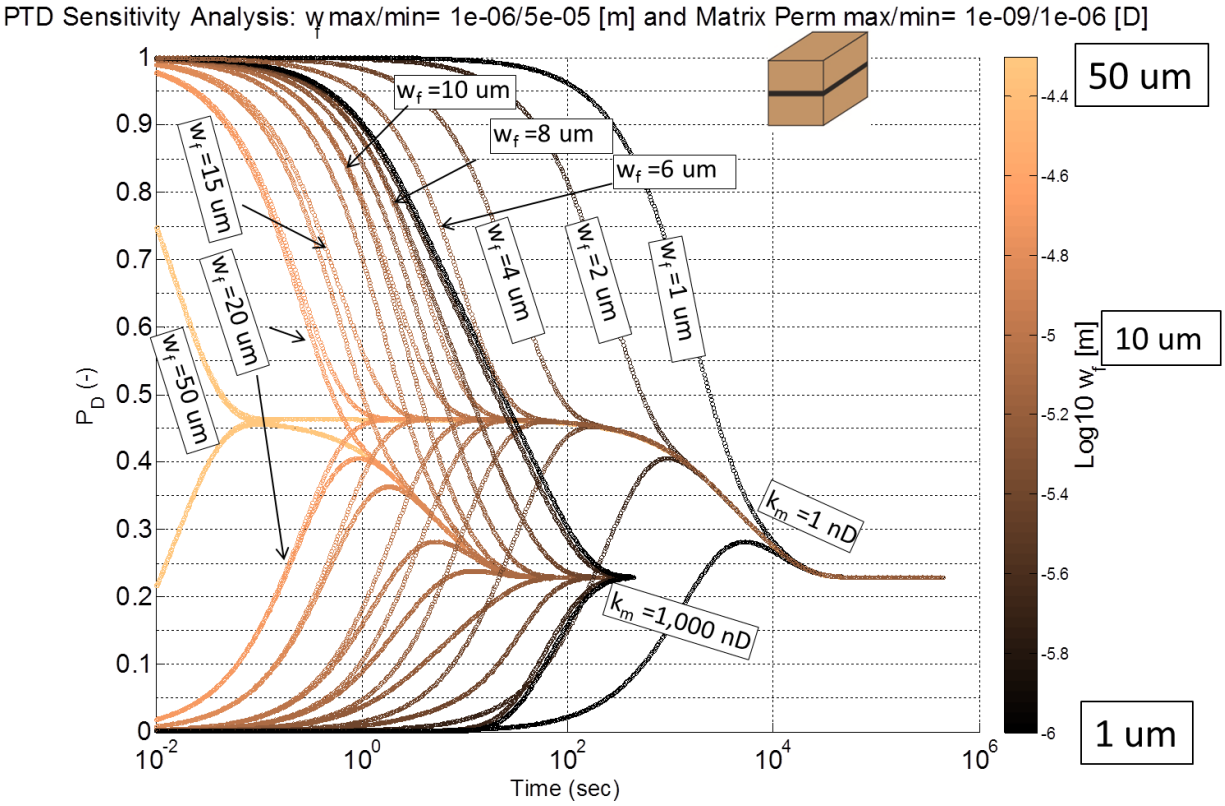

Figure 3.11 Theoretical pulse-decay pressure versus time behavior for example combinations of matrix permeability and fracture aperture for a pulse-decay experiment in the UT Geomechanics laboratory on a core with 1 fracture plane. Parameters listed in **Table 3.3**. Pressure versus time data generated using Cronin numerical simulator.

Table 3.3 Values used to generate pulse-decay data in **Figure 3.11**

V_u, V_d	1.96 cm^3, 2.26 cm^3	$L = 2.54\ cm\ (1\ in)$	$D = 3.91\ cm\ (1.5\ in)$
Pore Fluid	Argon	$\phi_m = 15\ p.u.$	
ΔP	689.5 kPa (100 psi)	$k_m = [10^{-21}, 10^{-18}]m^2$	
P_{u0}	14.47 MPa (2100 psi)	$w_f = [1,2,4,6,8,10,15,20,50]x10^{-6}m$	

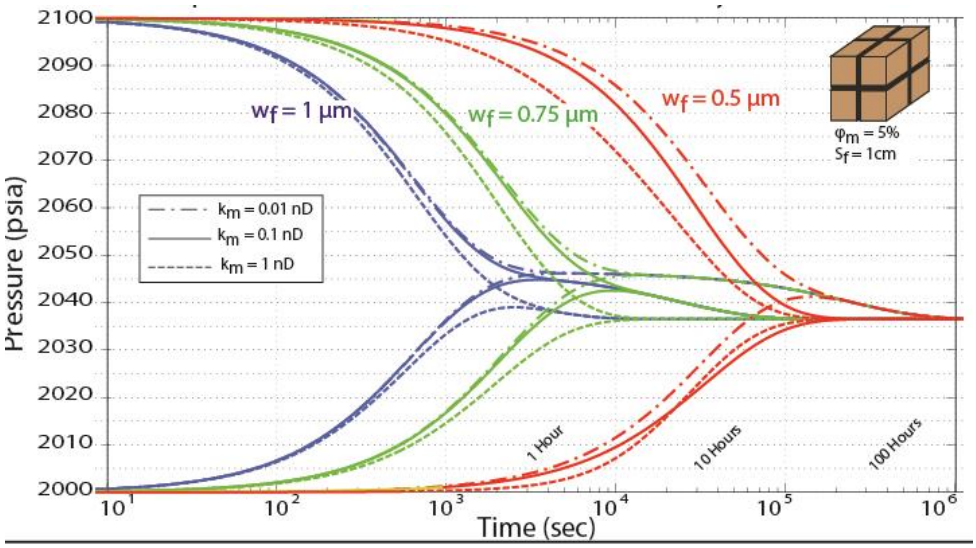

Figure 3.12 Theoretical pulse-decay pressure versus time behavior for example combinations of matrix permeability and fracture aperture for a pulse-decay experiment in the UT Geomechanics laboratory on a core with 3 mutually-orthogonal fracture planes ("sugar cube model). Dashed line corresponds to $k_m = 1.0\ nD$, solid lines to $k_m = 0.1\ nD$, and dash-dot lines to $k_m = 0.01\ nD$. Colors correspond to fracture aperture. Matrix porosity is 5%. Pressure versus time data generated using Cronin numerical dual-permeability model.

APPENDIX 3A: EARLY-TIME APPROXIMATE SOLUTION

The permeability of a single fracture (k_f) is:

$$k_f = \frac{w_f^2}{12} \quad [3.32]$$

I defined k_f by equating flow through parallel plates to Darcy's law (Bird et al. 2007). When fluid transport in the matrix is ignored (or the matrix permeability is taken to be zero), I can express fluid flow in this fractured rock in terms of the effective horizontal permeability (k_{fH}). k_{fH} is the permeability required in an un-fractured homogeneous rock (**Figure 3.6a**) to equal steady-state flow through a fractured rock.

$$k_{fH} = \frac{k_f A_f}{A_H} \quad [3.33]$$

A_f is the cross-sectional area of the fractures and A_H is the cross-sectional area of matrix plus fractures in the horizontal flow direction. For one fracture set ($N_\perp$ = 1):

$$k_{fH} = \frac{w_f^3}{12 S_f} \quad [3.34]$$

For two or more fracture sets ($N_\perp$ = 2 or 3):

$$k_{fH} = \frac{w_f^3 [2S_f - w_f]}{12 S_f^2} \approx \frac{w_f^3}{6 S_f} \quad [3.35]$$

Equations [3.34] and [3.35] assume zero matrix contribution ($k_m = 0$) and $w_f \ll S_f$. I defined k_{fH} to compare pulse-decay behavior in fractured cores and equivalent homogeneous cores, which may be markedly different (Ning 1992; Kamath et al. 1992).

Initial Conditions:

At initial conditions, the upstream reservoir is at the pulse pressure P_1 while the rest of the core sample (matrix and fractures) and the downstream reservoir are at the base pressure P_0.

$$\mathrm{P_u}(0) = P_{u0} \quad [3.36]$$

$$\mathrm{P_d}(0) = P_0 \quad [3.37]$$

$$\mathrm{P_m}(x,0) = P_0, \quad 0 < x < L \quad [3.38]$$

$$\mathrm{P_f}(x,0) = P_0, \quad 0 < x < L \quad [3.39]$$

Boundary Conditions:

The boundary conditions state that the fractures are hydraulically connected to the upstream and downstream reservoirs and that mass is conserved. Fluid flow into the core sample causes a drop in upstream pressure while fluid exiting the core causes downstream pressure to increase. At the convergence time, I assume that the upstream reservoir, fractures, and downstream reservoir are in pore pressure equilibrium. In addition, I assume that there is no flow at early-time into the lower-permeability matrix material prior to convergence, so matrix pressure $\mathrm{P_m}$ remains at $\mathrm{P_0}$. Therefore, the q_{m-f} term in [3.27] equals zero and flow in the fractures is defined by the pressure diffusion equation. Spatial pressure variation is only in the direction of flow.

$$\mathrm{P_u}(t) = P_f(x = 0, t), \quad t > 0 \quad [3.40]$$

$$\mathrm{P_d}(t) = P_f(x = L, t), \quad t \geq 0 \quad [3.41]$$

$$\frac{\mathrm{dP_u}(t)}{\mathrm{dt}} = \frac{k_{fH}}{\Phi_2 \overline{\mu C}_E L} \frac{V_{pf}}{V_u} \frac{dP_f}{dx}, \quad x = 0, t > 0 \quad [3.42]$$

$$\frac{\mathrm{dP_d}(t)}{\mathrm{dt}} = -\frac{k_{fH}}{\Phi_2 \overline{\mu C}_E L} \frac{V_{pf}}{V_d} \frac{dP_1}{dx}, \quad x = L, t > 0 \quad [3.43]$$

$$\mathrm{P_u(t) = P_f(x,t) = P_d(t) = P_{eqb}}, \quad 0 < x < L, t = t_{conv} \quad [3.44]$$

$$\mathrm{P_m(x,t) = P_0}, \quad 0 < x < L, \quad t < t_{conv} \quad [3.45]$$

$$\frac{\partial^2 P_f}{\partial x^2} = \frac{\Phi_2 \overline{\mu C}_E}{k_f} \frac{\partial P_f}{\partial t}, \qquad 0 < x < L, t < t_{conv} \quad [3.46]$$

Solution:

Conceptually, the initial conditions and boundary conditions in the early-time fractured core model are identical to the early-time layered core model I presented earlier. The layered core model solutions were based on minor modifications to Dicker and Smits (1988) who used the Laplace Transform to solve for reservoir pressure versus time in homogeneous core samples. Therefore, the only modification I must make to the layered-core solutions is to define dimensionless fracture time (t_{fD}):

$$t_{fD} = \frac{k_{fH}}{\Phi_2 \overline{\mu C}_E L^2} t \quad [3.47]$$

Upstream pressure:

$$\frac{P_u(t_{fD}) - P_0}{P_1 - P_0} = \frac{b_E}{a_E + b_E + a_E b_E} + 2\sum_{m=1}^{\infty} \frac{\exp(-t_{fD}\theta_m^2)(a_E b_E^2 + a_E \theta_m^2)}{[(\theta_m^4 + \theta_m^2(a_E + a_E^2 + b_E + b_E^2) + a_E b_E(a_E + b_E + a_E b_E)]cos\theta_m} \quad [3.48]$$

Downstream pressure:

$$\frac{P_d(t_{fD}) - P_0}{P_1 - P_0} = \frac{b_E}{a_E + b_E + a_E b_E} + 2\sum_{m=1}^{\infty} \frac{\exp(-t_{fD}\theta_m^2)(a_E b_E^2 - b_E \theta_m^2)}{[(\theta_m^4 + \theta_m^2(a_E + a_E^2 + b_E + b_E^2) + a_E b_E(a_E + b_E + a_E b_E)]cos\theta_m} \quad [3.49]$$

Differential pressure:

$$\frac{P_u(t_{fD}) - P_d(t_{fD})}{P_1 - P_0} = 2\sum_{m=1}^{\infty} \frac{\exp(-t_{fD}\theta_m^2) a_e(b_E^2 + \theta_m^2) - (-1)^m b_E[(a_E^2 + \theta_m^2)(b_E^2 + \theta_m^2)]^{0.5}}{[(\theta_m^4 + \theta_m^2(a_E + a_E^2 + b_E + b_E^2) + a_E b_E(a_E + b_E + a_E b_E)]} \quad [3.50]$$

a_E and b_E are dimensionless early-time pore volume to reservoir volume ratios:

$$a_E = V_{p1}/V_u \quad [3.51]$$

$$b_E = V_{p1}/V_d \quad [3.52]$$

and θ_m are the roots to the following equation:

$$tan\theta = \frac{(a_E + b_E)\theta}{(\theta^2 - a_E b_E)} \quad [3.53]$$

The first summation term ($m = 1$) term in Equation [3.50] dominates at large values of t_{fD}. Therefore, the time-domain solution for $\ln|\frac{P_u(t)-P_d(t)}{P_1-P_0}|$ is approximately:

$$\ln|\frac{P_u(t) - P_d(t)}{P_{u0} - P_0}| = -\frac{k_{fH}\theta_1^2}{\Phi_2 \overline{\mu C}_E L^2} t \quad [3.54]$$

In practice, Equation [3.54] is solved by determining the best-fit linear slope (m_E) to a plot of $\ln|\frac{P_u(t)-P_d(t)}{P_{u0}-P_0}|$ versus time. The effective fracture permeability is:

$$k_{fH} = -\frac{\Phi_2 \overline{\mu C}_E L^2}{f(a_E, b_E)} m_E \quad [3.55]$$

$f(a_E, b_E)$ (Dicker et al. 1988) approximates the value of θ_1^2 and is given by:

$$f(a_E, b_E) = (a_E + b_E + a_E b_E) - \frac{1}{3}(a_E + b_E + 0.4132 a_E b_E)^2 + 0.0744(a_E + b_E + 0.0578 a_E b_E)^3 \quad [3.56]$$

APPENDIX 3B: LATE-TIME APPROXIMATE SOLUTION

Initial Conditions:

Late-time describes period after initial convergence at t_{conv}. At t_{conv}, the reservoirs and fractures have equilibrated at P_{conv} while the low-permeability matrix remains at the base pressure P_0.

$$\mathrm{P_u}(t) = P_{conv} \ , t = t_{conv} \quad [3.57]$$

$$\mathrm{P_d}(t) = P_{conv} \ , t = t_{conv} \quad [3.58]$$

$$\mathrm{P_f}(x,t) = P_{conv} \ , 0 < x < L, t = t_{conv} \quad [3.59]$$

$$\mathrm{P_m}(x,t) = P_0 \ , 0 < x < L, t = t_{conv} \quad [3.60]$$

Boundary Conditions:

I assume that the reservoirs and fractures remain in perfect pressure equilibrium at late-time as reservoir pressure declines from P_{conv} to P_{eqb}. I combine the reservoirs and fracture pore volume into a single late-time volume (V_L) with a single average pressure (P_L):

$$\mathrm{P_L}(t) = \mathrm{P_u}(t) = P_f(x,t) = \mathrm{P_d}(t), \quad 0 < x < L, \ t \geq t_{conv} \quad [3.61]$$

Matrix pressure is equal to the average matrix pressure for all times:

$$P_m(x,t) = \overline{\mathrm{P}}_\mathrm{m}(t), \quad 0 < x < L, \ t \geq t_{conv} \quad [3.62]$$

These equations state there is no spatial variation in average matrix pressure or late-time system pressure. At late-time, reservoir pressure declines from P_{conv} to P_{eqb} (Equation [3.63]) while average pressure in the matrix (P_m) increases from P_0 to P_{eqb} (Equation [3.64]).

$$\mathrm{P_L}(t) = P_{eqb}, t = \infty \quad [3.63]$$

$$\overline{\mathrm{P}}_\mathrm{m}(t) = P_{eqb}, t = \infty \quad [3.64]$$

The mass-transfer rate between the late-time system and the fractures depends on the average pressure differential and the shape-factor α:

$$\frac{k_m \alpha}{\overline{\mu_g C_g}_{mf}} (\bar{P}_L - \bar{P}_m) = \Phi_1 \frac{\partial P_m}{\partial t} \quad [3.65]$$

This equation assumes a pseudo-steady-state (PSS) pressure profile within the matrix blocks. From the ideal gas law, the coupling between late-time pressure and matrix pressure is:

$$\frac{\partial \mathrm{P_L}(t)}{\partial \mathrm{t}} = -\frac{V_{pm}}{V_L}\frac{\partial \bar{P}_m}{\partial t}, \quad x = 0, t > 0 \qquad [3.66]$$

Solutions:

This system of equations has an exponential solution. Average pressure within the matrix is:

$$\frac{\bar{P}_m(t) - P_{eqb}}{(P_0 - P_{eqb})} = \exp\left(-\frac{k_m \alpha}{\Phi_1(\overline{\mu C})_L}\left(\frac{V_L + V_{pm}}{V_L}\right)t\right) \qquad [3.67]$$

Average pressure within the late-time system is:

$$\frac{\bar{P}_L(t) - P_{eqb}}{(P_{conv} - P_{eqb})} = \exp\left(-\frac{k_m \alpha}{\Phi_1(\overline{\mu C})_L}\left(\frac{V_L + V_{pm}}{V_L}\right)t\right) \qquad [3.68]$$

The $\ln\left|\frac{\bar{P}_L(t) - P_{eqb}}{P_{conv} - P_{eqb}}\right|$ is:

$$\ln\left|\frac{\bar{P}_L(t) - P_{eqb}}{P_{conv} - P_{eqb}}\right| = -\frac{k_m \alpha}{\Phi_1(\overline{\mu C})_L}\left(\frac{V_L + V_{pm}}{V_L}\right)t \qquad [3.69]$$

Matrix permeability is normally calculated by determining the best-fit linear slope (m_L) to a plot of $\ln\left|\frac{\bar{P}_L(t) - P_{eqb}}{P_{conv} - P_{eqb}}\right|$ versus time:

$$k_m = -\frac{\Phi_1(\overline{\mu C})_L}{\alpha}\left(\frac{V_L}{V_L + V_{pm}}\right)m_L \qquad [3.70]$$

APPENDIX 3C: SUPPLEMENTAL CEMENT CHARACTERIZATION DATA

Table 3.4 Helium porosimetry data for intact cement matrix in CI-01 at ambient stress using the pulse-decay apparatus and methods illustrated in **Figure 4.4**.

Test #	P_{Rvac} [psig]	P_{R0} [psig]	P_{Reqb} [psig]	ϕ_{He} [%]
1	-13.520	201.976	-0.77	15.25%
2	-14.568	202.465	-1.65	14.21%
3	-14.571	202.21	-1.692	14.53%
4	-14.589	159.301	-4.234	14.13%
5	-14.406	203.881	-1.412	14.19%
6	-14.384	202.946	-1.416	13.77%
7	-13.983	203.148	-1.046	14.03%
Volumes [cc]			Average Porosity [%]	14.30%
V_R	0.904		Standard Deviation [p.u.]	0.47
V_{ch}	36.184	Standard Deviation [as % of Average Porosity]		3.32%
V_{Billet}	14.392			
V_B	8.750			

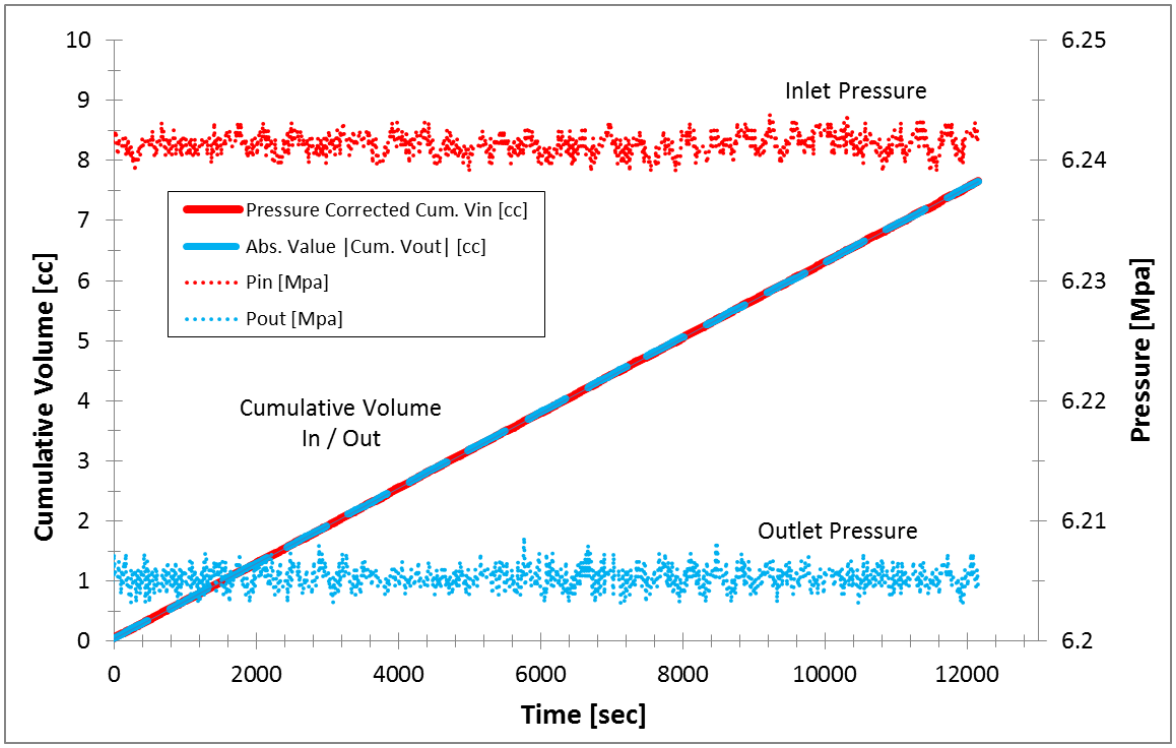

Figure 3.13 Cumulative volumes and pore pressure versus time measured at the upstream and downstream ends of intact core sample CI-01. The cumulative volume injected upstream is pressure corrected for expansion and referenced to outlet pressure. The average differential pressure ($P_2 - P_1$) was -0.36 MPa. Mean pore pressure is 6.22 MPa and absolute confining pressure is 29.7 MPa. The average flow rate at the upstream face is equal to the best-fitting linear slope to the cumulative downstream volume versus time, which is 6.25 $x10^{-4} cc/s$. The maximum pressure gradient was $(-9.5\frac{kPa}{cm}, -3.5\frac{psi}{in})$ to minimize inertial-turbulent effects which can occur for gradients exceeding $(-27\frac{kPa}{cm}, -10\frac{psi}{in})$ ((API) 1998). The steady-state permeability to Argon gas is 3.4 $x10^{-17} m^2$.

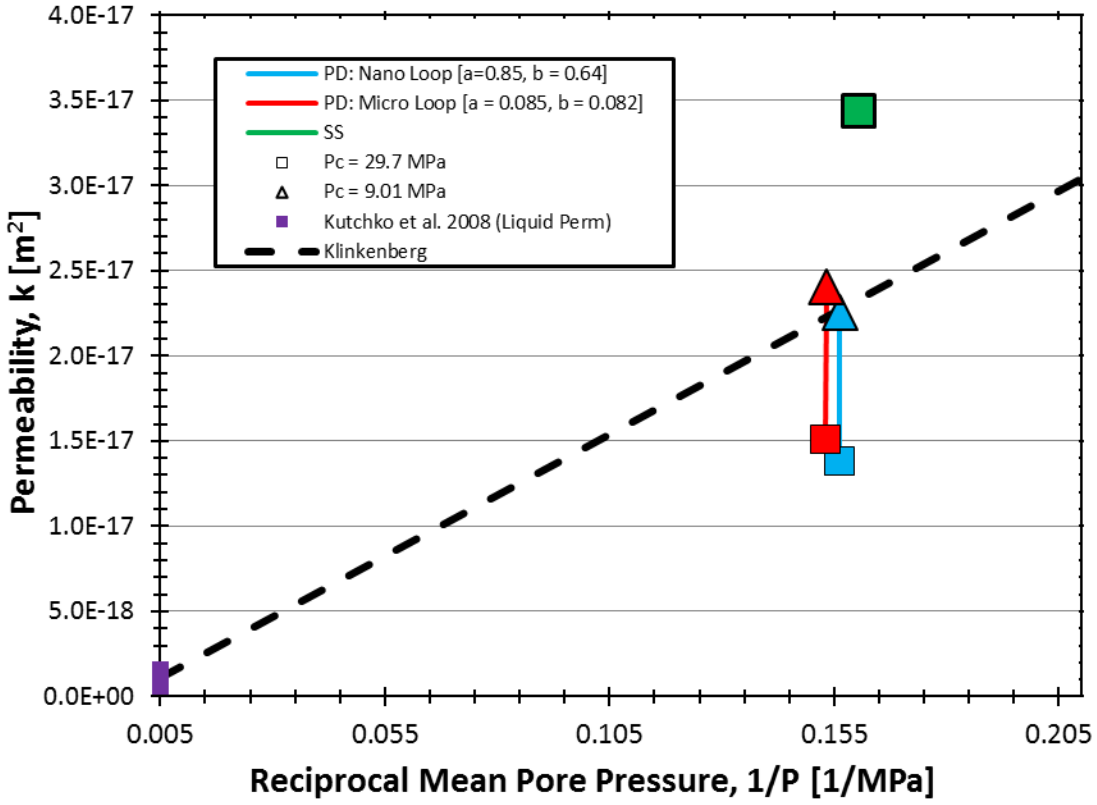

Figure 3.14 Permeability versus reciprocal mean pore pressure for the intact cement core sample. Squares correspond to tests conducted at high confining stress (P_c = 29.7 MPa) and triangles to low confining stress (P_c = 9.01 MPa). Blue lines correspond to tests conducted with the "nano-loop" configuration where reservoir volume is approximately equal to sample pore volume. Red lines correspond to tests conducted with the "micro-loop" where reservoir volumes are approximately 6 times the sample pore volume. The steady-state permeability value (green square) is slightly greater than the pulse-decay values. In addition, permeability decreases with increasing confining stress and increasing mean pore pressure. Pulse-decay permeability values range between $[1.5 - 2.7]x10^{-17}m^{-2}$. Black dashed line is the inferred Klinkenberg gas slip dependence line. Kutchko et al. (2008) report that absolute ("liquid") permeability in Class H Portland cement is on the order of ~ $(1.1x10^{-18}m^2, 1.1\ \mu D)$.

ACKNOWLEDGEMENTS

I thank James Patterson from the Department of Petroleum and Geosystems Engineering for his assistance in preparing the cement core samples. In addition, I thank Athma Bhandari and Peter Polito for help conducting the permeability and porosimetry experiments. Finally, I thank all the petroleum engineering and geoscience professors at the Pennsylvania State University and the University of Texas for teaching me how to use finite-difference methods.

REFERENCES

(API), A.P.I.: Recommended Practices for Core Analysis (2nd Edition). In: Exploration and Production Department, vol. Recommended Practice 40. API Publishing Services, 1220 L Street, N.W., Washington, D.C. 20005, (1998)

API: 10B-2/ISO 10426-2: 2005. In: Recommended Practice For Testing Well Cement. (2005)

Bird, R.B., Stewart, W.E., Lightfoot, E.N.: Transport Phenomena, Second ed. John Wiley & Sons, Inc., Hoboken, NJ (2007)

Cronin, M.B.: Using Brazilian Disk Tests to Define Tensile Strength of Lithologies in the Lower Oatka Creek and Upper Cherry Valley Members of the Marcellus Shale. Senior Thesis in Geosciences, Pennyslvania State University (2011)

Dandekar, A.Y.: Petroleum reservoir rock and fluid properties. CRC press, (2013)

Dicker, A.I., Smits, R.M.: A Practical Approach for Determining Permeability From Laboratory Pressure-Pulse Decay Measurements. Paper presented at the International Meeting on Petroleum Engineering, Tianjin, China, 01/01/1988

Ertekin, T., Abou-Kassem, J.H., King, G.R.: Basic Applied Reservoir Simulation. SPE Textbook Series vol. Vol. 7. Society of Petroleum Engineers, (2001)

Hondros, G.: The evaluation of Poisson's ratio and the modulus of materials of a low tensile resistance by the Brazilian (indirect tensile) test with particular reference to concrete. Australian Journal of Applied Science 10(3), 243-268 (1959)

Kamath, J., Boyer, R.E., Nakagawa, F.M.: Characterization of Core-Scale Heterogeneities Using Laboratory Pressure Transients. SPE Formation Evaluation September (1992)

Kazemi, H., Merrill Jr., L.S., Porterfield, K.L., Zeman, P.R.: Numerical Simulation of Water-Oil Flow in Naturally Fractured Reservoirs. Society of Petroleum Engineers Journal 16(6), 317-326 (1976). doi:10.2118/5719-pa

Kutchko, B.G., Strazisar, B.R., Lowry, G.V., Dzombak, D.A., Thaulow, N.: Rate of CO2 attack on hydrated Class H well cement under geologic sequestration conditions. Environmental science & technology 42(16), 6237-6242 (2008)

Lim, K.T., Aziz, K.: Matrix-fracture transfer shape factors for dual-porosity simulators. Journal of Petroleum Science and Engineering(13), 169-178 (1995)

Nickalls, R.: Viète, Descartes and the cubic equation. The Mathematical Gazette 90(518) (2006)

Ning, X.: The measurement of matrix and fracture properties in naturally fractured low permeability cores using a pressure pulse method. Texas A&M University (1992)

Reid, R.C., Prausnitz, J.M., Poling, B.E.: The Properties of Gases & Liquids, 4th ed. McGraw-Hill Book Company, New York (1987)

Taylor, H.F.: Cement chemistry. Thomas Telford, (1997)

Warren, J.E., Root, P.J.: The Behavior of Naturally Fractured Reservoirs. Society of Petroleum Engineers Journal(September), 245-255 (1963)

CHAPTER 4: APPENDICES

Appendix 4A: Thesis Nomenclature

Table 4.1 Thesis Nomenclature- M: mass, L: length, T: time, Θ: temperature, (-): integer

Symbol	Description and Fundamental Units
English Symbols	
A_c	Characteristic drainage surface area (L^2)
A_f	Cross-sectional area of fractures in x-direction (L^2)
A_{fx_i}	Cross-sectional area of fractured domain in x-direction at node i (**Table 3.2**) (L^2)
A_H	Cross-sectional area of core in x-direction (L^2)
A_{meq}	Equivalent matrix-fracture contact surface area (L^2)
A_{meqX}	Matrix-fracture contact area in x-direction (Eq. [4.70]) (L^2)
A_{meqY}	Matrix-fracture contact area in y-direction (Eq.[4.71]) (L^2)
A_{meqZ}	Matrix-fracture contact area in z-direction (Eq.[4.72]) (L^2)
A_{mx_i}	Cross-sectional area of matrix domain in x-direction at node i (Eq. [4.35]) (L^2)
A_{x_i}	Cross-sectional area of grid-block in x-direction at node i (L^2)
A_{2eq}	Characteristic low-permeability surface area in late-time model (L^2)
a	Ratio of V_{pB} to V_u (Eq.[4.15]) (dimensionless)
a_E	Ratio of V_{p1} to V_u (Eq. [2.32]) (dimensionless)
B_i	Difference equation at boundary node i (1 = Upstream, $N_x + 2$ = Downstream)
B_g	Gas formation volume factor (Eq. [4.23]) ($L_R^3 L_{SC}^{-3}$)
B_{g_f}	Gas formation volume factor in fractured domain ($L_R^3 L_{SC}^{-3}$)
B_{g_m}	Gas formation volume factor in matrix domain ($L_R^3 L_{SC}^{-3}$)
b	Ratio of V_{pB} to V_d (Eq.[4.16]) (dimensionless)
b_E	Ratio of V_{p1} to V_d (Eq.[2.33]) (dimensionless)
C_g	Gas compressibility (isothermal) (Eq. [4.84]) ($M^{-1}LT^2$)
C_{g_f}	Gas compressibility in fractures ($M^{-1}LT^2$)
C_{g_m}	Gas compressibility in matrix ($M^{-1}LT^2$)
CMB	Cumulative mass balance (Eq.[4.86]) ($L_{SC}^3 L_{SC}^{-3}$)
D	Diameter of core (L)
F_i	Difference equation for fracture domain at node i (Eq.[4.24])
$\mathcal{F}$	Combined matrix of difference equations in numerical model (**Table 4.4**)
$f(a,b)$	Eq. A15 in Dicker and Smits (1988) (rad^2)
$f(x_i,\beta)$	Model value at data point x_i
H	Thickness of model (with equal cross-sectional area to core of diameter D) (L)
H_1	Cumulative thickness of high-permeability layers (L)
H_2	Cumulative thickness of low-permeability layers (L)
h_{mx}	Thickness of matrix block in x-direction (L)
h_{my}	Thickness of matrix block in y-direction (L)
h_{mz}	Thickness of matrix block in z-direction (L)
h_1	Thickness of high -permeability layers (L)
h_2	Thickness of low-permeability layers (L)
IMB	Incremental mass balance (Eq. [4.85]) ($L_{SC}^3 L_{SC}^{-3}$)
J^v	Jacobian matrix (evaluated at iteration level v) for numerical model (Eq. [4.48])

Table 4.1, cont.

k_f	Permeability of fractures (L^2)
k_{fH}	Effective horizontal permeability of fractured core (L^2)
k_{fH_x}	Effective fracture permeability in x-direction for numerical model (L^2)
k_H	Effective horizontal permeability of homogeneous core (L^2)
k_{fx}	Permeability of fractures in x-direction (L^2)
k_{fy}	Permeability of fractures in y-direction (L^2)
k_{fz}	Permeability of fractures in z-direction (L^2)
$\aleph_i$	Indicial location of finite-difference equations in matrix $\mathcal{F}$ (**Table 4.4**)
k_m	Permeability (isotropic) of matrix (L^2)
k_{meq}	Equivalent matrix permeability for shape-factor (L^2)
k_{mx}	Permeability of matrix in x-direction (L^2)
k_{my}	Permeability of matrix in y-direction (L^2)
k_{mz}	Permeability of matrix in z-direction (L^2)
k_V	Effective vertical permeability (L^2)
k_1	Isotropic layer permeability in high-permeability layers (L^2)
k_2	Isotropic layer permeability in low-permeability layers (L^2)
L	Length of core (m)
L_{eq}	Equivalent core length in late-time layered core sample model (m)
L_{meq}	Equivalent length of matrix (L)
L_{meqX}	Equivalent length of matrix in x-direction (Eq.[4.73]) (L)
L_{meqY}	Equivalent length of matrix in y-direction (Eq.[4.74]) (L)
L_{meqZ}	Equivalent length of matrix in z-direction (Eq.[4.75]) (L)
M	Indicial replacement for sum, $m = 0, \ldots \infty$ (Eq. [2.42]) (-)
M_i	Difference equation for matrix domain at node i (Eq.[4.25])
m	Indicial index for summation (Eq. [2.42]) (-)
m_E	Early-time model dimensionless pressure dissipation slope (T^{-1})
m_L	Late-time model dimensionless pressure dissipation slope (T^{-1})
N_F	Number of fractures in a given plane (-)
N_{FX}	Number of fractures in x-direction (-)
N_{FY}	Number of fractures in y-direction (-)
N_{FZ}	Number of fractures in z-direction (-)
N_x	Number of grid blocks in x-direction in numerical model (-)
N_t	Number of time-steps in numerical model (-)
N_1	Number of high-permeability layers (-)
N_2	Number of low-permeability layers (-)
$N_\perp$	Number of mutually orthogonal preferential flow-path planes (dimensionless)
P	Pressure (absolute) ($ML^{-1}T^{-2}$)
P_{B_i}	Pressure in boundary node i (1 = Upstream, $N_x + 2$ = Downstream) ($ML^{-1}T^{-2}$)
P_C	Absolute (hydrostatic) confining pressure ($ML^{-1}T^{-2}$)
P_{conv}	Early-time reservoir convergence pressure ($ML^{-1}T^{-2}$)
P_D	Dimensionless pressure scaled between P_{u0} and P_0 (dimensionless)
P_d	Pore pressure in downstream reservoir ($ML^{-1}T^{-2}$)
P_{dD}	Dimensionless downstream reservoir pressure scaled between P_{u0} and P_0 (dimensionless)
P_{eqb}	Late-time final equilibrium pressure ($ML^{-1}T^{-2}$)
P_{F_i}	Pressure in the fracture domain at node i ($ML^{-1}T^{-2}$)

Table 4.1, cont.

$\bar{P}_f$	Average pore pressure within the fracture domain ($ML^{-1}T^{-2}$)
P_L	Volume-averaged reservoir pressure "late-time pressure" ($ML^{-1}T^{-2}$)
P_{LD}	Dimensionless P_L scaled between P_{u0} and P_0 (Eq. [3.6]) (dimensionless)
P_{M_i}	Pore pressure in the matrix domain at node i ($ML^{-1}T^{-2}$)
$\bar{P}_m$	Average pore pressure within the matrix domain ($ML^{-1}T^{-2}$)
P_p	Average pore pressure ($ML^{-1}T^{-2}$)
P_{SC}	Pressure at standard conditions ($ML^{-1}T^{-2}$)
P_u	Pore pressure in upstream reservoir scaled between P_{u0} and P_0 ($ML^{-1}T^{-2}$)
P_{uD}	Dimensionless upstream reservoir pressure (dimensionless)
P_{u0}	Initial upstream reservoir pressure (after opening main valve) ($ML^{-1}T^{-2}$)
$\vec{P}^n$	Nodal pressures at time-level n ($ML^{-1}T^{-2}$)
$\vec{P}^{n+1}$	Nodal pressures at time-level $n+1$ ($ML^{-1}T^{-2}$)
$\vec{P}^v$	Nodal pressures at iteration level v ($ML^{-1}T^{-2}$)
$\vec{P}^{v+1}$	Nodal pressures at iteration level $v+1$, (Eq. [4.45]) ($ML^{-1}T^{-2}$)
$\vec{P}^{v=0}$	Extrapolated nodal pressures for initial iteration, (Eq.[4.47]) ($ML^{-1}T^{-2}$)
P_2	Pore pressure within the low-permeability layers ($ML^{-1}T^{-2}$)
$\bar{P}_2$	Average pore pressure within the low-permeability layers ($ML^{-1}T^{-2}$)
P_1	Pore pressure within the high-permeability layers ($ML^{-1}T^{-2}$)
P_0	Initial system pore pressure ($ML^{-1}T^{-2}$)
q_{eqX}	Flux between matrix and fractures in x-direction (Eq. [4.67]) ($M\,T^{-1}$)
q_{eqY}	Flux between matrix and fractures in y-direction (Eq.[4.68]) ($M\,T^{-1}$)
q_{eqZ}	Flux between matrix and fractures in z-direction (Eq.[4.69]) ($M\,T^{-1}$)
q_{Leak_i}	Sink term for leak in one of the reservoirs (Eq. [4.42]) ($L_{SC}^3T^{-1}$)
q_{mf_i}	Inter-domain flux between fractures and matrix at node i (Eq. [4.26]) ($L_{SC}^3T^{-1}$)
q_T	Sum of q_{eqX}, q_{eqY} , q_{eqZ} (for shape-factor calculation) ($M\,T^{-1}$)
r	Pore radius (L)
r_i	Residual for point x_i in least-squares minimization problem (Eq. [4.88])
S	Sum of the residuals squared (Eq. [4.87])
S_f	Fracture spacing (L)
S_{fX}	Fracture spacing in x-direction (L)
S_{fY}	Fracture spacing in y-direction (L)
S_{fZ}	Fracture spacing in z-direction (L)
S_z	Layer spacing in the z-direction (L)
$\bar{s}$	Laplace transform variable
T	Fluid temperature (absolute) (Θ)
T_{SC}	Fluid temperature (absolute) at standard conditions (Θ)
T_V	Terzhagi (1943) dimensionless time-factor (Eq. [2.41]) (dimensionless)
TXn_i	Transmissibility in negative x-direction at node i ($L_{SC}^4TM^{-1}$)
TXn_{BF_i}	" at downstream-fracture interface ($i = N_x + 2$) (Eq. [4.40]) ($L_{SC}^4TM^{-1}$)
TXn_{BM_i}	" at downstream-matrix interface ($i = N_x + 2$) (Eq. [4.41]) ($L_{SC}^4TM^{-1}$)
TXn_{F_i}	" in fractured domain at node i (Eq. [4.32]) ($L_{SC}^4TM^{-1}$)
TXn_{M_i}	" in matrix domain at node i (Eq. [4.33]) ($L_{SC}^4TM^{-1}$)
TXp_i	Transmissibility in positive x-direction at node i ($L_{SC}^4TM^{-1}$)
TXp_{BF_i}	" at upstream reservoir-fracture interface ($i = 1$) (Eq. [4.38]) ($L_{SC}^4TM^{-1}$)

Table 4.1, cont.

TXp_{BM_i}	" at upstream reservoir-matrix interface ($i = 1$) (Eq. [4.39]) ($L_{SC}^4 TM^{-1}$)
TXp_{F_i}	" in fractured domain at node i (Eq. [4.30]) ($L_{SC}^4 TM^{-1}$)
TXp_{M_i}	" in matrix domain at node i (Eq. [4.31]) ($L_{SC}^4 TM^{-1}$)
t	Time (T)
t^n	Time at time-level n (T)
t_{conv}	Timescale for initial reservoir pressure convergence (T)
t_D	Dimensionless time (dimensionless)
t_{eqb}	Timescale for system to reach final equilibrium pressure (T)
t_{fD}	Dimensionless fracture time (dimensionless)
t_L	Late-time model time, $t_L = t - \tau_E$ (T)
t_{LD}	Dimensionless time in late-time model (dimensionless)
V_B	Bulk volume of the core sample (m^3)
V_{B1}	Bulk volume of all the high-permeability layers (L^3)
V_{B2}	Bulk volume of all the low-permeability layers (L^3)
V_{b_i}	Bulk volume of the grid-element i in numerical model (L^3)
V_d	Downstream reservoir volume (L^3)
V_L	Late-time system volume (L^3)
V_{pB}	Total pore volume of core (L^3)
V_{pE}	Pore volume at "early-time" reservoir convergence pressure (L^3)
V_{pf}	Pore volume in fractures (L^3)
V_{pm}	Pore volume in matrix (L^3)
V_{p1}	Pore volume in high-permeability material (L^3)
V_{p2}	Pore volume in low-permeability material (L^3)
V_{res_i}	Reservoir volume at boundary node i (1 = Upstream, $N_x + 2$ = Downstream) (L^3)
V_u	Upstream reservoir volume (L^3)
W	Width of model (with equal cross-sectional area to core of diameter D) (L)
w_f	Fracture aperture (L)
w_{fx}	Fracture aperture in x-direction (L)
w_{fy}	Fracture aperture in y-direction (L)
w_{fz}	Fracture aperture in z-direction (L)
x	Cartesian distance in horizontal flow direction (L)
x_i	Location of data point in least-squares minimization problem
y	Cartesian distance in horizontal plane, perpendicular to flow direction (L)
$y(x_i)$	Actual value of data at point x_i in least-squares minimization problem
Z	Real gas deviation factor (dimensionless)
Z_{conv}	Real gas deviation factor at P_{conv} (dimensionless)
Z_{eqb}	Real gas deviation factor at P_{eqb} (dimensionless)
Z_{SC}	Real gas deviation factor at standard conditions (dimensionless)
Z_{u0}	Real gas deviation factor at P_{u0} (dimensionless)
Z_0	Real gas deviation factor at P_0 (dimensionless)
z	Cartesian distance in vertical direction (perpendicular to bedding) (L)
Greek Symbols	
α	Shape factor (L^{-2})
α_c	Volume conversion factor for customary field units = 5.614583
β_c	Transmissibility conversion factor for customary field units = 1.127

Table 4.1, cont.

β_n	Fitting parameters in least-squares minimization problem
Γ_i	Accumulation term at node i in numerical model difference equations (L_{SC}^3)
Γ_{B_i}	Accumulation term for upstream/downstream (Eqs. [4.36],[4.37]) nodes (L_{SC}^3)
Γ_{F_i}	Accumulation term for fractured domain at node i (Eq. [4.28]) (L_{SC}^3)
Γ_{M_i}	Accumulation term for matrix domain at node i (Eq.[4.29]) (L_{SC}^3)
γ	High to Low-Permeability Layer Porosity Ratio (Eq. [2.2]) (dimensionless)
ΔP	Differential pore pressure, $\Delta P = (P_u - P_d)$ ($ML^{-1}T^{-2}$)
ΔP_D	Dimensionless ΔP, $\Delta P_D = \Delta P/(P_{u0} - P_0)$ (dimensionless)
ΔP_L	Late-time model differential pressure, $\Delta P_L = (P_L - P_{eqb})$ ($ML^{-1}T^{-2}$)
ΔP_{LD}	Dimensionless ΔP_L, $\Delta P_{LD} = \Delta P_L/(P_{conv} - P_0)$ (dimensionless)
Δx_i	Width of grid block i in numerical model (L)
Δt^n	Size of time-step at time-level n in numerical model ($ML^{-1}T^{-2}$)
ε_{Der}	Small step in function argument in central difference derivative (Eq. [4.42])
ε_{Tol}	Convergence tolerance for Newton-Rhapson iteration (Eq. [4.44])
λ	High to low-permeability layer transmissibility ratio (dimensionless)
λ_f	Fractures to matrix transmissibility ratio (dimensionless)
μ	Dynamic gas viscosity ($ML^{-1}T^{-1}$)
μ_{g_f}	Dynamic gas viscosity in fractures ($ML^{-1}T^{-1}$)
μ_{g_m}	Dynamic gas viscosity in matrix ($ML^{-1}T^{-1}$)
$\bar{\mu}_{g_{mf}}$	Average dynamic viscosity between matrix and fractures ($ML^{-1}T^{-1}$)
$\overline{\mu C}$	Average viscosity-compressibility product (T)
$\overline{\mu C}_E$	Average viscosity-compressibility product in early-time model (T)
$\overline{\mu C}_L$	Average viscosity-compressibility product in late-time model (T)
ρ	Fluid density (ML^{-3})
ρ_{SC}	Fluid density at standard conditions (ML^{-3})
τ	Characteristic timescale ratio: $\tau = t_{eqb}/t_{conv}$ (dimensionless)
τ_f	Characteristic timescale ratio in fractured core sample (dimensionless)
Φ_1	Fraction of "primary" pore volume to core bulk volume (Eq. [3.7]) (fraction)
Φ_2	Fraction of "secondary" pore volume to core bulk volume (Eq. [3.8]) (fraction)
Φ_{mi}	Value of Φ_1 in grid block node i (fraction)
Φ_{fi}	Value of Φ_2 in grid block node i (fraction)
ϕ	Porosity (fraction)
ϕ_B	Bulk porosity of entire core (fraction)
ϕ_E	Apparent bulk porosity of entire core at early-time (fraction)
ϕ_f	Intrinsic porosity of fractures (fraction)
ϕ_{He}	Bulk helium porosity of core sample (fraction)
ϕ_m	Intrinsic porosity of matrix (fraction)
ϕ_1	Porosity in high permeability layers (fraction)
ϕ_2	Porosity in low permeability layers (fraction)
ω	Fraction of V_{p1} to $V_{p1}+ V_{p2}$ (Eq. [2.1]) (dimensionless)
ω_f	Fraction of V_{pf} to $[V_{pf}+ V_{pm}]$ (Eq.[3.10]) (dimensionless)
Common Subscripts	
B	Bulk core property
D	Dimensionless
E	Early-time system property

Table 4.1, cont.

F	Pertaining to fractures
L	Late-time system property
M	Pertaining to matrix
SC	Standard conditions (60F, 14.7 psia)
X	Pertaining to x-direction
Y	Pertaining to y-direction
X	Pertaining to z-direction
$conv$	Pertaining to early-time reservoir pressure convergence
d	Pertaining to downstream reservoir
eq	Equivalent property
eqb	Pertaining to late-time equilibrium pressure
f	Pertaining to fractures
i	Location of grid node in numerical model
	i =1: Upstream reservoir node
	$1 < i < N_x + 2$: Grid nodes within core sample
	$i = N_x + 2$: Downstream reservoir node
m	Pertaining to matrix
p	Pertaining to pore volume (within core)
u	Pertaining to upstream reservoir
x	Pertaining to x-direction
y	Pertaining to y-direction
z	Pertaining to z-direction
0	Original value
1	Primary "matrix" domain (fractured model)
	High-permeability layers (layered model)
2	Secondary "fractured" domain (fractured model)
	Low-permeability layers (layered model)
Common Superscripts	
n	Time-level
v	Iteration-level
Unit Abbreviations	
$p.u.$	Porosity units
TOC	Total organic carbon by weight percent
Common Operators	
Δ	Difference
∂	Differential
Σ	Summation
$\bar{}$	Average
$\rightarrow$	Denotes vector

Appendix 4B: Pulse-Decay Theory of Homogeneous Cores

In this section, I briefly present the solution for pulse-decay behavior of homogeneous core samples in a fixed-volume pulse-decay apparatus. I present the Dicker and Smits (1988) solution because it simplifies the Hsieh et al. (1981) model for ease of use in petroleum-related investigations. Jones (1997) also presents an excellent summary. I encourage readers to consult these references for a more thorough derivation of the analytical pulse-decay solution for homogeneous cores. In addition, the pressure-diffusion equation [4.1] has been solved for constant downstream pressure (Bourbie et al. 1983) and oscillating reservoir pressure (Suri et al. 1997) boundary conditions.

The pressure diffusion equation [1.2] (shown below in one-dimension) describes fluid flow in homogeneous porous media with isotropic permeability (k) and constant porosity (ϕ). P is pressure, x is the Cartesian spatial coordinate, t is time, and C is fluid compressibility.

$$\frac{\partial^2 P}{\partial x^2} = \frac{\phi \mu C}{k} \frac{\partial P}{\partial t} \qquad [4.1]$$

A pulse-decay apparatus with fixed volume reservoirs upstream and downstream (**Figure 1.1**) has the following initial ([4.2],[4.3],[4.4]) and boundary ([4.5],[4.6],[4.7],[4.8],[4.9]) conditions when the pressure pulse is introduced upstream. Hsieh et al. (1981) solved the pressure diffusion equation [4.1] for these conditions to relate transient reservoir pressure time-series data to permeability in a homogeneous core sample. V_{pB} is the bulk pore volume of the core sample with diameter (D) [4.10]. V_u and V_d refer to the volume of the upstream and downstream reservoirs respectfully. P is pressure within the core sample and P_u and P_d refer to upstream and downstream reservoir pressures respectively.

At initial conditions ($t = 0$), the downstream reservoir and core sample are in pore-pressure equilibrium at the base system pressure (P_0) [4.3] and [4.4] while the upstream reservoir pressure is at an elevated "pulse pressure" (P_{u0}) [4.2]. Upstream reservoir pressure immediately declines after the main valve (**Figure 1.1a**) is opened because the upstream reservoir is hydraulically connected to the upstream face of the core [4.5] and fluid is flowing into the upstream face of the core. Equation [4.6] expresses the hydraulic connection at the downstream core face. The negative sign in [4.8] enforces that the downstream reservoir pressure increases through time (while upstream reservoir pressure always decreases through time [4.7]) due to conservation of mass. After a long time, pore pressure in the core sample and the reservoirs will equilibrate at the "final equilibrium" pressure (P_{eqb}) [4.9].

Initial Conditions:

$$\mathrm{P_u}(0) = P_{u0} \quad [4.2]$$

$$\mathrm{P_d}(0) = P_0 \quad [4.3]$$

$$\mathrm{P}(x, 0) = P_0, \quad 0 < x < L \quad [4.4]$$

Boundary Conditions:

$$\mathrm{P_u}(t) = P(x = 0, t), \quad t > 0 \quad [4.5]$$

$$\mathrm{P_d}(t) = P(x = L, t), \quad t \geq 0 \quad [4.6]$$

$$\frac{\partial \mathrm{P_u}}{\partial \mathrm{t}} = \frac{k}{\phi_B \mu C L} \frac{V_{pB}}{V_u} \frac{\partial P}{\partial x}, \quad x = 0, t > 0 \quad [4.7]$$

$$\frac{\partial \mathrm{P_d}}{\partial \mathrm{t}} = -\frac{k}{\phi_B \mu C L} \frac{V_{pB}}{V_d} \frac{\partial P}{\partial x}, \quad x = L, t > 0 \quad [4.8]$$

$$\mathrm{P_u(t) = P(x,t) = P_d(t) = P_{eqb}}, \quad 0 < x < L, t = \infty \tag{4.9}$$

$$V_{pB} = \tfrac{1}{4}\phi_B \pi D^2 L \tag{4.10}$$

Dicker and Smits (1988) use the Laplace Transform to obtain the analytical solutions to [4.1] for upstream, downstream, and differential reservoir pressures versus dimensionless time (t_D) for conditions [4.2] - [4.9]. In the dimensionless time domain, these solutions are:

Dimensionless time (t_D):

$$t_D = \frac{k}{\phi_B \overline{\mu C} L^2} t \tag{4.11}$$

Dimensionless upstream pressure ($\mathrm{P_{uD}}$):

$$\frac{P_u(t_D) - P_d(0)}{P_u(0) - P_d(0)} = \frac{b}{a+b+ab} + 2\sum_{m=1}^{\infty} \frac{\exp(-t_D\theta_m^2)(ab^2 + a\theta_m^2)}{[(\theta_m^4 + \theta_m^2(a+a^2+b+b^2) + a_E b_E(a+b+ab)]cos\theta_m} \tag{4.12}$$

Downstream downstream pressure ($\mathrm{P_{dD}}$):

$$\frac{P_d(t_D) - P_d(0)}{P_u(0) - P_d(0)} = \frac{b}{a+b+ab} + 2\sum_{m=1}^{\infty} \frac{\exp(-t_D\theta_m^2)(ab^2 - b\theta_m^2)}{[(\theta_m^4 + \theta_m^2(a+a^2+b+b^2) + ab(a+b+ab)]cos\theta_m} \tag{4.13}$$

Dimensionless differential pressure (ΔP_D):

$$\frac{P_u(t_D) - P_d(t_D)}{P_u(0) - P_d(0)} = 2\sum_{m=1}^{\infty} \frac{\exp(-t_D\theta_m^2)a(b^2+\theta_m^2) - (-1)^m b[(a^2+\theta_m^2)(b^2+\theta_m^2)]^{0.5}}{[(\theta_m^4 + \theta_m^2(a+a^2+b+b^2) + ab(a+b+ab)]} \tag{4.14}$$

Where a is the ratio of pore volume to upstream reservoir volume [4.15], b is the ratio of pore volume to downstream reservoir volume [4.16], and θ_m are the roots to [4.17].

$$a = \frac{V_{pB}}{V_u} \tag{4.15}$$

$$b = \frac{V_{pB}}{V_d} \tag{4.16}$$

$$tan\ \theta = \frac{(a+b)\theta}{(\theta^2 - ab)} \tag{4.17}$$

Pressure dissipation during a pulse-decay experiment is typically expressed in terms of the natural log of dimensionless differential pressure ($\ln|\Delta P_D(t)|$) versus time. This is

because Dicker and Smits (1988) show that permeability directly controls the time needed to reach a particular value of ΔP_D [4.18]:

$$\ln|\Delta P_D(t)| \approx -k\frac{f(a,b)}{\phi\overline{\mu C}L^2}t \quad [4.18]$$

For example, Equation [4.18] states that a pulse-decay experiment will take 10 times longer to reach $\Delta P_D = 0.1$ when $k = 1x10^{-19}m^2$ compared to $k = 1x10^{-18}m^2$ when all other properties are held constant. Therefore, effective permeability in the core (k) is proportional to the pressure dissipation rate observed in an experimental plot of $\ln|\Delta P_D|$ versus time (Dicker et al. 1988) [4.19]:

$$k = -\frac{\phi\overline{\mu C}L^2}{f(a,b)}m \quad [4.19]$$

The linear best-fit slope (m) to the experimental plot of $\ln|\Delta P_D|$ versus time is measured after 90% decay ($\Delta P_D = 0.1$) in the original differential pressure which corresponds to $\ln|\Delta P_D|$ equal to -2.3 (**Figure 1.3**). $\overline{\mu C}$ is the average viscosity-compressibility product. $f(a,b)$ (Dicker et al. 1988) is function of pore volume to reservoir volume ratios [4.20]:

$$f(a,b) = (a+b+ab) - \frac{1}{3}(a+b+0.4132ab)^2 + 0.0744(a+b+0.0578ab)^3 \quad [4.20]$$

$f(a,b)$ approximates the value of (θ_1^2), which is the squared value of the first root to [4.17]. The maximum error using [4.20] to calculate θ_1^2 is small (less than 0.5 %) for all combinations where a and b are each less than 1 (**Figure 4.1**).

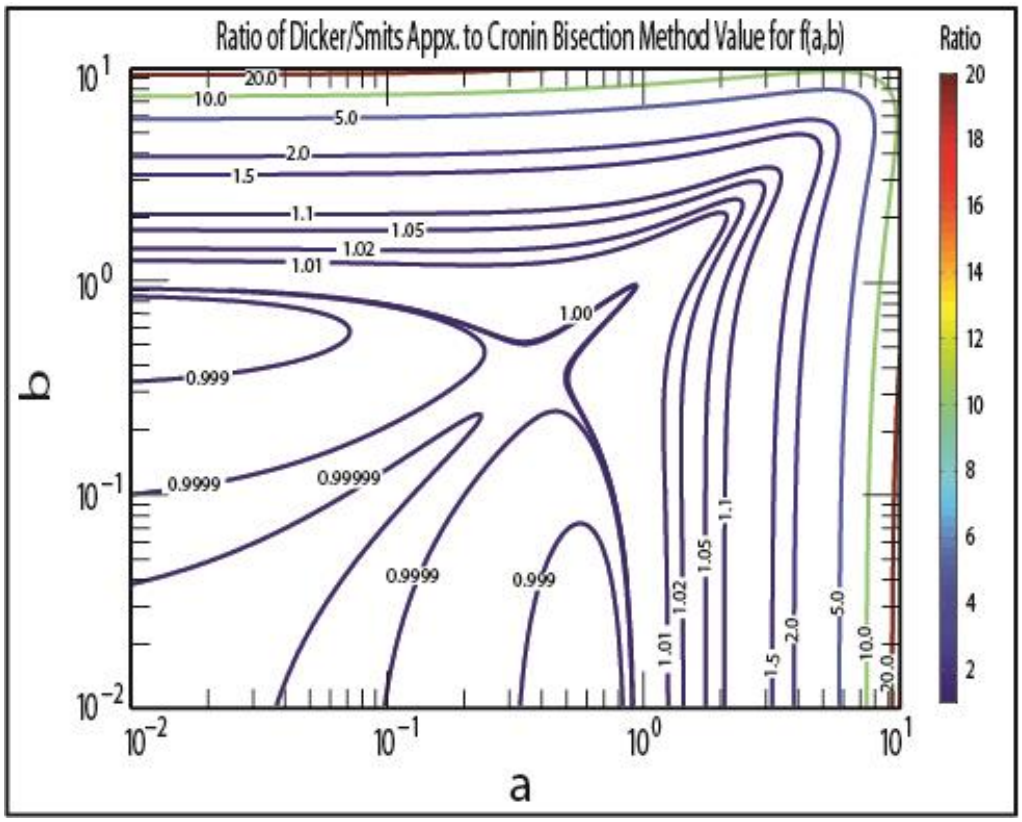

Figure 4.1 Contour plot of the ratio of the Dicker and Smits (1988) $f(a,b)$ approximation to θ_1^2 compared to solution by numerical bisection (tolerance 1E-5). Color corresponds to the ratio. Error is small for all values of a, b less than 1.

Appendix 4C: Supplemental Petrography Data for Barnett Shale Core Samples

ABSTRACT

I present additional petrographic characterization data from the Barnett Shale that was not included in Chapter 2. Supplemental information includes raw helium porosimetry data, additional details on micro-computed x-ray tomography, select photomicrographs from optical microscopy, scanning electron microscopy, and x-ray mapping. I also provide details on how I determined grain-size and mineralogical composition/abundance using digital image analysis.

4C.1: METHODS

Core Plug and Thin-Section Preparation

I obtained Barnett Shale core plugs ($D \approx 38.1\ mm$, $L \approx 25\ mm$) from (2319.5 – 2325.3 m-KB) in the Mitchell Energy T.P. Sims #2 Well, Fort Worth Basin, Texas, U.S.A. core (Loucks et al. 2007; Hickey et al. 2007) using the core sampling method detailed in Bhandari et al. (*in review*). Core plug sample depths are approximate because this depth interval of the core was mishandled at the well-site. 6H1 refers to the horizontal core sample (**Figure 4.2**) that I characterized in Chapter 2 using pulse-decay permeability experiments and my layered dual-permeability model. To preserve core plug 6H1 for future pulse-decay experiments, I used end-trim material from core plug 6H1, which I refer to as "6H1_ET" as well as material from core plug 6H2 (located directly next to 6H1) for destructive analyses.

I prepared specimens for petrographic analysis (optical microscopy, scanning electron microscopy, and x-ray mapping) following the methods described by Milliken et

al. (2012). Uncovered polished thin sections (20 - 25μm thick) for light microscopy and scanning electron microscope (SEM)-based imaging were produced (by Spectrum Petrographics) using surface impregnation with a low-viscosity medium before the final polish to reduce mechanical damage (**Figure 4.3**). Samples were examined in both transmitted and reflected polarized light on a conventional petrographic microscope (Nikon H600L). Carbon-coated thin sections were inspected using an FEI Nova NanoSEM 430 field-emission SEM (FE-SEM); all samples were examined using both secondary electron and backscattered electron (BSE) imaging. Additional observations were made using x-ray mapping (twin 30 mm^2 Bruker XFlash silicon drift detector energy dispersive spectroscopy detectors), as needed. A limited number of SEM images were obtained on milled surfaces prepared by Ar-ion cross section polishing (Leica mill) using an accelerating voltage of 8 kV, sample current of 2.8 mA, and a milling time of 10 hr. Electron microbeam imaging and milling were performed at the Electron Microbeam Laboratory, Department of Geological Sciences, The University of Texas at Austin.

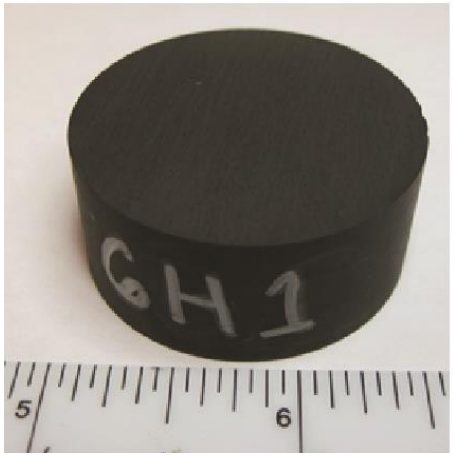

Figure 4.2 Core plug 6H1.

Figure 4.3 High-resolution scanned image of BAR6H1_ET thin section. This thin-section was prepared from an end trim of the 6H1 core plug. Re-worked Ca-phosphate-rich grains (maroon colored) and shell fragments (white) tend to concentrate in thin intervals.

Digital Image Analysis for Grain and Compositional Abundance

Grain and compositional (mineral and organic matter) abundances were determined semi-quantitatively by comparing selected electron and optical photomicrographs, using digital image analysis program JMicrovision© (Roduit 2008). I used a combination, of manual grain boundary tracing, image thresholding, and point-counting. As a preliminary quality-control measure, I verified these digital extractions against comparison charts for visual estimation of coarse fragments (Terry et al. 1955). I incorporated the following independent data: X-ray powder diffraction (XRPD) bulk mineralogy performed by The James Hutton Institute, Scotland, and total organic carbon (TOC) and vitrinite-reflectance (VR_o) thermal maturity measured by Geomark Research Ltd.

X-ray Micro-Computed Tomography

Sample 6H1 was scanned using X-ray micro-computed tomography at ambient temperature and stress conditions by the High-Resolution X-ray CT Facility, Department of Geological Sciences, The University of Texas at Austin. Detailed information on the scan and image reconstruction parameters is provided in **Table 4.2**.

Table 4.2 Core sample 6H1 X-ray computed tomography scan/reconstruction settings.

Requestor: Peter Polito of the Bureau of Economic Geology.
Sample ID & Description: Shale core plug 6H1.
Facility: University of Texas at Austin High-Resolution X-ray CT Facility
Operator/Date: Specimen scanned by Jessie Maisano 10 October 2013.
Scan Parameters: Xradia. 0.7X objective, 110kV, 10W, 2s acquisition time, detector 45 mm, source -72.7 mm, XYZ [-927, -3586, 1392], camera bin 2, angles ±180, 1261 views, 2.1 mm SiO2 filter, dithering, no sample drift correction. End reference (90 frames, each 1s). Reconstructed with center shift -6.5, beam hardening 0.08, theta 0, byte scaling [-15, 300], binning 1, low-contrast ring correction, recon filter smooth (kernel size = 0.5). Total slices = 460.
Output Files:

6H1A.rcp: Xradia recipe with scan parameters.

16bit: 16bit TIFF images reconstructed by Xradia Reconstructor. Voxels are 41.56 microns.

8bitjpg: 8bit jpg version of the reconstructed images.

Helium Porosimetry

I measured core sample porosity to Helium gas (ϕ_{He}) at ambient stress conditions using the apparatus shown (**Figure 4.4**a) and Boyle's Law:

$$\phi_{He} = \frac{\left(\frac{P_{Reqb}}{Z_{Reqb}} - \frac{P_{R0}}{Z_{R0}}\right)V_R + \left(\frac{P_{Rvac}}{Z_{Rvac}} - \frac{P_{Reqb}}{Z_{Reqb}}\right)(V_{ch} - V_{Billet} - V_B)}{\left(\frac{P_{Reqb}}{Z_{Reqb}} - \frac{P_{Rvac}}{Z_{Rvac}}\right)V_B} \quad [4.21]$$

Where P_{Rvac} is the initial pressure in the sample chamber, P_{R0} is the initial pressure in the reference chamber, and P_{Reqb} is the final equilibrium pressure (**Figure 4.4**b). Z_{R0}, Z_{Rvac}, and Z_{Reqb} are gas z-factors ((NIST) 2011) at the pressure indicated in the subscript. V_B is the bulk volume of the core sample, V_{ch} is the empty volume of the sample chamber, and V_R is the volume of the reference chamber. V_{Billet} is the total volume of steel billets placed inside the sample chamber to reduce "dead volume," which is the amount of empty space in the sample chamber. I calculated sample bulk volume using the average measured value for length and diameter. I present calculated helium porosity values in **Table 4.3**.

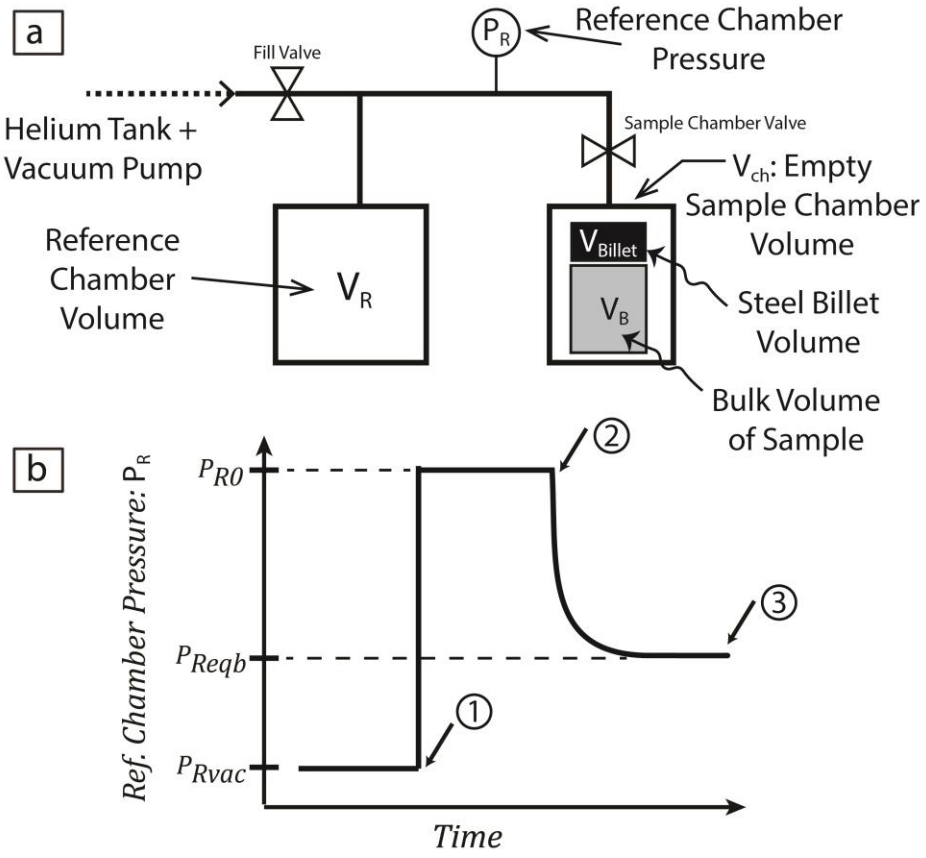

Figure 4.4 Helium porosimetry method. **a**. Experimental apparatus consists of a reference chamber and sample chamber (which holds the sample). Apparatus volumes are calibrated using steel billets of known volume and apparatus temperature is constant. Steel billets are used to reduce empty volume in the sample chamber. **b**. Reference chamber pressure versus time. A vacuum pump is used to lower pressure in the sample chamber and pore volume in the core sample to P_{Rvac}. The sample chamber valve is closed and the reference chamber is pressurized with Helium gas to P_{R0} (1). The gas supply/vacuum valve is closed. Opening the sample chamber valve (2) causes pressure in the two chambers to equalize at P_{Reqb} (3).

Table 4.3 Porosimetry data for intact Barnett Shale core plugs versus crushed samples. These data are discussed in detail by Bhandari et al. (*in review*)

Core Sample	Intact Plug ϕ_{He} [p.u.]	GRI $\phi_{He}^{\dagger}$ [p.u.]	GRI $k^{\dagger}$ [m^2]
2 (Plug 2V)	4.1 ± 1	5.9	99.6 $x10^{-21}$
6 (Plug 6H1)	4.1 ± 1	4.9	36.2 $x10^{-21}$

†: Analyzed by Weatherford, LTD using the GRI "crushed rock" method. Bulk material was crushed to yield less than 3.2-mm-sized material. In a vacuum oven set at 212°F, 85 g of as-received state crushed material is dried. Sample weights are monitored daily until weight stabilization is achieved (±0.01 g). The dried grain volume of each sample is measured by Helium injection using the Boyle's law method. The sample is subjected to a gas permeability determination using a pressure decay method by Luffel et al. (1993).

4C.2: LITHOLOGY DESCRIPTIONS AND GEOLOGIC CONTEXT

Silty-claystone

The light-colored layers in the x-ray computed tomography scans (**Figure 2.1a**) are laminated siliceous silty-claystone (25-30% silt versus 70-75% sub-silt sized particles). The silt-grain size fraction is approximately 30% quartz and 65% dolomite, with remaining 5% comprised of Ca-phosphate, feldspar, and pyrite. Silt grains have a chararacteristic diameter of ~7 μm. Quartz silt appears as isolated grains as well as associated with collapsed agglutinated foraminifera. Dolomite appears as a mixture of anhedral and euhedral rhombs with Ca-Mg zonation. Pyrite primarily occurs as framboids. Ca-phosphate grains are usually present as amalgamated Ca-phosphate, quartz, and carbonate. Ca-phosphate grains typically concentrate in horizons at the

interface between the light and dark layers, and correspond to the elongate bright spots seen in CT imaging. The sub-silt grain-size portion of matrix is a mixture of peloids, clay minerals, and organic matter. Organic matter appears in both stringy "organo-mineralic aggregates" (**Figure 4.20**, **Figure 4.21**) (Macquaker 1994) and angular woody particles (**Figure 4.17**).

Claystone

The dark-colored layers in the x-ray computed tomography scans (**Figure 2.1a**) are significantly finer-grained and contain a larger fraction of sub-silt sized material. The dark layers are laminated, non-fissile siliceous claystone (~ 15 - 25% silt versus 75 - 85% sub-silt sized particles). Silt grains have a characteristic diameter of ~4-5μm. The silt-grain size fraction is approximately 95% quartz, with remaining 5% comprised of Ca-phosphate, pyrite, and dolomite/calcite. Quartz silt appears primarily as isolated grains. Dolomite is near-absent, while pyrite and Ca-phosphate grains appear as previously described in the silty-claystone lithology. The sub-silt portion of matrix is a mixture of euhedral micro-quartz crystals, peloids, clay platelets, and organic matter. Organic matter is highly distributed (**Figure 4.9**, **Figure 4.10**, **Figure 4.11**) with well-developed organic matter hosted pores (**Figure 4.12**, **Figure 4.13**, **Figure 4.14**). Organic matter also appears in an angular, woody form (**Figure 4.8**).

Geologic Context

The silieceous claystone could represent the background flux of slowly accumulating marine snow in a starved basin (Loucks et al. 2007). Milliken et al. (2013) report that matrix-dispersed euhedral micro-quartz crystals (clay size) in the Barnett Shale may be authigenic. The silty-claystone has greater mineral diversity (dolomite,

feldspar), coarser texture, and less clay-sized material. This suggests a more energetic environment where finer grains would be winnowed. The silty-claystone could represent bottom current action or a period of dilute turbidite influx (Loucks et al. 2007). Another possibility is that the silty-claystone represents a period of grain-coarsening due to biological processes and seafloor cementation that produces intraclasts (Milliken et al. 2007). The Ca-phosphate grains show signs of re-working, containing grains of Ca-phosphate and fine-grain dolomite and quartz. Agglutinated forams appear within the silty-claystone as well as near the interface between claystone and silty-claystone. Agglutinated foraminifera are benthic forams, able to tolerate dysoxic conditions (Milliken et al. 2007). Therefore, their presence could indicate periodic, but short-lived oxygenation of bottom water. Alternatively, they could have been entrained in turbidite flows and deposited distally. In summary, I hypothesis that the facies assemblages in 6H1 suggests periodic bottom current action transporting distal sediment and limited quantities of oxygen into a starved basin. This process dilutes and winnows the background marine snow pelagic flux normally comprising the claystone lithology.

4C.3: SELECTED VIEWS OF CLAY-RICH LITHOLOGY

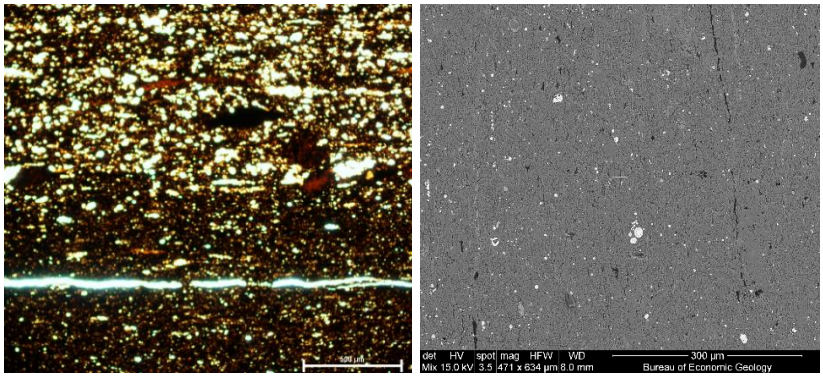

Figure 4.5 Left: PP view of the dark (clay-rich) and light (silty) lithology interface. There is minimal calcite, dolomite, and Ca-phosphate. Right: SEM image of the clay-rich matrix.

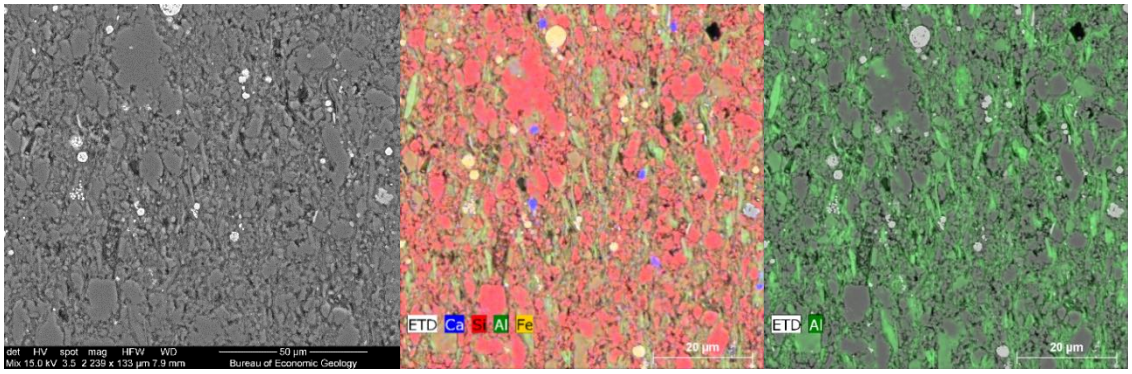

Figure 4.6 Clay-rich matrix shows fine-grained quartz and clay minerals in polished thin section 5PU-001 (6H2). There is minimal calcite, dolomite, and Ca-phosphate. Left: SEM image. Middle and Right: EDS map of elements for five different elements.

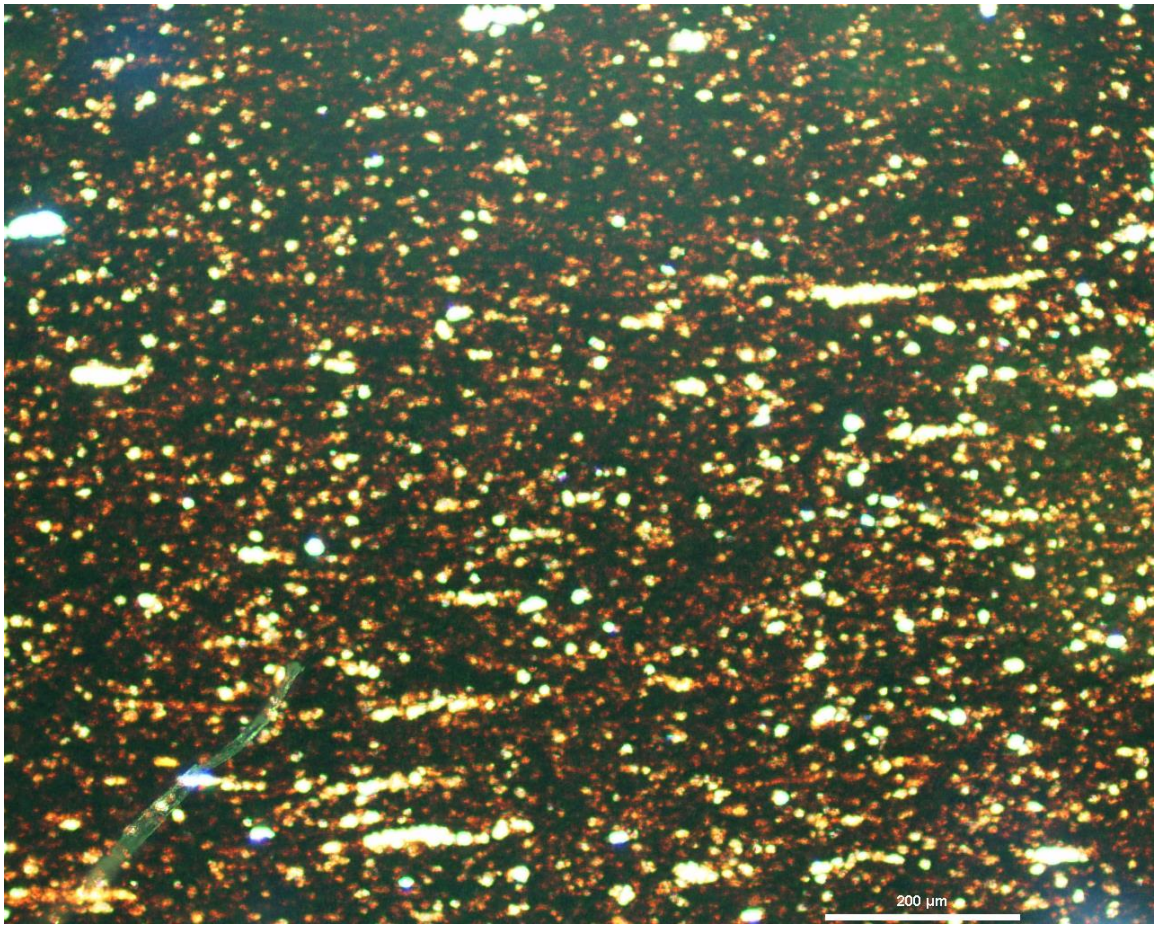

Figure 4.7 Claystone lithology in plane-polarized (PP) light.

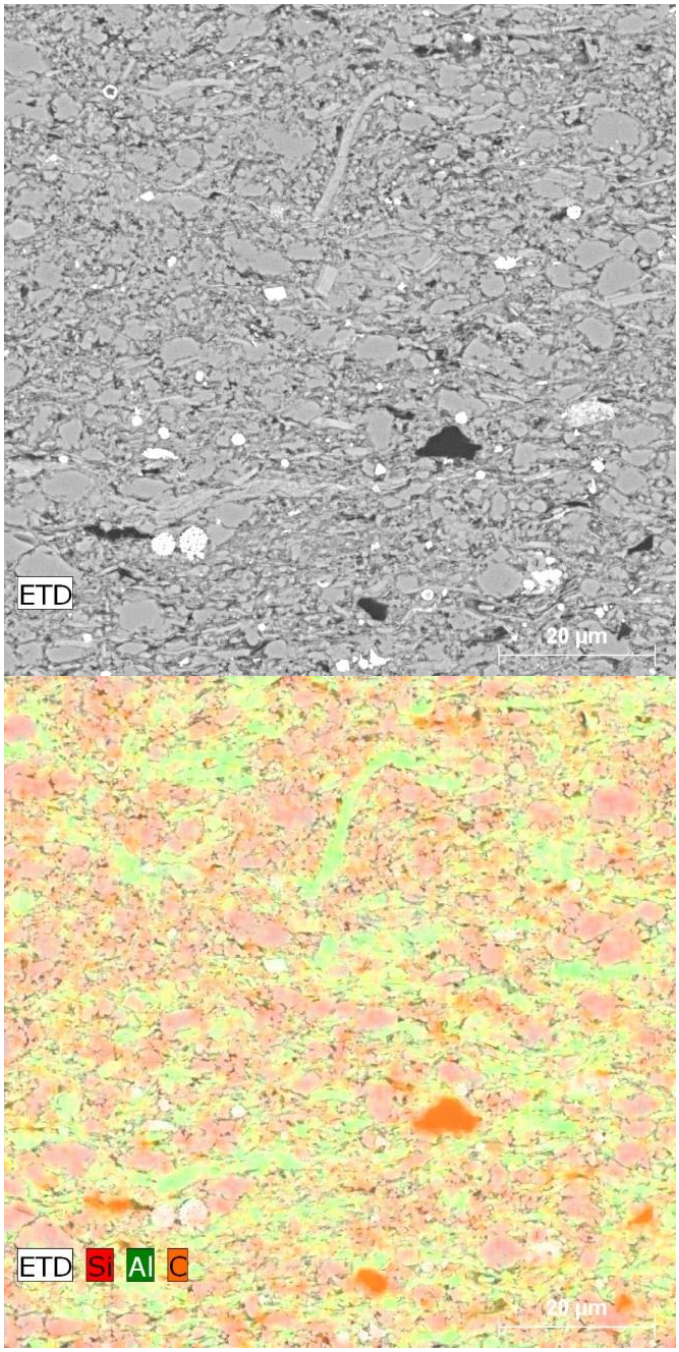

Figure 4.8 Mixed SE/BSE image (top) and EDS map (bottom) of claystone lithology. Mineral content is primarily clay and sub-silt size detrital quartz grains.

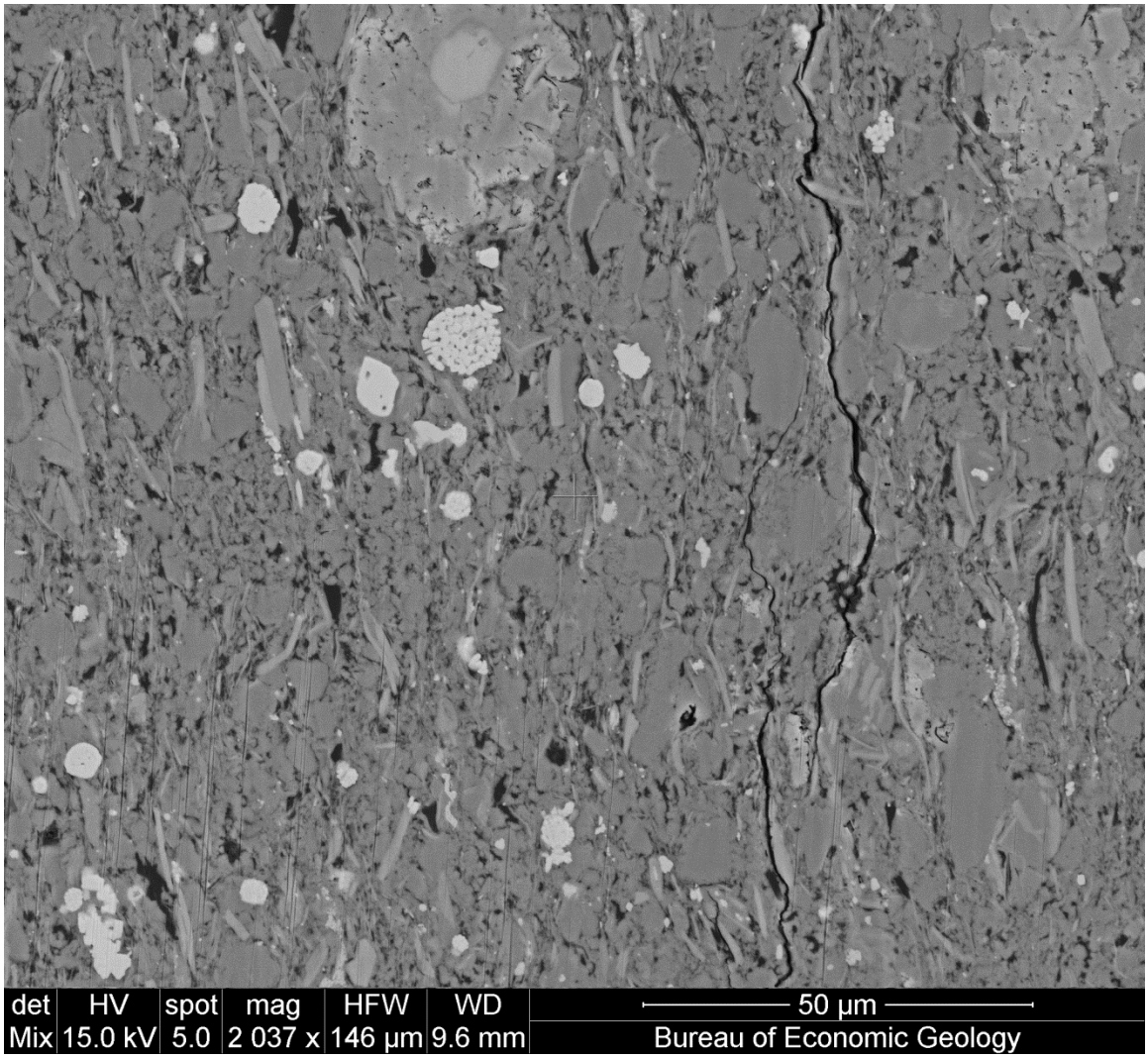

Figure 4.9 Mixed SE/BSE image on ion-milled surface within the claystone.

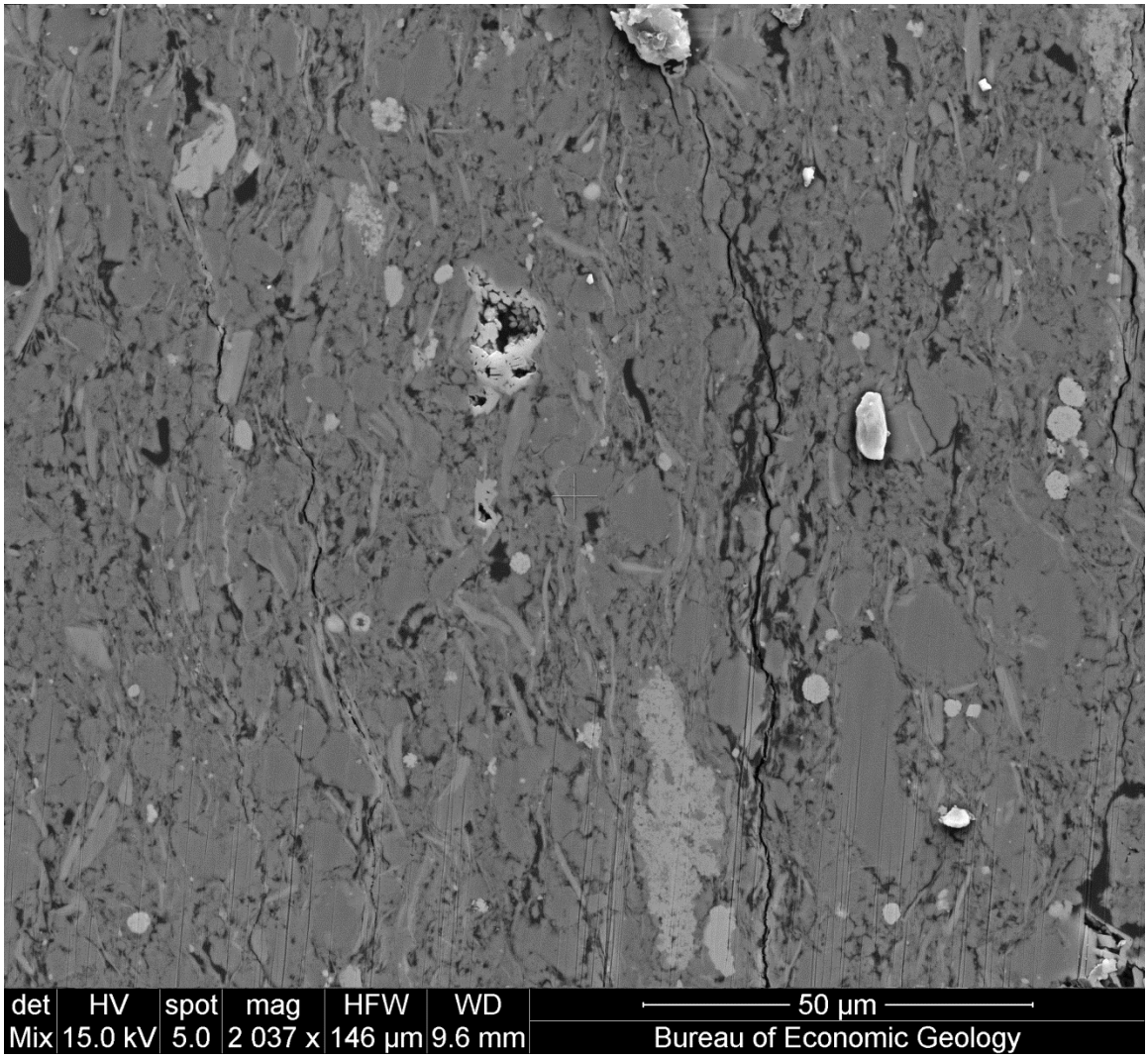

Figure 4.10 Mixed SE/BSE image on ion-milled surface within the claystone.

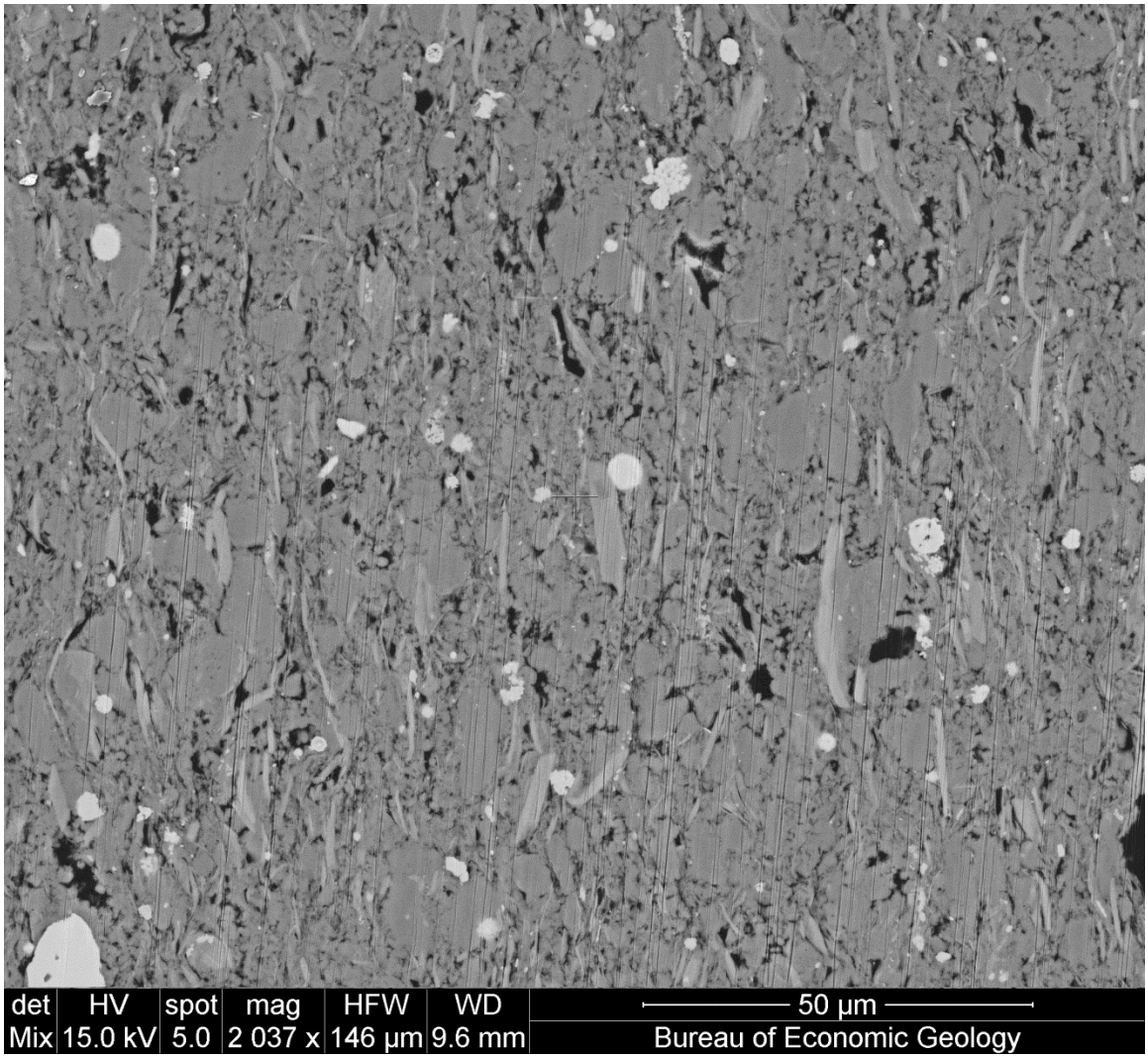

Figure 4.11 Mixed SE/BSE image on ion-milled surface within the claystone.

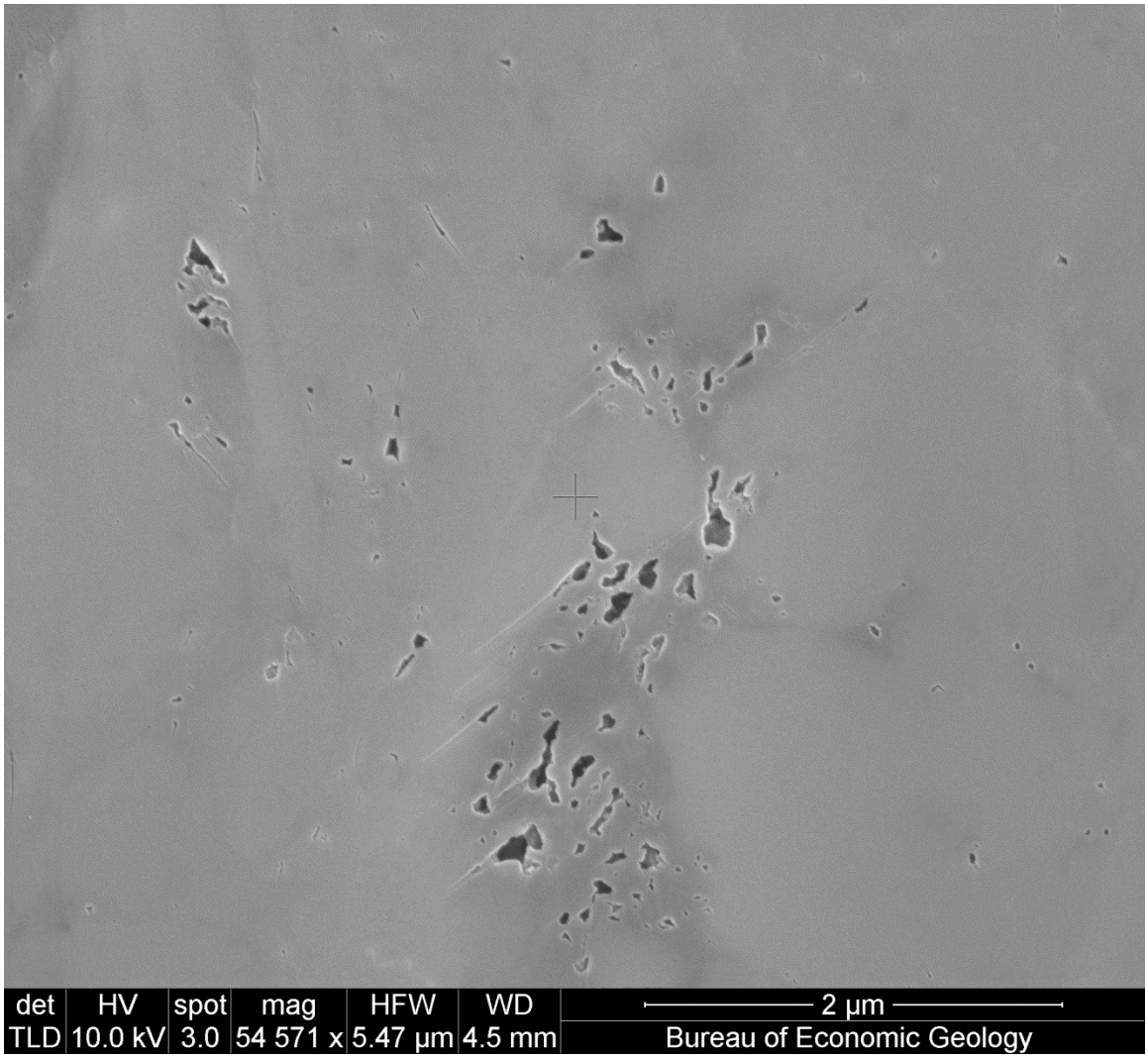

Figure 4.12 SEM image on ion-milled surface within the claystone showing organic matter pores within kerogen.

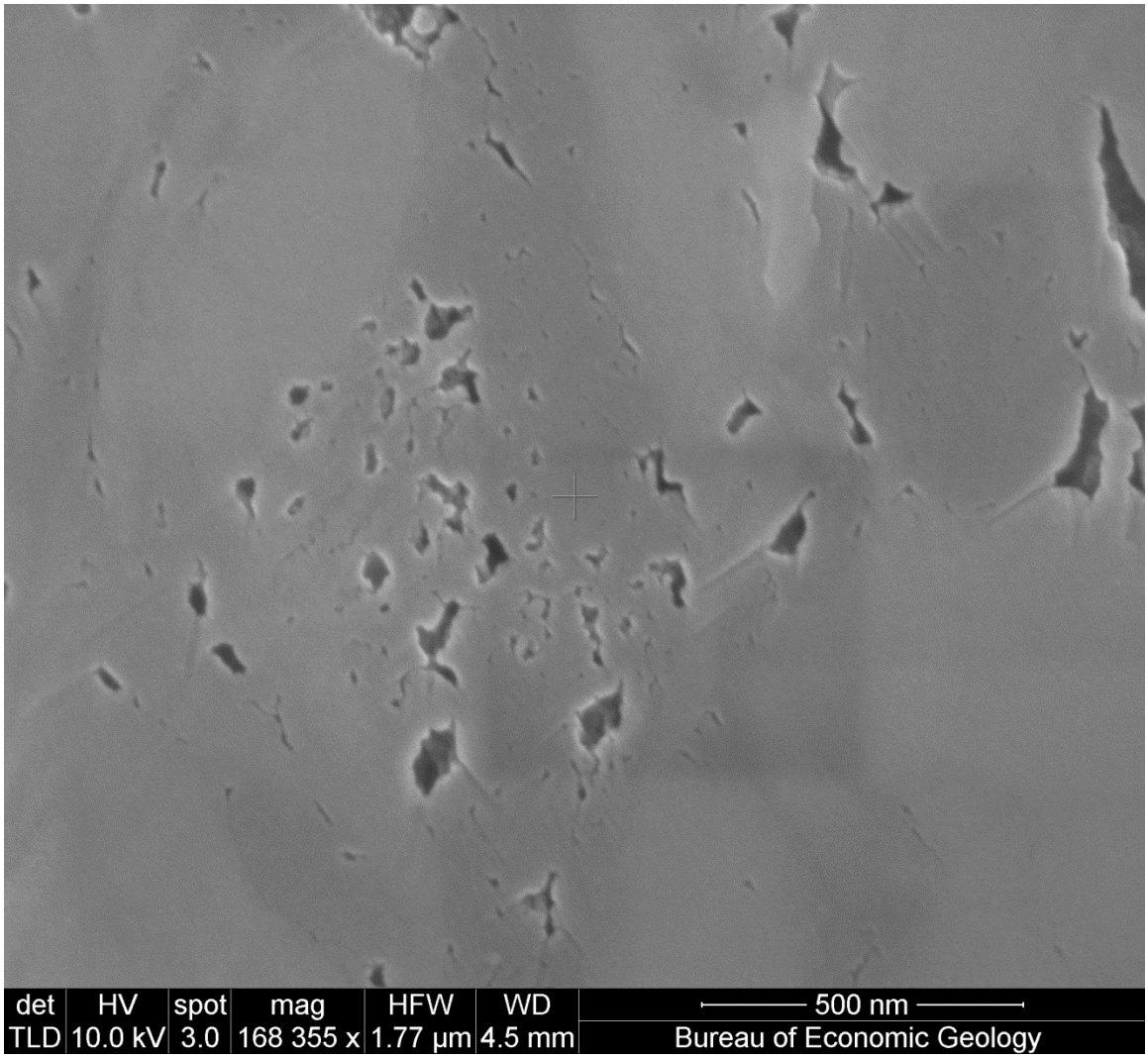

Figure 4.13 SEM image on ion-milled surface within the claystone showing organic matter pores within kerogen.

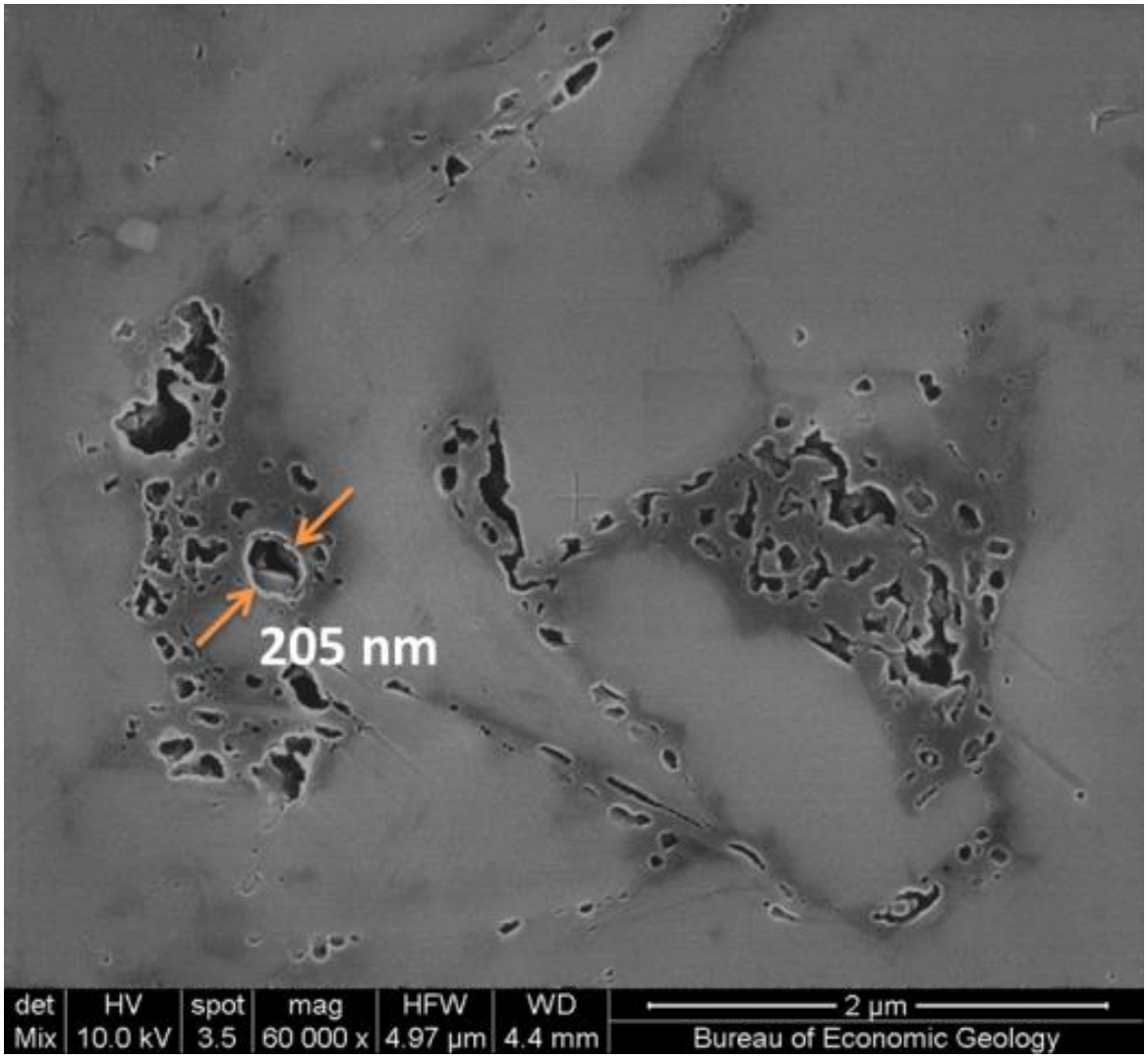

Figure 4.14 Back-Scatter Electron (BSE) image in sample 2V of organic material with nanopores approximately 205nm and smaller in diameter visible. Images produced by Patrick Smith (BEG).

4C.4: SELECTED VIEWS OF SILT-DOMINATED LITHOLOGY

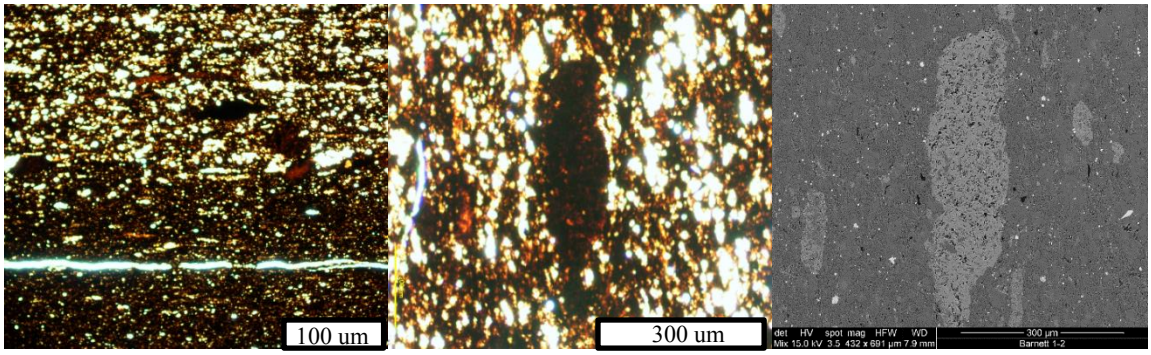

Figure 4.15 Ca-phosphate nodules with silt-sized quartz and dolomite in polished thin section 5PU-001 (6H2). Agglutinated foraminifera appear as silty aggregates with medial collapse line (Milliken et al. 2007). Left: PP view of the interface with the silty-claystone (top) and claystone (bottom). Ca-phosphate nodule and adjacent crystal grains in PP view (Middle) and SEM view (Right)

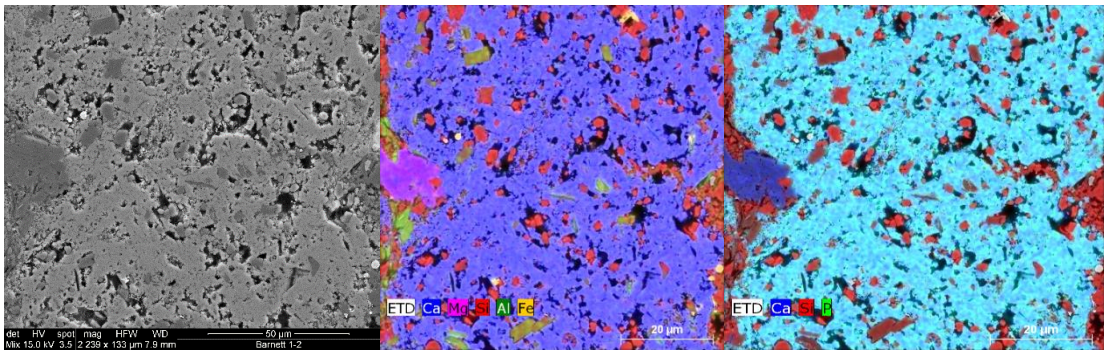

Figure 4.16 Expanded view of re-worked Ca-phosphate nodule with quartz, dolomite, and pyrite inclusions polished thin section 5PU-001 (6H2). Left: SEM image. Middle and Right: EDS map of elements for two different spectra.

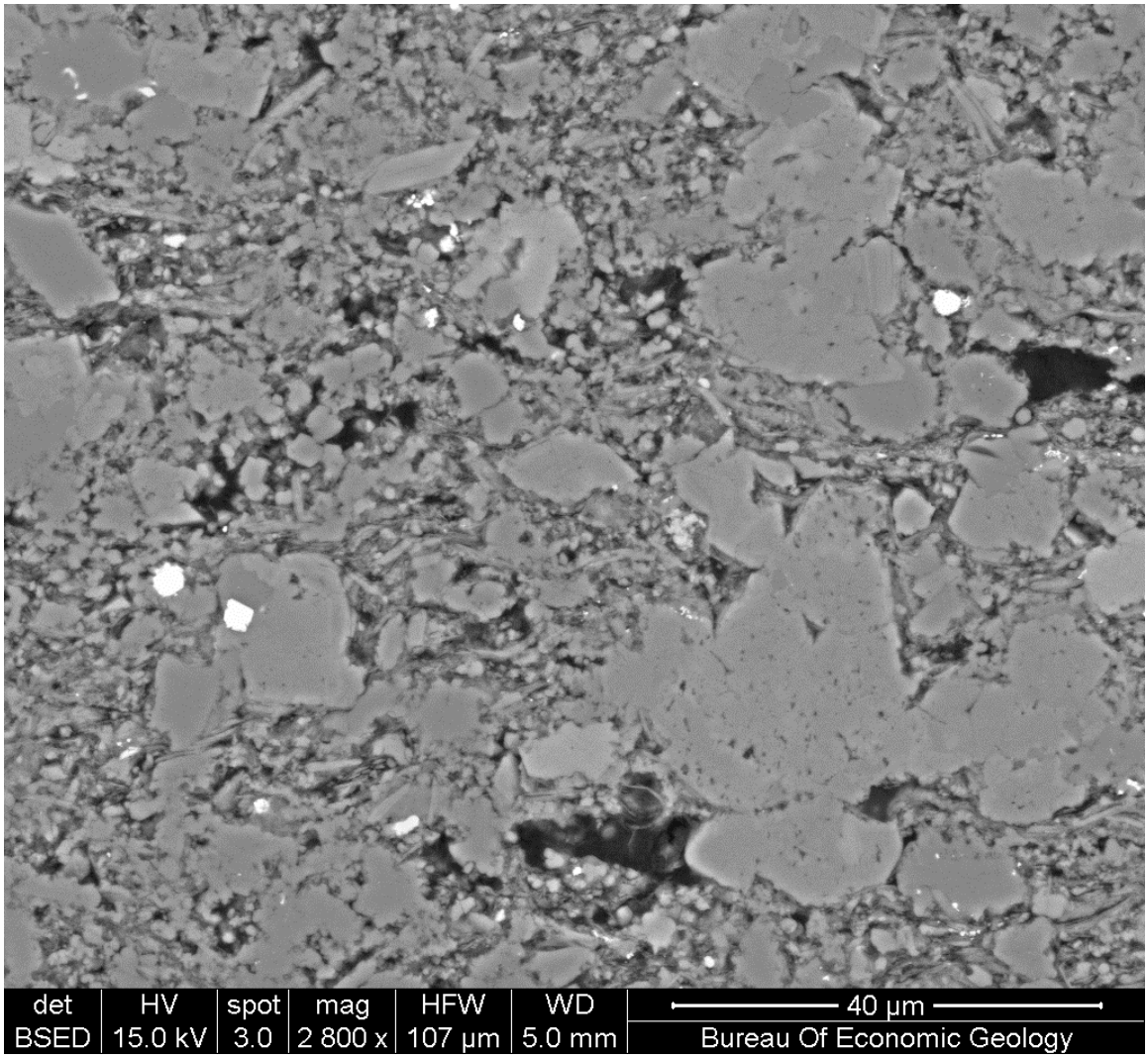

Figure 4.17 Polished thin section SEM image in silty-claystone. Bright spots are pyrite framboids, while silt-sized grains are primarily Mg-rich calcite/dolomite and quartz.

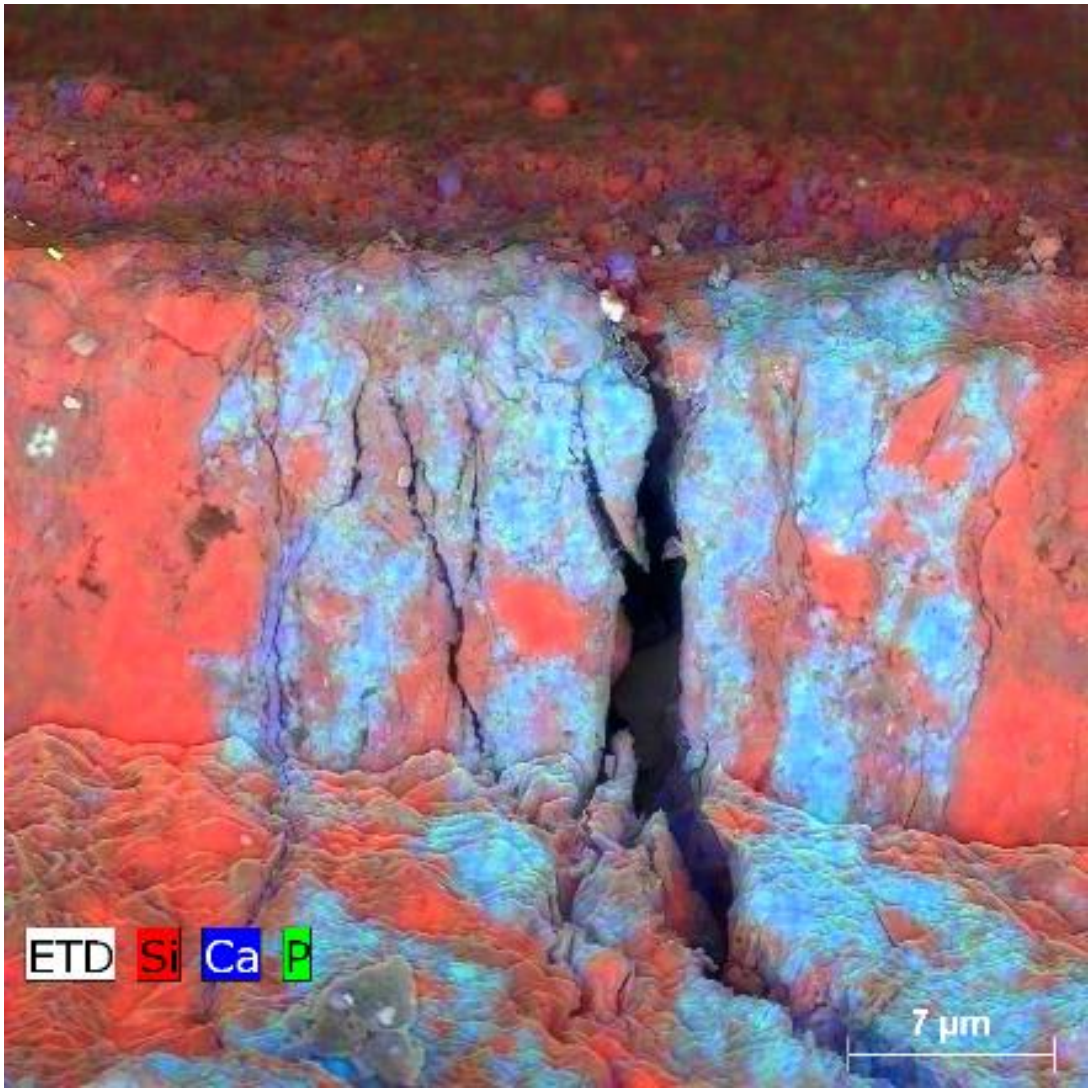

Figure 4.18 SEM-EDS image of a Ca-phosphate nodule from ion-milled surface obtained from core 6H2**.**

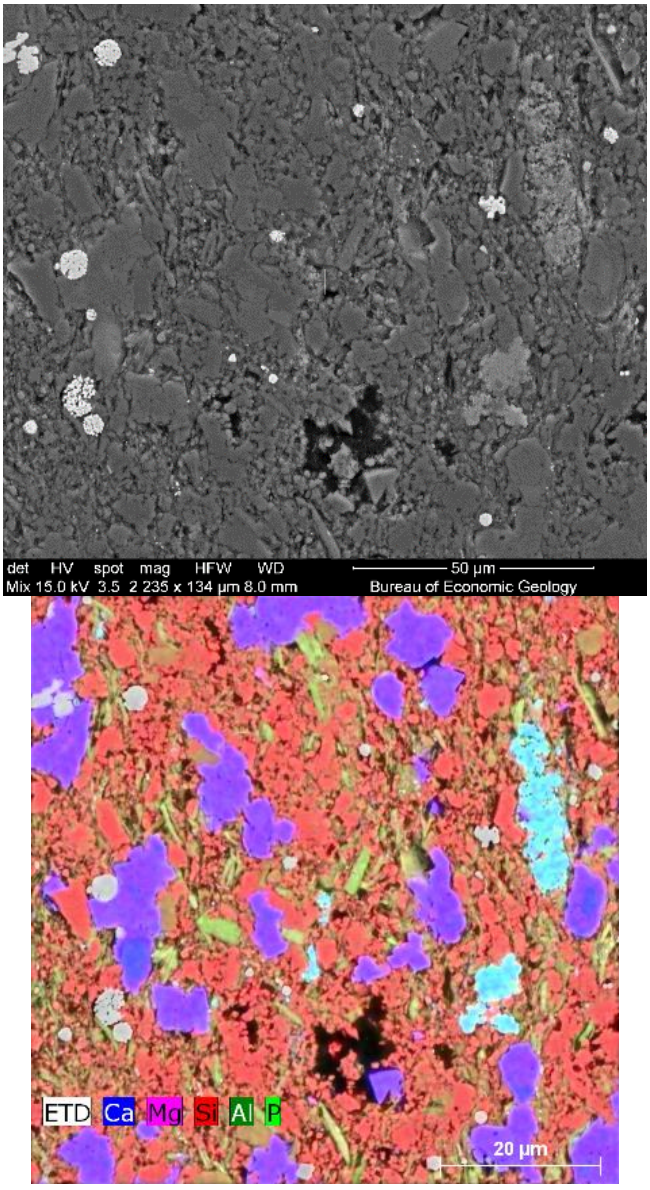

Figure 4.19 Polished thin section. Silt-sized dolomite (purple) and quartz crystals (red), with small Ca-phosphate nodules (aqua). Black material is epoxy impregnation. Top: Mixed SE/BSE image. Bottom: EDS image.

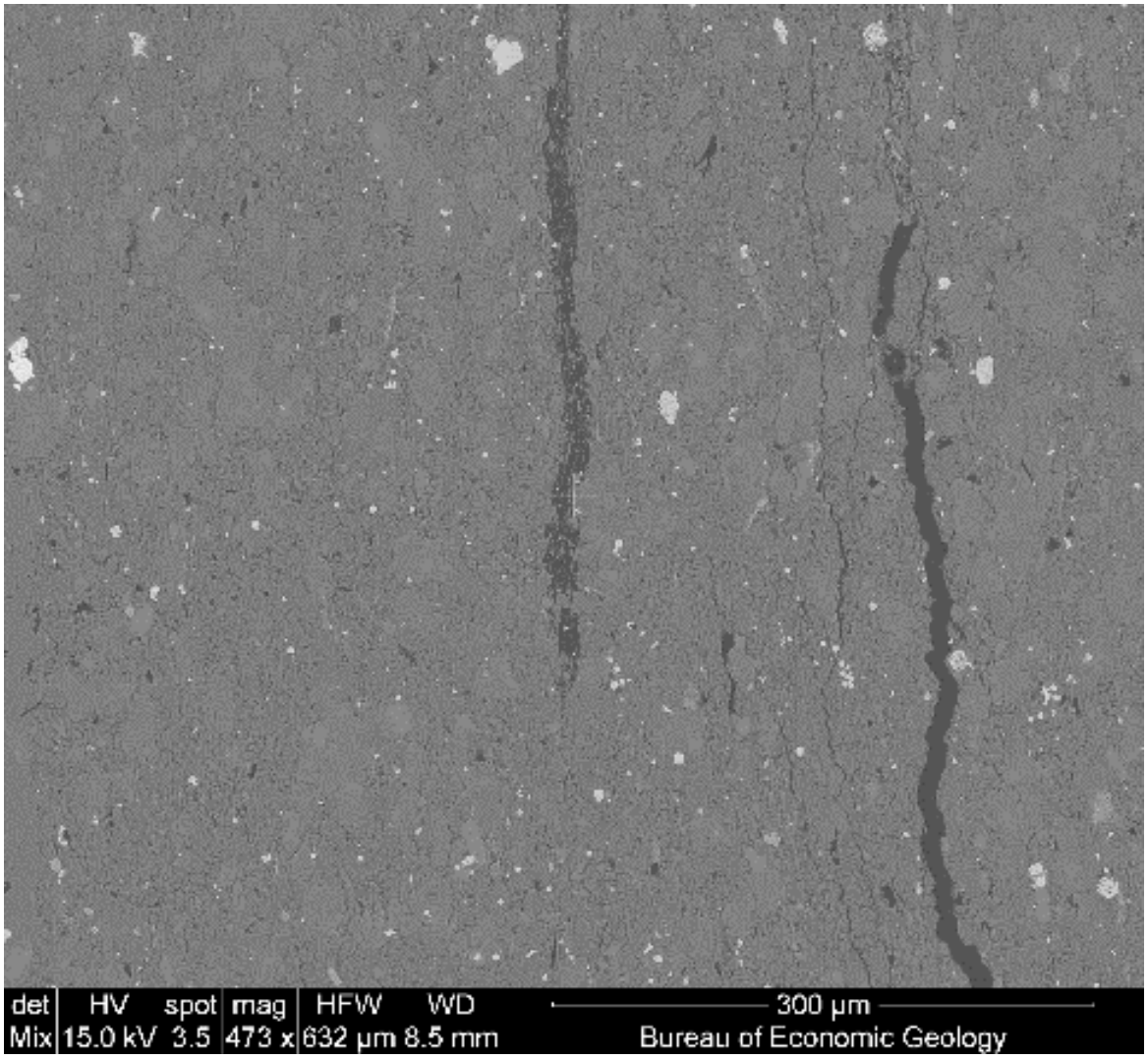

Figure 4.20 Polished thin section. Silt-sized dolomite and quartz crystals w/ stringy organic matter (center). The black string seen to the right is impregnation epoxy filling a post-coring fracture.

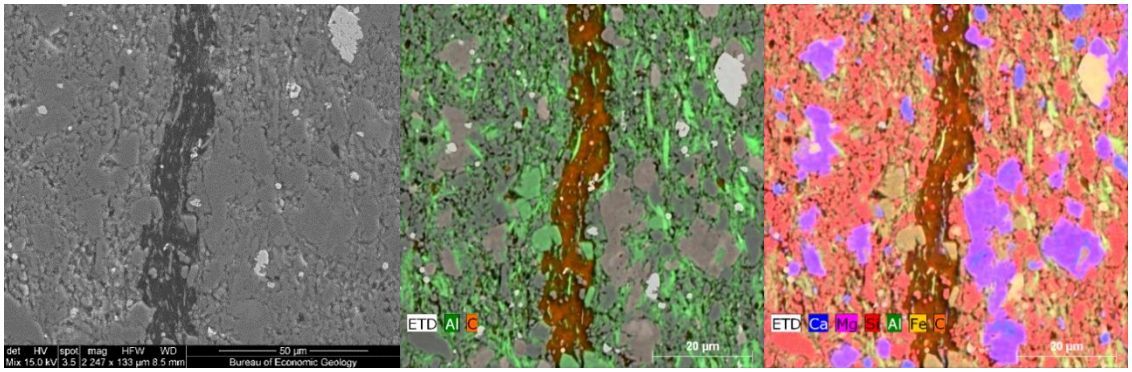

Figure 4.21 Polished thin section. Close up view of stringy organic matter in **Figure 4.20**. Silt-sized dolomite and quartz crystals w/ stringy organic matter. Clay and quartz inclusions in the organic matter suggest that it may be an "organo-mineralic aggregate" (Macquaker 1994). Left: SEM image. Middle and Right: Corresponding EDS images using two different spectra. SEM and EDS Images produced by Patrick Smith (BEG).

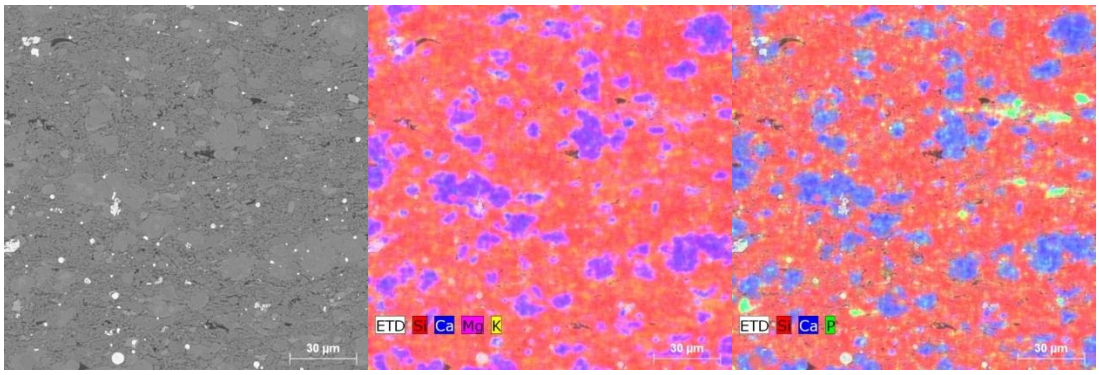

Figure 4.22 ETD (left) and EDS maps (middle, right) of silty-claystone facies. Dolomite grains show secondary overgrowth of more magnesium rich material. Sample Site: BAR6H2_E1

Appendix 4D: Numerical Pulse-Decay Simulator Details

ABSTRACT

I wrote a 1-Dimensional fully-implicit numerical simulator to analyze and forward model pulse-decay experiments conducted on core samples (both fractured and un-fractured) using gas as the pore fluid in a two-reservoir pulse-decay apparatus. My motivation was two-fold. Firstly, I desired to validate the analytical models I developed in this thesis. Secondly, I wanted to explore various initial/boundary conditions outside the scope of conventional pulse-decay analytical solutions (e.g. negative upstream pressure pulses, variable permeability/porosity in the core sample, non-uniform pressure profile in the sample, etc.). In this section, I provide a brief summary of the simulator with respect to my motivation, numerical discretization of the equations of flow, computational techniques, history matching algorithm, and experimental validation.

4D.1: MOTIVATION & UTILITY

I developed a pulse-decay simulator to validate the analytical models I developed to explain pulse-decay behavior in core samples with dual-permeability pore structure due to stratigraphically layering (**Chapter 2**) or fractures (**Chapter 3**). As a research tool, I use the simulator to replicate pulse-decay experiments ("history match") and identify the characteristic properties of core samples. In addition, I used my simulator to forward model pulse-decay experiments for the purposes of optimizing experimental duration based on expected core sample dimensions, permeability, reservoir volume, etc. In homogeneous samples, I interpret the matrix permeability and porosity. In layered samples, I interpret the porosity and permeability of each layer (**Figure 2.6**). In fractured samples, I interpret matrix permeability and porosity in addition to fracture aperture, spacing, and number of orthogonal planes (**Figure 3.6**).

The chief advantage of a numerical simulator compared to analytical techniques is the ease with which one can explore various initial/boundary conditions outside the scope of conventional pulse-decay analytical solutions. For example, conventional pulse-decay theory uses a positive pressure upstream (**Figure 1.2**). In my simulator, I can simulate the effects of a negative pressure pulse. I can also demonstrate the effects of variable permeability/porosity in the core sample (Kamath et al. 1992) or non-uniform pressure profile in the core-sample at initial conditions. In addition, fluid properties are robustly calculated as functions of pressure compared to using average values in analytical solutions. Finally, the simulator is able to correct for effects like leaks in the pulse-decay apparatus that would otherwise be difficult to accurately account for in an analytical model.

4D.2: NUMERICAL SIMULATION OVERVIEW

My numerical simulator has three segments: pre-processing (model initialization), active simulation, and post-processing (analysis) (**Figure 4.23**). The model is discretized using 1-Dimensional, point-centered approach (**Figure 4.24**) with two unknowns (matrix pressure and fracture pressure) at each interior node. The reservoir boundaries are implemented as a node at the upstream and downstream end. The simulation loop has an outer loop, which consists of time-steps $n = 1,2,3, \dots, N_t$, where n is the time-step level and N_t is the total number of steps. At each time-step, grid block pressures are implicitly calculated. The inner loops represent the iterative Newton-Rhapson process of continually updating grid-block pressures and re-calculating pressure dependent coefficients and derivatives (in the Jacobian matrix) for iteration steps $v = 1,2,3, \dots$ until convergence is satisfied. The post-processing segment entails user analysis and visualization of simulation results. All variables are defined in nomenclature **Table 4.1**.

To avoid an unwieldy number of citations in-text, I make a general citation of *Basic Applied Reservoir Simulation* by Ertekin, Abou-Kassem, and King (2001). This resource has been of immeasurable assistance, and I consulted it extensively.

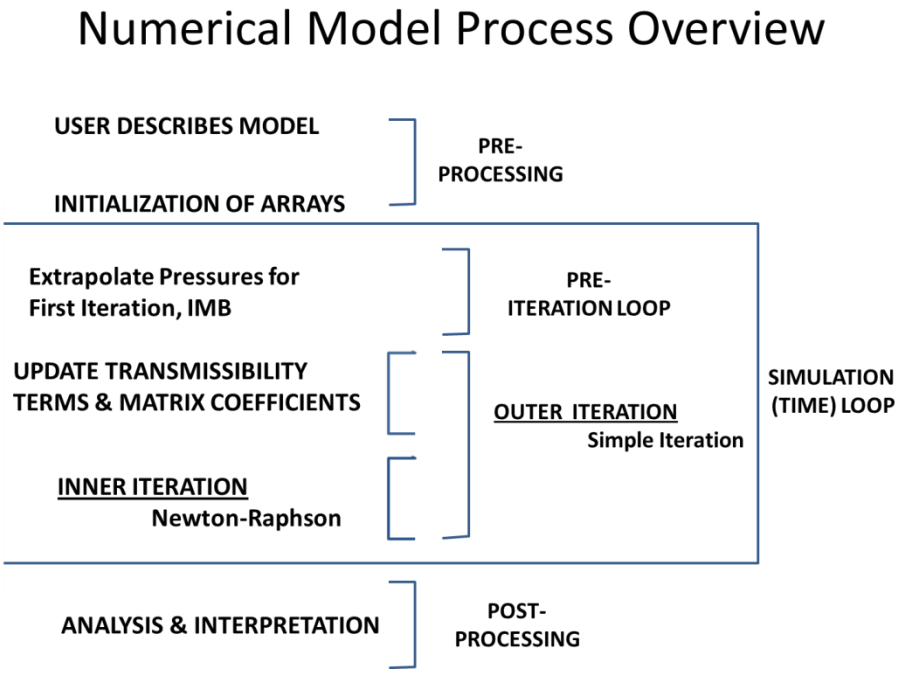

Figure 4.23 General computational schematic detailing the numerical model workflow and the relationship between inner and outer loops.

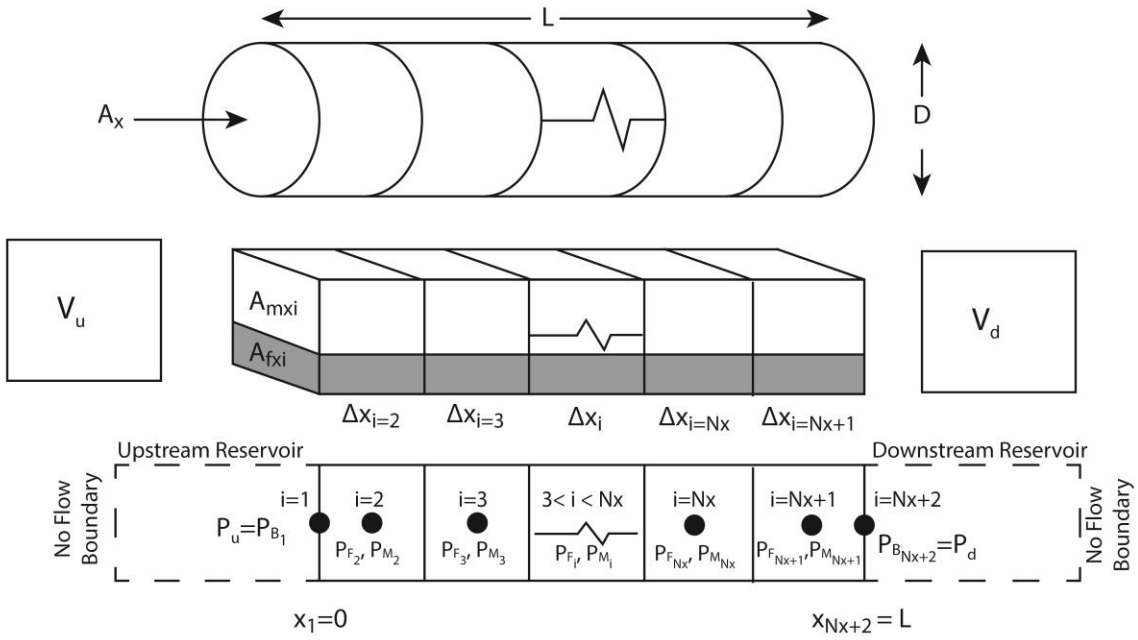

Figure 4.24 Point-centered discretization for 1-D numerical simulator of pulse-decay experiments in dual-permeability core samples. The grid index (i) refers to location of each node in the array in the x-direction. Δx_i is the length and A_{xi} is the cross-sectional area of each grid block, while A_{mxi} and A_{fxi} is the cross-sectional area of matrix and fractures in each block. The upstream and downstream reservoirs are incorporated as additional blocks upstream and downstream with no-flow external boundary conditions. Top: The cylindrical core sample. Middle: Partitioning core sample in matrix domain and fractured domain. Bottom: Discretizing the core sample into grid blocks with a central node where pressure is defined. A pressure node is defined upstream and downstream to represent reservoir pressures. Transmissibility is calculated between adjacent grid blocks in the positive ($x_{i+1/2}$) and negative ($x_{i-1/2}$) directions.

4D.3: DUAL-PERMEABILITY CODE

All variables are defined in nomenclature **Error! Reference source not found.** at the end f this Appendix. I discretize the core sample using a point-centered scheme (Figure 4.24) with a series of grid blocks identified by nodes $i = 1,2,3, \ldots, N_x + 2$, where i is the physical grid location in the x-direction for each node and N_x is the total number of grid blocks representing the core. At each interior node, there are two variables. Pressure in the fractures (P_{F_i}) and pressure in the matrix (P_{M_i}). Node $i = 1$ refers to the upstream reservoir pressure, nodes $i = 2,3, \ldots, N_x - 1$ refer to the interior grid nodes (core sample), and node $i = N_x + 2$ refers to the downstream reservoir pressure. The bulk volume (V_{b_i}) of each node is the product of grid block length (Δx_i) and cross-sectional area in the x-direction (A_x):

$$V_{b_i} = A_x \Delta x_i \qquad [4.22]$$

I used standard reservoir-simulation finite difference techniques described in (Ertekin et al. 2001) to develop a linearized implicit formulation to Equations [3.25], [3.26], and [3.27] for pressure at each node in the model. Unlike explicit formulations, implicit methods are unconditionally stable and without time-step restriction. (Ertekin et al. 2001). I use a two-point forward difference approximation for time derivatives, and the "upwind" central-difference technique for spatial derivatives. I use the gas formation volume factor (B_g) to define fluid mass in terms of the volume occupied at standard conditions (Equation [4.23]), where B_g is the ratio of fluid density, ρ, at simulated pressure and temperature conditions to a fluid density, ρ_{SC}, calculated at standard temperature and pressure conditions.

$$B_g = \frac{\rho}{\rho_{SC}} = \frac{Z_{SC} P T_{sc}}{ZTP} \qquad [4.23]$$

I list my matrix equations at each node in **Table 4.4**, where the fracture domain is represented by equations F_i, the matrix domain by equations M_i, and the reservoir boundary conditions by equations B_i. The grid equation for interior node i in the fractured domain is:

$$F_i = -\left(TXp^v_{F_i} * \left(P^v_{F_{i+1}} - P^v_{F_i}\right) - TXn^v_{F_i} * \left(P^v_{F_i} - P^v_{F_{i-1}}\right)\right) + \left(\frac{1}{\Delta t^n}\right) * \Gamma^v_{F_i} + q^v_{mf_i} = 0 \qquad [4.24]$$

And for the matrix domain:

$$M_i = -\left(TXp^v_{M_i} * \left(P^v_{M_{i+1}} - P^v_{M_i}\right) - TXn^v_{M_i} * \left(P^v_{M_i} - P^v_{M_{i-1}}\right)\right) + \left(\frac{1}{\Delta t^n}\right) * \Gamma^v_{M_i} - q^v_{mf_i} = 0 \qquad [4.25]$$

Where:

$q^v_{mf_i}$ is the inter-domain flux between the matrix and fractured pore volume:

$$q^v_{mf_i} = 2\beta_c \frac{V_{b_i}(\alpha k_{meq})}{\left(\mu^v_{g_f} B^v_{g_f} + \mu^v_{g_m} B^v_{g_f}\right)_i}\left(P^v_{F_i} - P^v_{M_i}\right) \qquad [4.26]$$

β_c is a unit conversion factor for customary (field) units, and $\mu^v_{g_f}$ and $\mu^v_{g_m}$ are gas viscosity in the fractured domain and matrix domain respectively at node i. To calculate $q^v_{mf_i}$, I multiply the bulk volume of each grid block (V_{b_i}) by the shape-factor equivalent matrix permeability product (αk_{meq}) that I calculated for the entire bulk core volume. When matrix permeability is isotropic ($k_{meq} = k_m = k_{mx} = k_{my} = k_{mz}$), the value of αk_{meq} is given by Equation [4.27], where $S_{fx,y,z}$, $w_{fx,y,z}$, are fracture spacing, and aperture, and $N_{FX,Y,Z}$ is the number of fractures in each Cartesian direction (**Figure 3.5**). Refer to Appendix 4D.4 for additional details on the derivation of α.

$$\alpha k_{meq} = 4k_m \left[\left(\frac{N_{FX}}{(N_{FX}+1)(S_{fx}-w_{fx})}\right)^2 + \left(\frac{N_{FY}}{(N_{FY}+1)(S_{fy}-w_{fy})}\right)^2 + \left(\frac{N_{FZ}}{(N_{FZ}+1)(S_{fz}-w_{fz})}\right)^2\right] \qquad [4.27]$$

Γ^v_{F,M,B_i} is the mass accumulation term between iteration level v and time-level n in the fractures (Equation [4.28]) and matrix (Equation [4.29]). α_c is a unit conversion factor for

customary (field) units, Φ_{fi} is the fraction of fracture pore volume contained in grid block i to the bulk volume of grid block i. Φ_{mi} is the fraction of matrix pore volume to bulk volume in each grid block.

$$\Gamma_{F\,i}^{v} = \frac{V_{b_i}\Phi_{fi}}{\alpha_c}\left(\frac{1}{B_{g_f}^{v}} - \frac{1}{B_{g_f}^{n}}\right)_i \quad [4.28]$$

$$\Gamma_{M\,i}^{v} = \frac{V_{b_i}\Phi_{mi}}{\alpha_c}\left(\frac{1}{B_{gm}^{v}} - \frac{1}{B_{gm}^{n}}\right)_i \quad [4.29]$$

TXp_{F,M_i}^{v} is transmissibility in the positive x-direction (evaluated at $i+\frac{1}{2}$) for the fractures (Equation [4.30]), matrix (Equation [4.31]). TXn_{F,M_i}^{v} is transmissibility in the negative x-direction (evaluated at $i-\frac{1}{2}$) for the fractures (Equation [4.32]) and matrix (Equation [4.33]).

$$TXp_{F\,i}^{v} = 2\beta_c \frac{k_{fHx_i}A_{x_i}k_{fHx_{i+1}}A_{x_{i+1}}}{\mu_{f_{g_i}}B_{f_{g_i}}k_{fHx_{i+1}}A_{fx_{i+1}}\Delta x_i + \mu_{f_{g_{i+1}}}B_{f_{g_{i+1}}}k_{fx_i}A_{fx_i}\Delta x_{i+1}} \quad [4.30]$$

$$TXp_{M\,i}^{v} = 2\beta_c \frac{k_{mx_i}A_{mx_i}k_{mx_{i+1}}A_{mx_{i+1}}}{\mu_{m_{g_i}}B_{m_{g_i}}k_{mx_{i+1}}A_{mx_{i+1}}\Delta x_i + \mu_{m_{g_{i+1}}}B_{m_{g_{i+1}}}k_{mx_i}A_{mx_i}\Delta x_{i+1}} \quad [4.31]$$

$$TXn_{F\,i}^{v} = 2\beta_c \frac{k_{fHx_i}A_{x_i}k_{fHx_{i-1}}A_{x_{i-1}}}{\mu_{f_{g_i}}B_{f_{g_i}}k_{fHx_{i-1}}A_{fx_{i-1}}\Delta x_i + \mu_{f_{g_{i-1}}}B_{f_{g_{i-1}}}k_{fHx_i}A_{fx_i}\Delta x_{i-1}} \quad [4.32]$$

$$TXn_{M\,i}^{v} = 2\beta_c \frac{k_{mx_i}A_{mx_i}k_{mx_{i+1}}A_{mx_{i+1}}}{\mu_{m_{g_i}}B_{m_{g_i}}k_{x_{i-1}}A_{mx_{i-1}}\Delta x_i + \mu_{m_{g_{i-1}}}B_{m_{g_{i-1}}}k_{mx_i}A_{mx_i}\Delta x_{i-1}} \quad [4.33]$$

The fracture permeability appearing in the transmissibility terms is defined in terms of effective horizontal permeability k_{fHx} (Equation [4.34]). A_x is the cross-sectional area in the x-direction of each grid block. $k_{f_{sandwich}}$ and $A_{f_{sandwich}}$ is the permeability and cross-sectional area of fractures in the X-Y plane ("sandwich" orientation), and $k_{f_{fin}}$ and $A_{f_{fin}}$ is the permeability and cross-sectional area of fractures in the Y-Z plane ("fin" orientation) (**Figure 3.5**).

$$k_{fHx} = \frac{k_{f_{sandwich}}A_{f_{sandwich}} + k_{f_{fin}}A_{f_{fin}}}{A_x} \quad [4.34]$$

A_{fx_i} is the total cross-sectional area of the fractured domain in the x-direction for each element. It is a function of fracture aperture, spacing, and the number of orthogonal fracture planes (**Table 3.2**). k_{mx_i} is the matrix permeability in the x-direction of each element. A_{mx_i} is the cross-sectional area in the x-direction between two continuous matrix blocks and equals the bulk cross-sectional area minus the area of fractures (Equation [4.37]):

$$A_{mx_i} = \left(A_{x_i} - A_{fx}\right) \quad [4.35]$$

The reservoirs are represented as grid blocks with zero width ($\Delta x_1, \Delta x_{N_x+2} = 0$) and pore volume equal to the reservoir volume ($V_{res_1} = V_u, V_{res_{N_x+2}} = V_d$). The mass accumulation term for the upstream reservoir ($\Gamma^v_{B\,1}$) is Equation [4.36] and for the downstream reservoir ($\Gamma^v_{B\,N_x+2}$) is Equation [4.37]. The vessels are rigid and in continuity with the fractured and matrix pore volume.

$$\Gamma^v_{B\,1} = \frac{V_u}{\alpha_c}\left(\frac{1}{B^v_{g_B}} - \frac{1}{B^n_{g_B}}\right)_1 \quad [4.36]$$

$$\Gamma^v_{B\,N_x+2} = \frac{V_d}{\alpha_c}\left(\frac{1}{B^v_{g_B}} - \frac{1}{B^n_{g_B}}\right)_{N_x+2} \quad [4.37]$$

The upstream boundary has transmissibility in the positive direction to the fractures $TXp^v_{BF_1}$(Equation [4.38]) and to the matrix $TXp^v_{BM_1}$ (Equation [4.39]). Transmissibility in the negative direction is zero (no flow boundary).

$$TXp^v_{BF_1} = 2\beta_c \frac{k_{fHx_1} A_{x_1} k_{fHx_2} A_{x_2}}{\mu_{f g_2} B_{f g_2} k_{fHx_1} A_{x_1} \Delta x_2} \quad [4.38]$$

$$TXp^v_{BM_1} = 2\beta_c \frac{k_{mx_1} A_{mx_1} k_{mx_2} A_{mx_2}}{\mu_{m g_2} B_{m g_2} k_{mx_1} A_{mx_1} \Delta x_2} \quad [4.39]$$

The downstream boundary has transmissibility in the negative direction to the fractures $TXn^v_{BF_{N_x+2}}$(Equation [4.40]) and to the matrix $TXn^v_{BM_{N_x+2}}$ (Equation [4.41]). Transmissibility in the positive direction is zero (no flow boundary).

$$TXn^{v}_{BF_{N_x+2}} = 2\beta_c \frac{k_{fHx_{N_x+2}} A_{x_{N_x+2}} k_{fHx_{N_x+1}} A_{x_{N_x+1}}}{\mu_{fg_{N_x+1}} B_{fg_{N_x+1}} k_{fHx_{N_x+2}} A_{x_{N_x+2}} \Delta x_{N_x+1}}} \quad [4.40]$$

$$TXn^{v}_{BM_{N_x+2}} = 2\beta_c \frac{k_{mx_{N_x+2}} A_{mx_{N_x+2}} k_{mx_{N_x+1}} A_{mx_{N_x+1}}}{\mu_{mg_{N_x+1}} B_{mg_{N_x+1}} k_{mx_{N_x+2}} A_{mx_{N_x+2}} \Delta x_{N_x+1}}} \quad [4.41]$$

$q^{v}_{Leak_i}$ is the sink-term for a gas leak in one of the reservoirs (Equation [4.42]), where B_g is evaluated at the extrapolated reservoir pressure P^{n+1}_{Leak} (Equation [4.43]) due to it leaking at a rate of $\frac{dP_{res}}{dt}$.

$$q^{v}_{Leak_i} = \frac{V_{res_i}}{\alpha_c}\left(\frac{1}{B_g(P^{n+1}_{Leak_i})} - \frac{1}{B^n_g}\right)_i \quad [4.42]$$

$$P^{n+1}_{Leak_i} = P^{n}_{res_i} + \Delta t^n \frac{dP_{res_i}}{dt} \quad [4.43]$$

I linearized the flow equations by lagging the pressure dependent terms (evaluating them using pressures at iteration level v) when solving for grid pressures at iteration level $v+1$. I combine the equations listed in **Table 4.4** into a single system of equations ($\mathcal{F}(\vec{P}^v, \vec{P}^n)$). I order the equations using the indicial index $\hbar_i$, where subscript i refers to the x-location of each node. The reservoirs correspond to $\hbar_1 = 1$ and $\hbar_{N_x+2} = 2N_x + 2$, the fractured domain to ($\hbar_{2\leq i\leq N_x+1} = 2i-2$), and the matrix domain to ($\hbar_{2\leq i\leq N_x+1} = 2i-1$) (**Table 4.4**). Matrix $\mathcal{F}(\vec{P}^v, \vec{P}^n)$ incorporates information at n time-level and v iteration level. The Jacobian matrix (J^v) of $\mathcal{F}(\vec{P}^v, \vec{P}^n)$ is defined by matrix Equation [4.48], and the non-zero entries listed in Equations [4.49]– [4.65]. Derivatives appearing in the Jacobian were determined numerically using the two-point central difference method (Equation [4.44]), where ε_{Der} is a small step in the function argument x.

$$F'(x) = \frac{F(x+\varepsilon_{Der}) - F(x-\varepsilon_{Der})}{2\varepsilon_{Der}} \quad [4.44]$$

I inverted the Jacobian matrix using L-U decomposition and used Newton-Rhapson iteration (Equation [4.45]) to find the node pressures at $\vec{P}^{v+1}$ until the solution converged (Equation [4.46]).

$$\vec{P}^{v+1} = -[J^v]^{-1}\left[\mathcal{F}\left(\vec{P}^v, \vec{P}^n\right)\right] + \vec{P}^v \quad [4.45]$$

I defined convergence in terms of the maximum relative pressure change in the solution vector $\vec{P}$ between iterations $v+1$ and v, where ε is a small number:

$$\left\|\vec{P}^{v+1} - \vec{P}^v\right\|_{oo} \leq \varepsilon_{Tol} * \left\|\vec{P}^v\right\|_{oo} \quad [4.46]$$

To speed up convergence, I linearly extrapolated pressure using the $n-1$ and n timelevels to estimate transmissibility values for the initial iteration:

$$\vec{P}^{v=0} = \frac{\vec{P}^n - \vec{P}^{n-1}}{t^n - t^{n-1}}(t^{n+1} - t^n) \quad [4.47]$$

Table 4.4 Grid Equations for Fractured Domain (F_i), Matrix Domain (M_i), and Reservoir Boundaries (B_i). $\aleph_i$ is the index for when the grid equations are combined into a single matrix.

$\aleph_i$	Grid Equations: F_i, M_i	Grid Region
1	$B_1 = -\left(TXp^v_{B_1F} * \left(P^v_{F_2} - P^v_{B_1}\right)\right) - \left(TXp^v_{B_1M} * \left(P^v_{M_2} - P^v_{B_1}\right)\right) + \left(\frac{1}{\Delta t^n}\right) * \Gamma^v_{B_1} - q^v_{Leak_i}$	Upstream Reservoir: $i = 1$
2	$F_2 = -\left(TXp^v_{F_2} * \left(P^v_{F_3} - P^v_{F_2}\right) - TXn^v_{F_2} * \left(P^v_{F_2} - P^v_{B_1}\right)\right) + \left(\frac{1}{\Delta t^n}\right) * \Gamma^v_{F_2} + q^v_{mf_2}$	
3	$M_2 = -(TXp^v_{M_2} * (P^v_{M_3} - P^v_{M_2}) - TXn^v_{M_2} * (P^v_{M_2} - P^v_{B_1})) + \left(\frac{1}{\Delta t^n}\right) * \Gamma^v_{M_2} - q^v_{mf_2}$	
⋮	⋮	
$2i-2$	$F_i = -\left(TXp^v_{F_i} * \left(P^v_{F_{i+1}} - P^v_{F_i}\right) - TXn^v_{F_i} * \left(P^v_{F_i} - P^v_{F_{i-1}}\right)\right) + \left(\frac{1}{\Delta t^n}\right) * \Gamma^v_{F_i} + q^v_{mf_i}$	Core Sample Interior: $i =$ $[2, \ldots, N_x + 1]$
$2i-1$	$M_i = -(TXp^v_{M_i} * (P^v_{M_{i+1}} - P^v_{M_i}) - TXn^v_{M_i} * (P^v_{M_i} - P^v_{M_{i-1}})) + \left(\frac{1}{\Delta t^n}\right) * \Gamma^v_{M_i} - q^v_{mf_i}$	
⋮	⋮	
$2N_x$	$M_{N_x+1} = -(TXp^v_{M_{N_x+1}} * (P^v_{B_{N_x+2}} - P^v_{M_{N_x+1}}) - TXn^v_{M_{N_x+1}} * (P^v_{M_{N_x+1}} - P^v_{M_{N_x}})) + \left(\frac{1}{\Delta t^n}\right) * \Gamma^v_{M_{N_x+1}} - q^v_{mf_{N_x+1}}$	
$2N_x+1$	$F_{N_x+1} = -\left(TXp^v_{F_{N_x+1}} * \left(P^v_{B_{N_x+2}} - P^v_{F_{N_x+1}}\right) - TXn^v_{F_{N_x+1}} * \left(P^v_{F_{N_x+1}} - P^v_{F_{N_x}}\right)\right) + \left(\frac{1}{\Delta t^n}\right) * \Gamma^v_{F_{N_x+1}} + q^v_{mf_{N_x+1}}$	
$2N_x+2$	$B_{N_x+2} = \left(TXn^v_{BF_{N_x+2}} * \left(P^v_{B_{N_x+2}} - P^v_{F_{N_x+1}}\right)\right) + \left(TXn^v_{BM_{N_x+2}} * \left(P^v_{B_{N_x+2}} - P^v_{M_{N_x+1}}\right)\right) + \left(\frac{1}{\Delta t^n}\right) * \Gamma^v_{B_{N_x+2}} - q^v_{Leak_i}$	Downstream Reservoir: $i = N_x + 2$

$$J^v = [\mathcal{F}]^{-1} = \quad [4.48]$$

$$
\begin{bmatrix}
\frac{dB_1}{dP_{B_1}} & \frac{dB_1}{dP_{F_2}} & \frac{dB_1}{dP_{M_2}} & & & & & & & & & & \\
\frac{dF_2}{dP_{B_1}} & \frac{dF_2}{dP_{F_2}} & \frac{dF_2}{dP_{M_2}} & \frac{dF_2}{dP_{F_3}} & & & & & & & & & \\
\frac{dM_2}{dP_{B_1}} & \frac{dM_2}{dP_{F_2}} & \frac{dM_2}{dP_{M_2}} & & \frac{dM_2}{dP_{M_3}} & & & & & & & & \\
 & \frac{dF_3}{dP_{F_2}} & & \frac{dF_3}{dP_{F_3}} & \frac{dF_3}{dP_{M_3}} & \frac{dF_3}{dP_{F_4}} & & & & & & & \\
 & & \frac{dM_3}{dP_{M_2}} & \frac{dM_3}{dP_{F_3}} & \frac{dM_3}{dP_{M_3}} & & \frac{dM_3}{dP_{M_4}} & & & & & & \\
 & & & \ddots & & \ddots & & \ddots & & & & & \\
 & & & & \frac{dF_i}{dP_{F_{i-1}}} & & \frac{dF_i}{dP_{F_i}} & \frac{dF_i}{dP_{M_i}} & \frac{dF_i}{dP_{F_{i+1}}} & & & & \\
 & & & & & \frac{dM_i}{dP_{M_{i-1}}} & \frac{dM_i}{dP_{F_i}} & \frac{dM_i}{dP_{M_i}} & & \frac{dM_i}{dP_{M_{i+1}}} & & & \\
 & & & & & \ddots & & & & & \ddots & & \\
 & & & & & & \frac{dF_{N_x}}{dP_{F_{N_x-1}}} & & \frac{dF_{N_x}}{dP_{F_{N_x}}} & \frac{dF_{N_x}}{dP_{M_{N_x}}} & \frac{dF_{N_x}}{dP_{F_{N_x+1}}} & & \\
 & & & & & & & \frac{dM_{N_x}}{dP_{M_{N_x-1}}} & \frac{dM_{N_x}}{dP_{F_{N_x}}} & \frac{dM_{N_x}}{dP_{M_{N_x}}} & & \frac{dM_{N_x}}{dP_{M_{N_x+1}}} & \\
 & & & & & & & & \frac{dF_{N_x+1}}{dP_{F_{N_x+1}}} & & \frac{dF_{N_x+1}}{dP_{F_{N_x+1}}} & \frac{dF_{N_x+1}}{dP_{M_{N_x+1}}} & \frac{dF_{N_x+1}}{dP_{B_{N_x+2}}} \\
 & & & & & & & & & \frac{dM_{N_x+1}}{dP_{M_{N_x}}} & \frac{dM_{N_x+1}}{dP_{F_{N_x+1}}} & \frac{dM_{N_x+1}}{dP_{M_{N_x+1}}} & \frac{dM_{N_x+1}}{dP_{B_{N_x+2}}} \\
 & & & & & & & & & & \frac{dB_{N_x+2}}{dP_{F_{N_x+1}}} & \frac{dB_{N_x+2}}{dP_{M_{N_x+1}}} & \frac{dB_{N_x+2}}{dP_{B_{N_x+2}}}
\end{bmatrix}
$$

For the Upstream Reservoir Boundary Node ($i = 1$):

$$\frac{dB_1}{dP_{B_1}} = TXp^v_{BF_1} - \frac{dTXp^v_{BF_i}}{dP_{F_i}} * \left(P^v_{F_2} - P^v_{B_1}\right) + TXp^v_{BM_1} - \frac{dTXp^v_{BM_1}}{dP_{B_1}} * \left(P^v_{M_2} - P^v_{B_1}\right) + \left(\frac{1}{\Delta t^n}\right) * \frac{d\Gamma^v_{B_1}}{dP_{B_1}} \quad [4.49]$$

$$\frac{dB_1}{dP_{F_2}} = -TXp^v_{BF_1} - \frac{dTXp^v_{BF_1}}{dP_{F_2}} * \left(P^v_{F_2} - P^v_{F_1}\right) \quad [4.50]$$

$$\frac{dB_1}{dP_{F_0}} = 0 \quad [4.51]$$

$$\frac{dB_1}{dP_{M_2}} = -TXp^v_{BM_i} - \frac{dTXp^v_{BM_1}}{dP_{M_2}} * \left(P^v_{M_2} - P^v_{B_1}\right) \quad [4.52]$$

For the Interior Nodes ($i = 2,3,\dots,N_x + 1$), note that $P_{F_1} = P_{M_1} = P_{B_1}$ and $P_{F_{N_x+2}} = P_{M_{N_x+2}} = P_{B_{N_x+2}}$.

$$\frac{dF_i}{dP_{F_i}} = TXp^v_{F_i} - \frac{dTXp^v_{F_i}}{dP_{F_i}} * \left(P^v_{F\,i+1} - P^v_{F\,i}\right) + TXn^v_{F_i} + \frac{dTXn^v_{F_i}}{dP_{F_i}} * \left(P^v_{F\,i} - P^v_{F\,i-1}\right) + \left(\frac{1}{\Delta t^n}\right) * \frac{d\Gamma^v_{F_i}}{dP_{F_i}} + \frac{dq^v_{mf_i}}{dP_{F_i}} \quad [4.53]$$

$$\frac{dF_i}{dP_{F_{i+1}}} = -TXp^v_{F_i} - \frac{dTXp^v_{F_i}}{dP_{F_{i+1}}} * \left(P^v_{F\,i+1} - P^v_{F\,i}\right) \quad [4.54]$$

$$\frac{dF_i}{dP_{F_{i-1}}} = -TXn^v_{F_i} + \frac{dTXn^v_{F_i}}{dP_{F_{i-1}}} * \left(P^v_{F\,i} - P^v_{F\,i-1}\right) \quad [4.55]$$

$$\frac{dF_i}{dP_{M_i}} = \frac{dq^v_{mf_i}}{dP_{M_i}} \quad [4.56]$$

$$\frac{dM_i}{dP_{M_i}} = TXp^v_{M_i} - \frac{dTXp^v_{M_i}}{dP_{M_i}} * \left(P^v_{M_{i+1}} - P^v_{M_i}\right) + TXn^v_{M_i} + \frac{dTXn^v_{M_i}}{dP_{M_i}} * \left(P^v_{M_i} - P^v_{M_{i-1}}\right) + \left(\frac{1}{\Delta t^n}\right) * \frac{d\Gamma^v_{M_i}}{dP_{M_i}} - \frac{dq^v_{mf_i}}{dP_{M_i}} \quad [4.57]$$

$$\frac{dM_i}{dP_{M_{i+1}}} = -TXp^v_{M_i} - \frac{dTXp^v_{M_i}}{dP_{M_{i+1}}} * \left(P^v_{M_{i+1}} - P^v_{M_i}\right) \quad [4.58]$$

$$\frac{dM_i}{dP_{M_{i-1}}} = -TXn^v_{M_i} + \frac{dTXn^v_{M_i}}{dP_{M_{i-1}}} * \left(P^v_{M_i} - P^v_{M_{i-1}}\right) \quad [4.59]$$

$$\frac{dM_i}{dP_{F_i}} = -\frac{dq^v_{mf_i}}{dP_{F_i}} \quad [4.60]$$

For the Downstream Reservoir Boundary Node ($i = N_x + 2$):

$$\frac{dB_{N_x+2}}{dP_{B_{N_x+2}}} = \left(TXn^v_{BF_{N_x+2}} * \left(P^v_{B\,N_x+2} - P^v_{F\,N_x+1}\right)\right) + \left(TXn^v_{M_{N_x+2}} * \left(P^v_{B\,N_x+2} - P^v_{M_{N_x+1}}\right)\right) + \left(\frac{1}{\Delta t^n}\right) * \Gamma^v_{B\,N_x+2} - q^v_{Leak_i} \quad [4.61]$$

$$\frac{dB_{N_x+2}}{dP_{B_{N_x+2}}} = TXn^v_{BF_{N_x+2}} - \frac{dTXn^v_{BF_{N_x+2}}}{dP_{B_{N_x+2}}} * \left(P^v_{B\,N_x+2} - P^v_{F\,N_x+1}\right) + TXn^v_{BM_{N_x+2}} - \frac{dTXn^v_{BM_{N_x+2}}}{dP_{B_{N_x+2}}} * \left(P^v_{B\,N_x+2} - P^v_{M\,N_x+1}\right) + \left(\frac{1}{\Delta t^n}\right) * \frac{d\Gamma^v_{B_{N_x+2}}}{dP_{B_{N_x+2}}} \quad [4.62]$$

$$\frac{dB_{N_x+2}}{dP_{B_{N_x+3}}} = 0 \quad [4.63]$$

$$\frac{dB_{N_x+2}}{dP_{F_{N_x+1}}} = -TXn^v_{F_{N_x+2}} + \frac{dTXn^v_{BF_{N_x+2}}}{dP_{F_{N_x+1}}} * \left(P^v_{B\,N_x+2} - P^v_{F\,N_x+1}\right) \quad [4.64]$$

$$\frac{dB_{N_x+2}}{dP_{M_{N_x+1}}} = -TXn^v_{BM_{N_x+2}} + \frac{dTXn^v_{BM_{N_x+2}}}{dP_{M_{N_x+1}}} * \left(P^v_{B\,N_x+2} - P^v_{M\,N_x+1}\right) \quad [4.65]$$

4D.4: SHAPE FACTOR

Fluid transfer between two porous domains can be expressed in terms of shape factor and the average pressure differential between the two domains. This is advantageous because it simplifies fluid exchange that may be occurring in 1, 2, or 3 dimensions into an equivalent 1-D problem. I use a matrix shape factor in my analytical dual-permeability models in addition to my numerical pulse-decay simulator. This section details the derivation of shape factor (α).

Consider a porous medium consisting of matrix blocks with dimensions $h_{mx}\ x\ h_{my}\ x\ h_{mz}$ separated by a number of planar fractures in the x- (N_{FX}), y- (N_{FY}), and z- (N_{FZ}) directions (**Figure 3.5**). The bulk volume of this system is:

$$V_B = (N_{FX}+1)(N_{FY}+1)(N_{FZ}+1)h_{mx}h_{my}h_{mz} \quad [4.66]$$

The total mass-flow rate in the x-direction (q_{eqX}), y-direction (q_{eqY}), and z-direction (q_{eqZ}) between the matrix and fractured domains is:

$$q_{eqX} = -\rho\frac{k_{mx}A_{meqX}}{\mu L_{meqX}}(\bar{P}_m - \bar{P}_f) \quad [4.67]$$

$$q_{eqY} = -\rho\frac{k_{my}A_{meqY}}{\mu L_{meqY}}(\bar{P}_m - \bar{P}_f) \quad [4.68]$$

$$q_{eqZ} = -\rho\frac{k_{mz}A_{meqZ}}{\mu L_{meqZ}}(\bar{P}_m - \bar{P}_f) \quad [4.69]$$

ρ is fluid density, μ is viscosity, $\bar{P}_m$ is the average matrix pressure, and $\bar{P}_f$ is the average matrix pressure. k_{mx}, k_{my}, and k_{mz} are matrix permeability in each Cartesian direction. A_{meqX}, A_{meqY}, and A_{meqZ} is the summed contact surface area in the Y-Z, X-Z, and X-Y planes respectively between matrix and fractures:

$$A_{meqX} = 2N_{FX}(N_{FY}+1)(N_{FZ}+1)h_{my}h_{mz} = 2N_{FX}\sum h_{my_i}\sum h_{mz_i} \quad [4.70]$$

$$A_{meqY} = 2N_{FY}(N_{FX}+1)(N_{FZ}+1)h_{mx}h_{mz} = 2N_{FY}\sum h_{mx_i}\sum h_{mz_i} \quad [4.71]$$

$$A_{meqZ} = 2N_{FZ}(N_{FX}+1)(N_{FY}+1)h_{mx}h_{my} = 2N_{FZ}\sum h_{mx_i}\sum h_{my_i} \quad [4.72]$$

L_{eqX}, L_{eqY}, and L_{eqZ} are the equivalent matrix block half-lengths in each Cartesian direction:

$$L_{meqX} = \frac{(N_{FX}+1)h_{mx}}{2N_{FX}} = \frac{\sum h_{mx_i}}{2N_{FX}} \quad [4.73]$$

$$L_{meqY} = \frac{(N_{FY}+1)h_{my}}{2N_{FY}} = \frac{\sum h_{my_i}}{2N_{FY}} \quad [4.74]$$

$$L_{meqZ} = \frac{(N_{FZ}+1)h_{mz}}{2N_{FZ}} = \frac{\sum h_{mz_i}}{2N_{FZ}} \quad [4.75]$$

These equations were derived in a finite-difference framework where $\bar{P}_m$ is defined at the center of each block and $\bar{P}_f$ at the center of each fracture. The fractures are thin, so the distance between $\bar{P}_f$ and $\bar{P}_m$ is one-half the matrix thickness in each direction. However, not every matrix block is drained on both faces, which I show for a 1-D case (**Figure 4.25a**). The no-flow boundary effects are removed by transforming the system of matrix blocks into an equivalent matrix block draining on both sides (**Figure 4.25b**). As the number of fractures increases, the equivalent thickness approaches one half of the matrix thickness (**Figure 4.25c**). The total mass-flux rate (q_T) between the fractured domain and the matrix domain is the sum of the mass flux in each Cartesian direction is:

$$q_T = q_{eqX} + q_{eqY} + q_{eqZ} \quad [4.76]$$

The shape factor (α) is dimensionless constant used to simplify this total mass flux [4.76] into an expression dependent only on the matrix geometry and average pressure differential between the matrix and fractures (Warren et al. 1963):

$$q'_T = \frac{q_T}{V_B} = -\rho k_{meq} \frac{\alpha}{\mu} (\bar{P}_m - \bar{P}_f) \quad [4.77]$$

k_{meq} is the characteristic equivalent permeability in the matrix. Shape factor is:

$$\alpha = \frac{\left[\frac{k_{mx}A_{meqX}}{L_{meqx}} + \frac{k_{my}A_{meqY}}{L_{meqY}} + \frac{k_{mz}A_{meqZ}}{L_{meqZ}}\right]}{V_B k_{meq}} \quad [4.78]$$

Combing equations [4.66] through [4.78] gives the value of shape factor:

$$\alpha = \frac{4}{k_{meq}}\left[k_{mx}\left(\frac{N_{FX}}{(N_{FX}+1)h_{mx}}\right)^2 + k_{my}\left(\frac{N_{FY}}{(N_{FY}+1)h_{my}}\right)^2 + k_{mz}\left(\frac{N_{FZ}}{(N_{FZ}+1)h_{mz}}\right)^2\right] \quad [4.79]$$

For the case with isotropic matrix permeability ($k_{meq} = k_m = k_{mx} = k_{my} = k_{mz}$):

$$\alpha = 4\left[\left(\frac{N_{FX}}{(N_{FX}+1)h_{mx}}\right)^2 + \left(\frac{N_{FY}}{(N_{FY}+1)h_{my}}\right)^2 + \left(\frac{N_{FZ}}{(N_{FZ}+1)h_{mz}}\right)^2\right] \quad [4.80]$$

The equivalent formulation for Equation [4.80] in terms of fracture spacing and aperture is:

$$\alpha = 4\left[\left(\frac{N_{FX}}{(N_{FX}+1)(S_{fx}-w_{fx})}\right)^2 + \left(\frac{N_{FY}}{(N_{FY}+1)(S_{fy}-w_{fy})}\right)^2 + \left(\frac{N_{FZ}}{(N_{FZ}+1)(S_{fz}-w_{fz})}\right)^2\right] \quad [4.81]$$

For the case with isotropic matrix permeability ($k_m = k_{mx} = k_{my} = k_{mz}$), cubic matrix ($h_m = h_{mx} = h_{my} = h_{mz}$), and equal fracture density ($N_F = N_{FX} = N_{FY} = N_{FZ}$), shape factor is:

$$\alpha = \frac{12}{h_m^2}\frac{N_F^2}{(N_F+1)^2} \quad [4.82]$$

For the case with isotropic matrix permeability and only horizontal fractures:

$$\alpha = \frac{4}{h_{mz}^2}\frac{N_{FZ}^2}{(N_{FZ}+1)^2} \quad [4.83]$$

I incorporate shape factor in my numerical pulse-decay simulator by discretizing the equations presented earlier for each block in my numerical grid. For the layered dual-permeability model, the same basic approach is used.

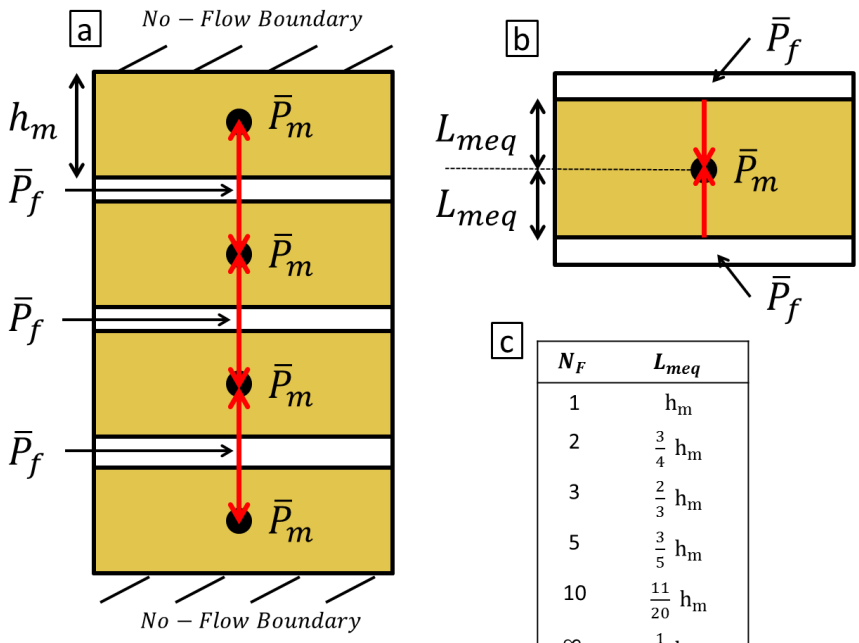

N_F	L_{meq}
1	h_m
2	$\frac{3}{4}$ h_m
3	$\frac{2}{3}$ h_m
5	$\frac{3}{5}$ h_m
10	$\frac{11}{20}$ h_m
∞	$\frac{1}{2}$ h_m

Figure 4.25 a. Schematic for 1-D fractured media. Average matrix pressure is defined at the center of each matrix block where red arrows indicate fluid flow (shown is the case where fracture pressure is higher than matrix pressure). The number of matrix-fracture interfaces is equal to two times the number of fractures. The model has no-flow boundaries at the top and bottom. **b.** Equivalent layer thickness where the boundaries are removed and flow occurs on both faces. **c.** Relationship number of fractures (N_F) and the equivalent matrix half-length (L_{meq}) in terms of matrix block thickness (h_m). As N_F goes to infinity, L_{meq} goes to one-half of h_m. This convergence reflects the decreasing importance of the no-flow boundaries at the model edges.

4D.5: EQUATIONS OF STATE

I used the Peng Robinson (Peng et al. 1976) Equation of State (EOS) to generate gas compressibility "z" factors. Isothermal gas compressibility, C_g, was numerically calculated using:

$$C_g = \frac{1}{P} - \frac{1}{z}\frac{dz}{dP} \quad [4.84]$$

Gas viscosity was calculated using either the Lucas method (Reid et al. 1987) (for non-hydrocarbon rich gases) and the Lee, Gonzalez, and Eakin Correlation (Lee et al. 1966) (for hydrocarbon-rich gases). I verified simulated properties against values provided by the National Institute of Standards and Technology (NIST) fluid properties database ((NIST) 2011).

4D.6: MASS BALANCE CALCULATIONS

The reservoir-core-reservoir system in the pulse-decay experiment is a closed system. Therefore, the fluid mass in the system should not change over the course of simulation, as any changes imply a loss or gain of mass. While small changes may occur as a computing side-effect, they should be as small as possible. The amount of mass change is quantified using the incremental mass balance (IMB) and cumulative mass balance (CMB) calculations. The IMB (Equation [4.85]) is defined as the relative change in fluid mass between the n+1 and the n time levels:

$$\text{IMB} = \frac{\Sigma \frac{V_{b_i}\phi_i}{\alpha_c}\left(\frac{1}{B_g^{n+1}}\right)_i + \Delta t^{n+1} \Sigma\, q_i{}^{n+1}}{\Sigma \frac{V_{b_i}\phi_i}{\alpha_c}\left(\frac{1}{B_g^{n}}\right)_i} \quad [4.85]$$

The CMB (Equation [4.86]) is defined as the relative change in fluid mass between the final time step at time level n, and the initial state at time level, n = 1:

$$\text{CMB}=\frac{\sum_1^n \frac{V_{b_i}\phi_i}{\alpha_c}\left(\frac{1}{B_g^n}\right)_i \Delta t^n + \sum_1^n \sum q_i{}^n \Delta t^n}{\sum \frac{V_{b_i}\phi_i}{\alpha_c}\left(\frac{1}{B_g^1}\right)_i} \quad [4.86]$$

Where:
$\sum_1^n$ = The summation from time step 1
$\sum$ = The summation across all nodes
Δt^n = time step at time level n
$q_i{}^n$ = source/sink term at each block (if present) at time level n [SCF/D]
$\frac{V_{b_i}\phi_i}{\alpha_c}\left(\frac{1}{B_g^n}\right)_i$ = the volume of gas contained within a grid block at time n [SCF]

Ertekin (2001) recommends that the value of IMB be maintained between 0.995 and 1.005 over the course of the simulation, and that the CMB be within similar bounds. I show an example model output that I use to analyze the incremental and cumulative mass (IMB/CMB) ratios over time (**Figure 4.26**). Analysis of the data indicates an absolute change of < 0.02% over the entire simulation run-- well within the recommended bounds.

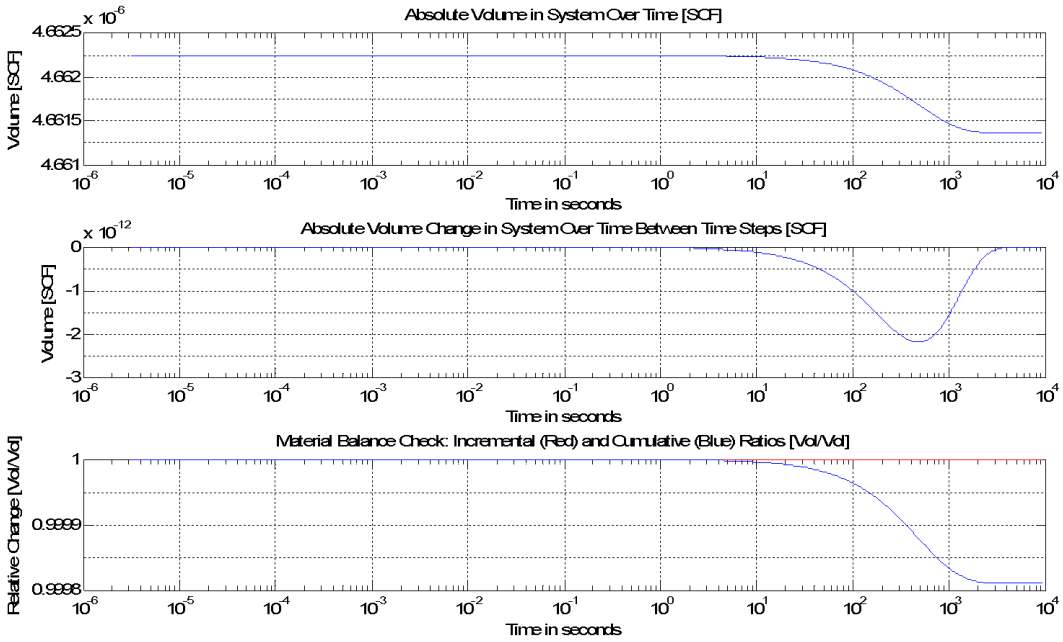

Figure 4.26 Multiplot analysis panel of incremental mass balance (IMB) and cumulative mass balance (CMB) over time in the numerical simulation. The top panel is the volume of gas in the system [SCF] vs. time (sec). The middle panel is the absolute change in total system volume of gas [SCF] vs. time [sec]. The final panel is the calculated IMB and CMB curves in blue and red respectively.

4D.7: HISTORY MATCHING PROTOCOL

I systematically vary model properties in the simulator to replicate ("history match") an experimental pulse-decay response. I schematically illustrate this process in **Figure 4.27**. There are several methods of defining the quality or "goodness" of fit between an experimental data set and the model being fitted to the data. I use the least-squares method which minimizes the sum, S, of the square of the error between the model and the experimental data. This is expressed mathematically as:

$$S = \sum_{i=1}^{m} r_i^2 \quad [4.87]$$

Where:

$$r_i = y(x_i) - f(x_i, \beta) \quad [4.88]$$

r_i is the residual at calculated at the x-location of the ith experimental data point. It is the difference between the data, $y(x_i)$, and the model $f(x_i, \beta)$. x_i is the x-location for the m experimental data points. $f(x_i, \beta)$ is the generic expression for a model function in one-dimension where the fitting parameter, β, is adjusted. $y(x_i)$ is the y-value associated with each experimental data point at x_i and S is the sum of the squared residual.

The objective function in this history match is to identify the value of the fitting parameter, β, that minimizes the sum of the square residuals, *S*. This minimum occurs when the derivative of *S* with respect to β is equal to zero:

$$\frac{\partial S}{\partial \beta} = 2 \sum_{i=1}^{m} r_i \frac{\partial r_i}{\partial \beta} = 0 \quad [4.89]$$

and *S* is concave up with respect to β:

$$\frac{\partial^2 S}{\partial \beta^2} = 2 \sum_{i=1}^{m} \left[\left(\frac{\partial r_i}{\partial \beta} \right)^2 + r_i \frac{\partial^2 r_i}{\partial \beta^2} \right] > 0 \quad [4.90]$$

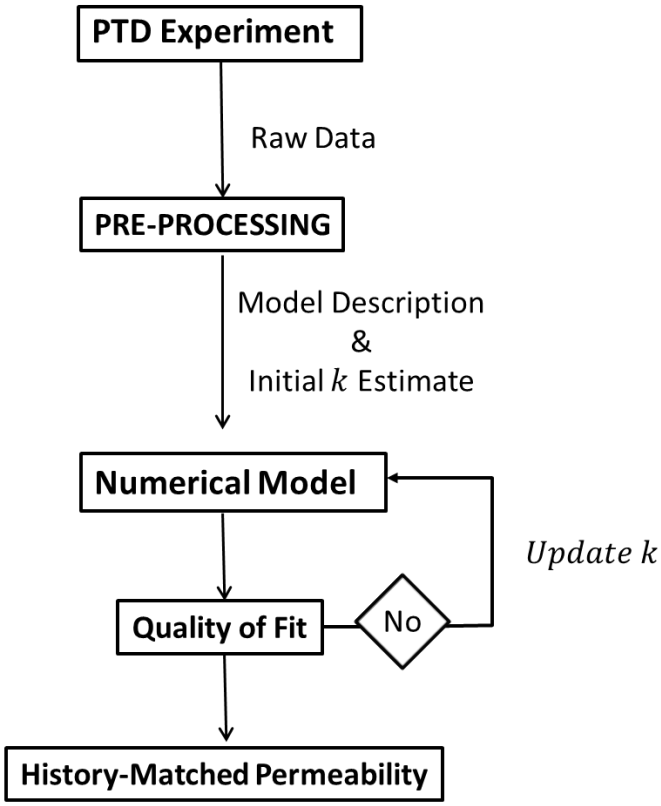

Figure 4.27 Pseudo-code for history-matching experimental pulse-decay permeability data to interpret core sample permeability.

For this single model parameter case, I use permeability, k, as the fitting parameter, β, in the minimization of S. There are various methods of identifying minimums, but I use the line search method. The line search method entails calculating S at a series of permeability values centered about the initial starting estimate for core permeability. Based on the observed gradient, $\frac{\Delta S}{\Delta k}$, the permeability value associated with the minimum value of S will be selected as the best-fitting history-matched permeability value. This method is valid when the global minimum is contained within the line search interval. I illustrate how I used the line-search method to interpret permeability in a ceramic core sample. The plot of S vs. k reveals a global minimum at $k = 9.3x10^{-18}m^2$ (Figure 4.28). Next, I show that simulating the reservoir-pressure time-series data using $k = 9.3x10^{-18}m^2$ provides a high-quality fit to the experimental data with respect to reservoir pressure versus time (Figure 4.29), differential pressure versus time (Figure 4.30), and the natural log of dimensionless differential pressure versus time (Figure 4.31).

Multivariate analysis with multiple unknowns follows a similar approach to the single-variable case. However, it is significantly more complicated because there are now n fitting parameters such that the sum of square residuals for the multivariate case is:

$$S(\beta_n, \beta_{n-1}, \dots, \beta_1) = \sum\big(y(x_i) - f(x_i, \beta_n, \beta_{n-1}, \dots, \beta_1)\big)^2 \quad [4.91]$$

Madsen et al. (1999) describe in detail various algorithms to identify the values of β_i that minimize $S(\beta_n, \beta_{n-1}, \dots, \beta_1)$.

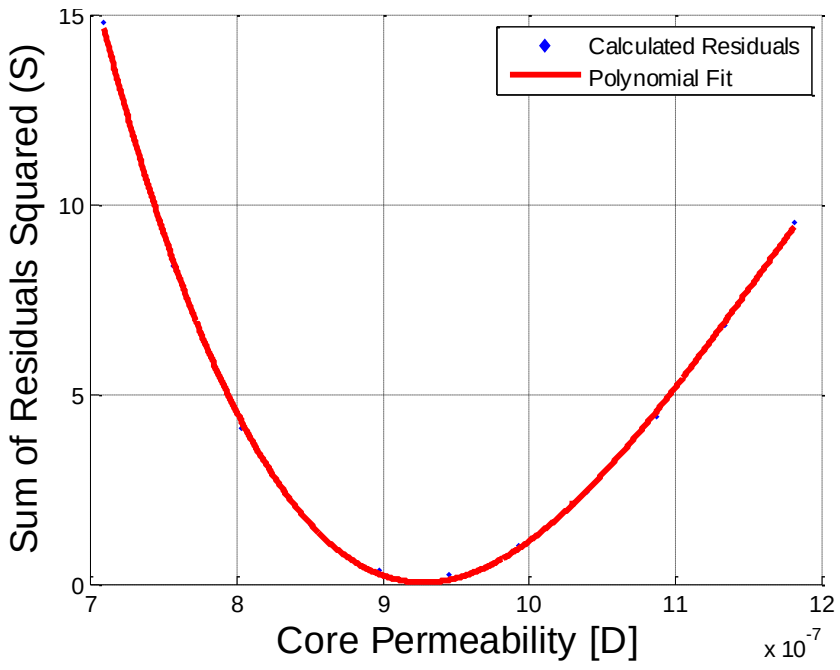

Figure 4.28 Example plot of the sum of residuals squared (S) vs. core permeability (fitting parameter) accompanying the history match of test PTD0082. Blue points are calculated *S* values, while the red line is a polynomial fit to the 11 calculated data points. The minimum *S* value occurs at a permeability value of ~9.24 μD compared to the initial guess (from analytical late-time solution) of ~9.50 μD for core permeability, a difference of approximately 2.5%.

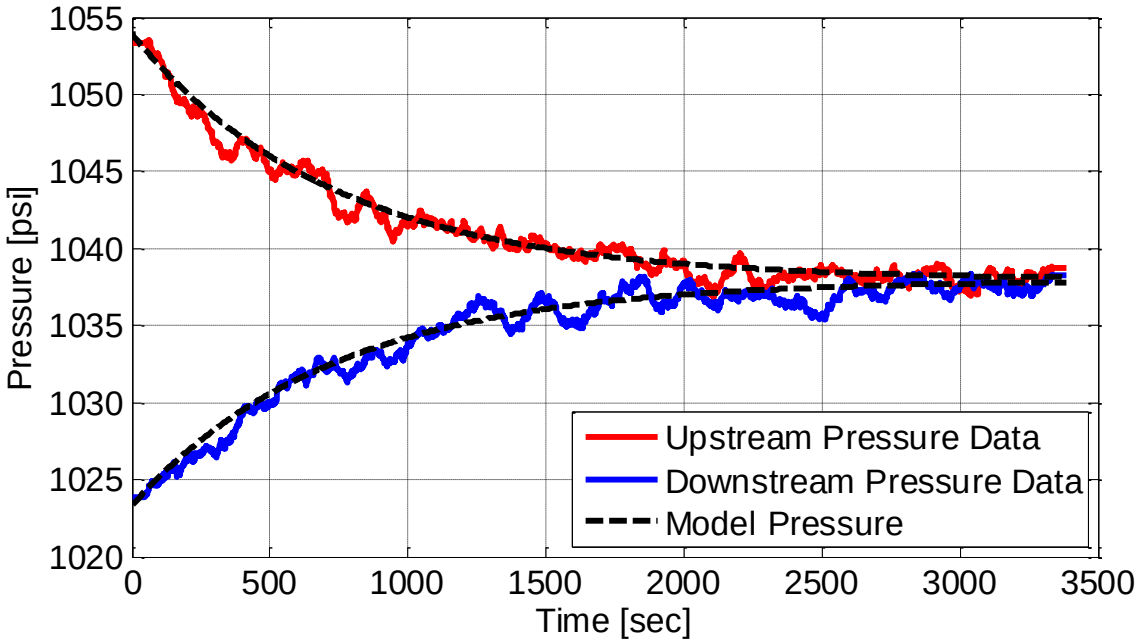

Figure 4.29 Comparison of experimental pulse-decay reservoir pressure time-series data to numerical model results. The calculated permeability is $9.3x10^{-18}m^2$ and the quality of fit between model and experimental observations is good.

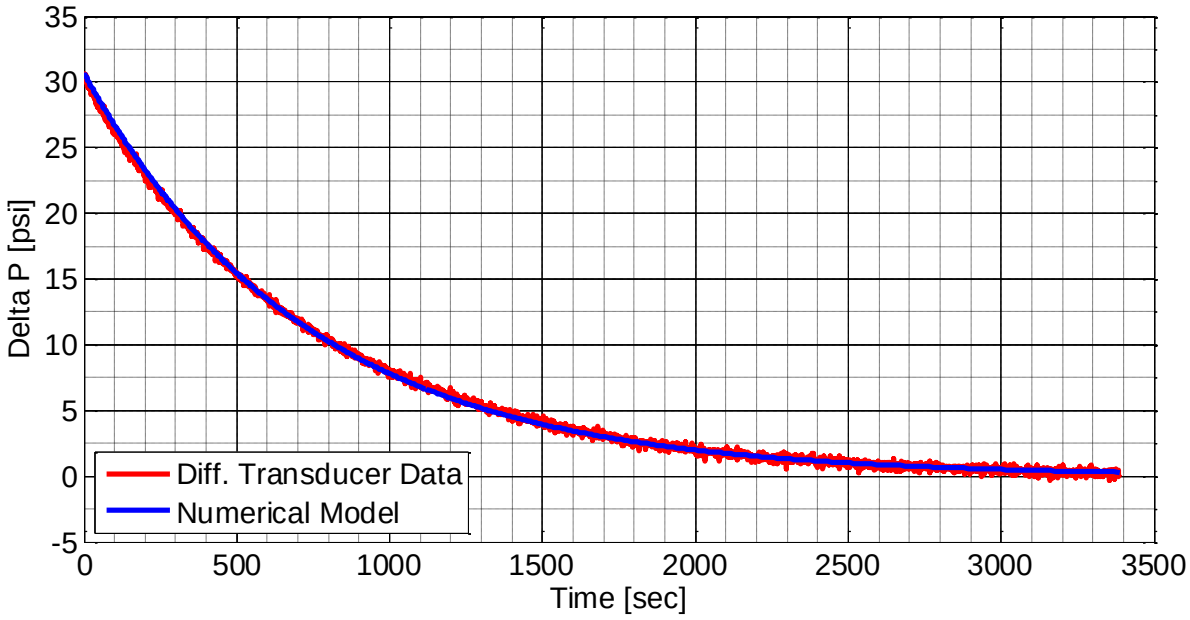

Figure 4.30 Comparison of model (blue) versus experimental (red) values for dimensionless differential pressure versus time. The calculated permeability is 9.28 μD and the quality of fit between model and experimental observations is good.

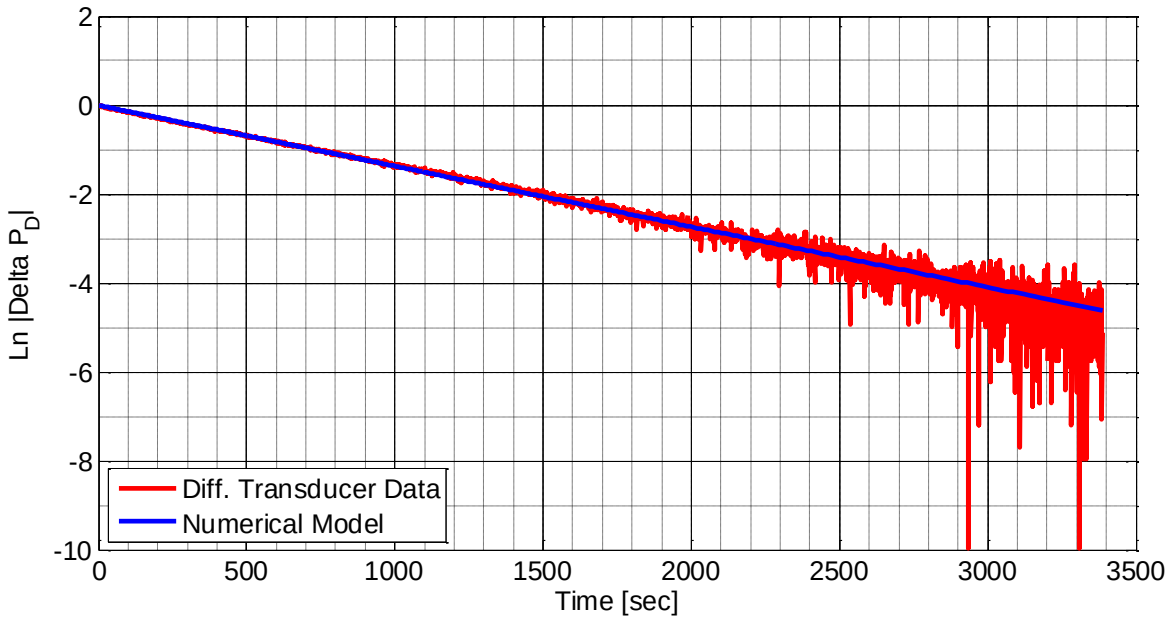

Figure 4.31 Comparison of model (blue) versus experimental (red) values for the natural log of dimensionless differential pressure versus time. The calculated permeability is 9.28 μD and the quality of fit between model and experimental observations is good.

References

(API), A.P.I.: Recommended Practices for Core Analysis (2nd Edition). In: Exploration and Production Department, vol. Recommended Practice 40. API Publishing Services, 1220 L Street, N.W., Washington, D.C. 20005, (1998)

(NIST), N.I.o.S.a.T.: Thermophysical Properties of Fluid Systems. http://webbook.nist.gov/chemistry/fluid/ (2011). 2013

API: 10B-2/ISO 10426-2: 2005. In: Recommended Practice For Testing Well Cement. (2005)

Benson, P.M., Meredith, P.G., Schubn|el, A.: Role of void space geometry in permeability evolution in crustal rocks at elevated pressure. Journal of Geophysical Research **111**, B12203 (2006)

Bhandari, A.R., Flemings, P.B., Polito, P.J., Cronin, M.B., Bryant, S.L.: Anisotropy and Stress Dependence of Permeability in the Barnett Shale. Transport in Porous Media (*in review*)

Bird, R.B., Stewart, W.E., Lightfoot, E.N.: Transport Phenomena, Second ed. John Wiley & Sons, Inc., Hoboken, NJ (2007)

Bourbie, T., Walls, J.: Pulse decay permeability: Analytical solution and experimental test : Bourbie, T; Walls, J Soc Petr Engr J, V22, N5, Oct 1982, P719-721. International Journal of Rock Mechanics and Mining Sciences & Geomechanics Abstracts **20**(2), A37-A37 (1983). doi:10.1016/0148-9062(83)90369-8

Brace, W.F., Walsh, J.B., Frangos, W.T.: Permeability of Granite Under High Pressure. Journal of Geophysical Research **73**(6), 2225-2236 (1968)

Bustin, R.M., Bustin, A.M.M., Cui, A., Ross, D., Pathi, V.M.: Impact of Shale Properties on Pore Structure and Storage Characteristics, 2008/1/1/

Cinco-Ley, H., Samaniego-V, F.: Transient Pressure Analysis for Fractured Wells. Journal of Petroleum Technology (1981). doi:10.2118/7490-pa

Civan, F., Rai, C., Sondergeld, C.: Shale-Gas Permeability and Diffusivity Inferred by Improved Formulation of Relevant Retention and Transport Mechanisms. Transport in Porous Media **86**(3), 925-944 (2011). doi:10.1007/s11242-010-9665-x

Civan, F., Rasmussen, M.L.: Parameters of Matrix/Fracture Immiscible-Fluids Transfer Obtained by Modeling of Core Tests. SPE Journal **17**(2), pp. 540-554 (2012). doi:10.2118/104028-pa

Craig, R.F.: Craig's Soil Mechanics. Spoon Press, New York, NY (2004)

Cronin, M.B.: Using Brazilian Disk Tests to Define Tensile Strength of Lithologies in the Lower Oatka Creek and Upper Cherry Valley Members of the Marcellus Shale. Senior Thesis in Geosciences, Pennyslvania State University (2011)

Cui, X., Bustin, A.M.M., Bustin, R.M.: Measurements of gas permeability and diffusivity of tight reservoir rocks: different approaches and their applications. Geofluids **9**(3), 208-223 (2009). doi:10.1111/j.1468-8123.2009.00244.x

Dandekar, A.Y.: Petroleum reservoir rock and fluid properties. CRC press, (2013)

Desbarats, A.J.: Numerical estimation of effective permeability in sand-shale formations. Water Resour. Res. **23**(2), 273-286 (1987). doi:10.1029/WR023i002p00273

Dicker, A.I., Smits, R.M.: A Practical Approach for Determining Permeability From Laboratory Pressure-Pulse Decay Measurements. Paper presented at the International Meeting on Petroleum Engineering, Tianjin, China, 01/01/1988

EIA: Technically Recoverable Shale Oil and Shale Gas Resources: An Assessment of 137 Shale Formations in 41 Countries Outside the United States. In: Administration, U.S.E.I. (ed.). U.S. Department of Energy (DOE), (2013)

Ertekin, T., Abou-Kassem, J.H., King, G.R.: Basic Applied Reservoir Simulation. SPE Textbook Series vol. Vol. 7. Society of Petroleum Engineers, (2001)

Fathi, E., Akkutlu, I.Y.: Matrix Heterogeneity Effects on Gas Transport and Adsorption in Coalbed and Shale Gas Reservoirs. Transport in Porous Media **80**(2), 281-304 (2009). doi:10.1007/s11242-009-9359-4

Gale, J.F., Reed, R.M., Holder, J.: Natural fractures in the Barnett Shale and their importance for hydraulic fracture treatments. AAPG Bulletin **91**(4), 603-622 (2007)

Geiser, P., Lacazette, A., Vermiyle, J.: Beyond 'dots in a box'; an empirical view of reservoir permeability with tomographic fracture imaging. First Break **30**(7), 63-69 (2012)

Grieser, W.V., Shelley, R.F., Johnson, B.J., Fielder, E.O., Heinze, J.R., Werline, J.R.: Data Analysis of Barnett Shale Completions. SPE Journal (2008). doi:10.2118/100674-pa

Heath, J.E., Dewers, T.A., McPherson, B.J.O.L., Petrusak, R., Chidsey, T.C., Jr., Rinehart, A.J., Mozley, P.S.: Pore networks in continental and marine mudstones: Characteristics and controls on sealing behavior. Geosphere **7**(2), 429-454 (2011). doi:10.1130/ges00619.1

Hickey, J.J., Henk, B.: Lithofacies summary of the Mississippian Barnett Shale, Mitchell 2 T.P. Sims well, Wise County, Texas. AAPG Bulletin **91**(4), 437-443 (2007). doi:10.1306/12040606053

Holder, J., et al.: Laboratory Measurement of Permeability in Rock. In: al., C.e. (ed.) Key Questions in Rock Mechanics. Balkema, Rotterdam (1988)

Hondros, G.: The evaluation of Poisson's ratio and the modulus of materials of a low tensile resistance by the Brazilian (indirect tensile) test with particular reference to concrete. Australian Journal of Applied Science **10**(3), 243-268 (1959)

Hsieh, P.A., Tracy, J.V., Neuzil, C.E., Bredehoeft, J.D., Silliman, S.E.: A transient laboratory method for determining the hydraulic properties of `tight' rocks--I. Theory. International Journal of Rock Mechanics and Mining Sciences &

Geomechanics Abstracts **18**(3), 245-252 (1981). doi:10.1016/0148-9062(81)90979-7

Ingram, R.L.: Fissility of Mudrocks. Geological Society of America Bulletin **64**(8), 869-878 (1953). doi:10.1130/0016-7606(1953)64[869:fom]2.0.co;2

Jannot, Y., Lasseux, D., Vize, G., Hamon, G.: A Detailed Analysis of Permeability and Klinkenberg coefficient estimation from unsteady-state pulse-decay or draw-down experiments. Paper presented at the International Symposium of the Society of Core Analysts, Calgary, Canada, 10-12 September, 2007

Jarvie, D.M., Hill, R.J., Ruble, T.E., Pollastro, R.M.: Unconventional shale-gas systems: The Mississippian Barnett Shale of north-central Texas as one model for thermogenic shale-gas assessment. AAPG Bulletin **91**(4), 475-499 (2007). doi:10.1306/12190606068

Javadpour, F.: Nanopores and Apparent Permeability of Gas Flow in Mudrocks (Shales and Siltstone). Journal of Canadian Petroleum Technology(08) (2009). doi:10.2118/09-08-16-da

Jones, S.C.: A Technique for Faster Pulse-Decay Permeability Measurements in Tight Rocks SPE Formation Evaluation **12**(1), 19-26 (1997). doi:10.2118/28450-PA

Kamath, J., Boyer, R.E., Nakagawa, F.M.: Characterization of Core-Scale Heterogeneities Using Laboratory Pressure Transients. SPE Formation Evaluation **September** (1992)

Kazemi, H., Merrill Jr., L.S., Porterfield, K.L., Zeman, P.R.: Numerical Simulation of Water-Oil Flow in Naturally Fractured Reservoirs. Society of Petroleum Engineers Journal **16**(6), 317-326 (1976). doi:10.2118/5719-pa

King, G.R., Ertekin, T., Schwerer, F.C.: Numerical Simulation of the Transient Behavior of Coal-Seam Degasification Wells. (1986). doi:10.2118/12258-pa

Kutchko, B.G., Strazisar, B.R., Lowry, G.V., Dzombak, D.A., Thaulow, N.: Rate of CO2 attack on hydrated Class H well cement under geologic sequestration conditions. Environmental science & technology **42**(16), 6237-6242 (2008)

Lee, A., Gonzalez, M., Eakin, B.: The Viscosity of Natural Gases. SPE Paper 1340. Journal of Petroleum Technology **18**, 997-1000 (1966)

Lee, J., Rollins, J.B., Spivey, J.P.: Pressure transient testing. Society of Petroleum Engineers, (2003)

Lim, K.T., Aziz, K.: Matrix-fracture transfer shape factors for dual-porosity simulators. Journal of Petroleum Science and Engineering(13), 169-178 (1995)

Lin, C., Pirie, G., Trimmer, D.A.: Low Permeability Rocks: Laboratory Measurements and Three-Dimensional Microstructural Analysis. J. Geophys. Res. **91**(B2), 2173-2181 (1986). doi:10.1029/JB091iB02p02173

Loucks, R.G., Reed, R.M.: Scanning-Electron-Microscope Petrographic Evidence for Distinguishing Organic-Matter Pores Associated with Depositional Organic Matter versus Migrated Organic Matter in Mudrocks. Gulf Coast Association of Geological Studies **3**, 51-60 (2014)

Loucks, R.G., Reed, R.M., Ruppel, S.C., Jarvie, D.M.: Morphology, genesis, and distribution of nanometer-scale pores in siliceous mudstones of the Mississippian Barnett Shale. Journal of Sedimentary Research **79**(12), 848-861 (2009)

Loucks, R.G., Ruppel, S.C.: Mississippian Barnett Shale: Lithofacies and depositional setting of a deep-water shale-gas succession in the Fort Worth Basin, Texas. AAPG Bulletin **91**(4), 579-601 (2007). doi:10.1306/11020606059

Luffel, D.L., Houston, R., Hopkins, C.W., Inc, S.A.H.a.A., Schettler, P.D.J.: Matrix Permeability Measurement of Gas Productive Shales. Paper presented at the 6th Annual Technical Conference and Exhibition of the Society of Petroleum Engineers, Houston, TX,

Macquaker, J.: A lithofacies study of the Peterborough Member, Oxford Clay Formation (Jurassic), UK: an example of sediment bypass in a mudstone succession. Journal of the Geological Society **151**(1), 161-172 (1994)

Macquaker, J.H.S., Adams, A.E.: Maximizing Information from Fine-Grained Sedimentary Rocks: An Inclusive Nomenclature for Mudstones. Journal of Sedimentary Research **73**(5), 735-744 (2003). doi:10.1306/012203730735

Madsen, K., Bruun, H., Tingleff, O.: Methods for non-linear least squares problems. (1999)

Mehmani, A., Prodanović, M., Javadpour, F.: Multiscale, Multiphysics Network Modeling of Shale Matrix Gas Flows. Transport in Porous Media **99**(2), 377-390 (2013). doi:10.1007/s11242-013-0191-5

Milliken, K., Choh, S.-J., Papazis, P., Schieber, J.: “Cherty” stringers in the Barnett Shale are agglutinated foraminifera. Sedimentary Geology **198**(3–4), 221-232 (2007). doi:http://dx.doi.org/10.1016/j.sedgeo.2006.12.012

Milliken, K.L.: SEM-Based Cathodoluminescence Imaging for Discriminating Quartz Types in Mudrocks. (2013)

Milliken, K.L., Esch, W.L., Reed, R.M., Zhang, T.: Grain assemblages and strong diagenetic overprinting in siliceous mudrocks, Barnett Shale (Mississippian), Fort Worth Basin, Texas. AAPG Bulletin **96**(8), 1553-1578 (2012). doi:10.1306/12011111129

Nickalls, R.: Viète, Descartes and the cubic equation. The Mathematical Gazette **90**(518) (2006)

Nie, R.-S., Meng, Y.-F., Jia, Y.-L., Zhang, F.-X., Yang, X.-T., Niu, X.-N.: Dual Porosity and Dual Permeability Modeling of Horizontal Well in Naturally Fractured Reservoir. Transport in Porous Media **92**(1), 213-235 (2012). doi:10.1007/s11242-011-9898-3

Ning, X.: The measurement of matrix and fracture properties in naturally fractured low permeability cores using a pressure pulse method. Texas A&M University (1992)

Passey, Q.R., Bohacs, K., Esch, W.L., Klimentidis, R., Sinha, S.: From Oil-Prone Source Rock to Gas-Producing Shale Reservoir â□“ Geologic and Petrophysical Characterization of Unconventional Shale-Gas Reservoirs. Paper presented at the

International Oil and Gas Conference and Exhibition in China, Beijing, China, 01/01/2010
Patzek, T.W., Male, F., Marder, M.: Gas production in the Barnett Shale obeys a simple scaling theory. Proceedings of the National Academy of Sciences (2013). doi:10.1073/pnas.1313380110
Peng, D.Y., Robinson, D.B.: A New Two-Constant Equation of State Industrial and Engineering Chemistry: Fundamentals **15**, 59–64 (1976)
Pollastro, R.M., Jarvie, D.M., Hill, R.J., Adams, C.W.: Geologic framework of the Mississippian Barnett Shale, Barnett-Paleozoic total petroleum system, Bend archFort Worth Basin, Texas. AAPG Bulletin **91**(4), 405-436 (2007)
Reid, R.C., Prausnitz, J.M., Poling, B.E.: The Properties of Gases & Liquids, 4th ed. McGraw-Hill Book Company, New York (1987)
Roduit, N.: MicroVision: Image analysis toolbox for measuring and quantifying components of high-definition images. In. (2008)
Rowe, H., Hughes, N., Robinson, K.: The quantification and application of handheld energy-dispersive x-ray fluorescence (ED-XRF) in mudrock chemostratigraphy and geochemistry. Chemical Geology **324–325**(0), 122-131 (2012). doi:http://dx.doi.org/10.1016/j.chemgeo.2011.12.023
Rwechungura, R.W., Dadashpour, M., Kleppe, J.: Advanced History Matching Techniques Reviewed, 2011/1/1/
Schneider, J., Flemings, P.B., Day-Stirrat, R.J., Germaine, J.T.: Insights into pore-scale controls on mudstone permeability through resedimentation experiments. Geology (2011). doi:10.1130/g32475.1
Shephard, F.P.: Nomenclature based on sand-silt-clay ratios. Journal of Sedimentary Petrology **24**(3), 151-158 (1954)
Soeder, D.J.: Porosity and Permeability of Eastern Devonian Gas Shale. SPE Formation Evaluation(03) (1988). doi:10.2118/15213-pa
Sondergeld, C.H., Ambrose, R.J., Rai, C.S., Moncrieff, J.: Micro-Structural Studies of Gas Shales, 2010/1/1/
Suri, P., Azeemuddin, M., Zaman, M., Kukreti, A.R., Roegiers, J.C.: Stress-dependent permeability measurement using the oscillating pulse technique. Journal of Petroleum Science and Engineering **17**(3-4), 247-264 (1997). doi:10.1016/s0920-4105(96)00073-3
Taylor, H.F.: Cement chemistry. Thomas Telford, (1997)
Terry, R.D., Chilingar, G.V.: Summary of "Concerning some additional aids in studying sedimentary formations," by M. S. Shvetsov. Journal of Sedimentary Research **25**(3), 229-234 (1955)
Terzaghi, K.: Theoretical Soil Mechanics. John Wiley & Sons, New York (1943)
Vega, B., Dutta, A., Kovscek, A.: CT Imaging of Low-Permeability, Dual-Porosity Systems Using High X-ray Contrast Gas. Transport in Porous Media **101**(1), 81-97 (2014). doi:10.1007/s11242-013-0232-0
Vermylen, J.: Geomechanical Studies of the Barnett Shale, Texas, USA. Stanford (2011)

Wang, F.P., Reed, R.M.: Pore Networks and Fluid Flow in Gas Shales. Paper presented at the SPE Annual Technical Conference and Exhibition, New Orleans, Louisiana, 01/01/2009

Warren, J.E., Root, P.J.: The Behavior of Naturally Fractured Reservoirs. Society of Petroleum Engineers Journal(September), 245-255 (1963)

Waters, G.A., Dean, B.K., Downie, R.C., Kerrihard, K.J., Austbo, L., McPherson, B.: Simultaneous Hydraulic Fracturing of Adjacent Horizontal Wells in the Woodford Shale, 2009/1/1/

Wilkins, A.D.: Terminology and the classification of fine grained sedimentary rocks - is there a difference between a claystone, a mudstone and a shale? http://www.abdn.ac.uk/tacs/home/documents/Terminology.pdf (2011). 2014

Vita

Michael Brett Cronin graduated from the Pennsylvania State University in 2011 where he obtained a Bachelors of Science (w/ honors) in Geosciences and a Bachelors of Science in Petroleum & Natural Gas Engineering. Michael received the Eric A. Walker award and was the College of Earth & Mineral Sciences Engineering Honor Graduate. Michael interned at the United States Geological Survey (Menlo Park, CA) in 2009 as part of USGS-NAGT program. Michael is privately employed in the oil and gas industry.

Permanent email address: mcronin@utexas.edu

This thesis was typed by Michael Brett Cronin